

# Study of the $B_s$ -Meson with the First LHC Data

Dissertation

zur

Erlangung der naturwissenschaftlichen Doktorwürde  
(Dr. sc. nat.)

vorgelegt der

Mathematisch-naturwissenschaftlichen Fakultät

der

Universität Zürich

von

**Lotte Wilke**

aus Deutschland

## **Promotionskomitee**

Prof. Dr. Claude Amsler (Vorsitz)

Prof. Dr. Vincenzo Chiochia

Dr. Alexander Schmidt

**Zürich, 2009**



# Contents

<b>Abstract</b>	<b>1</b>
<b>Zusammenfassung</b>	<b>3</b>
<b>1 Introduction and Motivation</b>	<b>5</b>
1.1 Quark mixing and CP violation . . . . .	5
1.1.1 The CKM matrix . . . . .	5
1.1.2 CP violation in the quark sector . . . . .	7
1.2 The $B_s$ system . . . . .	9
1.2.1 $B_s$ oscillations . . . . .	9
1.2.2 Classification of CP violating effects . . . . .	10
1.2.3 Helicity amplitudes . . . . .	11
1.2.4 Predictions from the Standard Model . . . . .	15
1.3 $b$ -hadron production at the LHC . . . . .	15
1.4 Results on the $B_s$ system from Tevatron . . . . .	18
1.5 Summary . . . . .	19
<b>2 LHC and the CMS experiment</b>	<b>21</b>
2.1 The Large Hadron Collider . . . . .	21
2.2 The CMS detector . . . . .	24
2.2.1 The solenoid . . . . .	27
2.2.2 Inner tracking system . . . . .	29
2.2.2.1 Silicon pixel detector . . . . .	30
2.2.2.2 Silicon strip detector . . . . .	34
2.2.3 The CMS muon system . . . . .	36
2.2.4 Trigger and data acquisition . . . . .	39
<b>3 Measurement of the Lorentz angle</b>	<b>41</b>
3.1 Introduction . . . . .	41
3.2 Measurement of the Lorentz angle from cosmic ray data . . . . .	44
3.3 Measurement of the Lorentz angle from collision data . . . . .	52
3.3.1 Study of systematic errors . . . . .	54
3.3.1.1 Different simulation values of the Lorentz angle . . . . .	56

3.3.1.2	Impact of wrong Lorentz angle on hit resolution . . .	57
3.3.1.3	Tracker misalignment studies . . . . .	58
3.4	Conclusions . . . . .	59
<b>4</b>	<b>Study of the decay <math>B_s \rightarrow J/\psi (\rightarrow \mu^+ \mu^-) \phi (\rightarrow K^+ K^-)</math></b>	<b>63</b>
4.1	Signal and background samples . . . . .	64
4.1.1	Simulation of the $B_s \rightarrow J/\psi \phi$ signal . . . . .	64
4.1.2	Simulation of the $B_d \rightarrow J/\psi K^*$ background . . . . .	65
4.1.3	Simulation of the $b \rightarrow J/\psi X$ background . . . . .	66
4.1.4	Direct $J/\psi$ production at LHC . . . . .	67
4.2	Trigger reconstruction and selection . . . . .	68
4.2.1	Level-1 Trigger . . . . .	68
4.2.2	Level-2 selection using displaced $J/\psi$ candidates . . . . .	70
4.2.2.1	Primary vertex reconstruction . . . . .	70
4.2.2.2	Muon track reconstruction . . . . .	73
4.2.2.3	$J/\psi$ reconstruction and selection . . . . .	74
4.2.2.4	Prompt $J/\psi$ background rejection . . . . .	75
4.2.2.5	Trigger rates at Level-2 . . . . .	77
4.2.3	Level-3 selection with full $B_s \rightarrow J/\psi \phi$ reconstruction . . . . .	78
4.3	Offline selection and reconstruction . . . . .	80
4.3.1	Pre-selection of $B_s \rightarrow J/\psi (\rightarrow \mu^+ \mu^-) \phi (\rightarrow K^+ K^-)$ decays . . . . .	81
4.3.2	Kinematic vertex fit . . . . .	82
4.3.3	Final $B_s \rightarrow J/\psi (\rightarrow \mu^+ \mu^-) \phi (\rightarrow K^+ K^-)$ selection . . . . .	83
4.3.4	Proper decay time resolution . . . . .	83
4.4	The maximum likelihood fit . . . . .	85
4.4.1	Validation of likelihood fit . . . . .	87
4.4.1.1	Test with different values for the input parameters . . . . .	88
4.4.1.2	Influence of the resolution of the angular variables and the proper decay length . . . . .	89
4.4.2	Signal efficiency from full detector simulation . . . . .	91
4.4.2.1	Angular efficiency . . . . .	91
4.4.2.2	Efficiency of the proper decay time . . . . .	93
4.4.3	Background . . . . .	94
4.4.3.1	Possible improvements in the background description . . . . .	95
4.4.4	The full probability density function . . . . .	97
4.4.5	Results from full detector simulation . . . . .	98
4.4.6	Systematics and detector effects . . . . .	99
4.5	Conclusions . . . . .	104
	<b>Bibliography</b>	<b>107</b>



# Abstract

After more than twenty years of development, collisions at the Large Hadron Collider at CERN are expected to take place at the end of 2009. The aim of the CMS detector is to measure the particles emerging from these interactions. The innermost detector of this high energy experiment is a silicon pixel detector starting only 4 cm apart from the interaction point. Its main goal is to measure tracks and vertices with high precision.

Charged particles passing the silicon pixel detector produce charge carriers which drift in a high electric field ( $V_{\text{bias}} \approx 100 - 600 \text{ V}$ ). Due to the magnetic field of 3.8 T present in the inner part of the CMS detector, charge carriers experience an angular deflection due to the Lorentz force. This leads to a shift in the measured hit coordinate (Lorentz drift). The first part of this thesis presents a measurement of the Lorentz drift based on cosmic data taken in autumn 2008. The drift is approximately  $66 \mu\text{m}$  for the barrel detector and  $20 \mu\text{m}$  for the forward detectors. Furthermore, a method to measure the Lorentz drift from collision data is developed. This is necessary because tracks from collision data cover a different range of incident angles on the detector surface than cosmic rays: In general, in the plane transverse to the beam axis cosmic rays traverse the silicon sensors at larger angles than particles originating from the collision point. This method will allow to monitor the Lorentz drift as the bias voltage is increased to compensate for irradiation damages.

In the second part of this thesis, a physics analysis to measure various properties of the  $B_s$ -meson system is developed. The pixel detector allows a precise measurement of the  $B_s$  decay vertices which are displaced from the proton-proton interaction point. Thus it is the key detector component for this analysis. A decay time dependent angular analysis is performed on selected  $B_s \rightarrow J/\psi(\rightarrow \mu^+\mu^-)\phi(\rightarrow K^+K^-)$  events. With an integrated luminosity of  $1.3 \text{ fb}^{-1}$ , the width difference  $\Delta\Gamma_s$  between the CP eigenstates  $B_s^L$  and  $B_s^H$  could be extracted with an uncertainty of  $0.028 \text{ ps}^{-1}$ , yielding a better measurement than the one currently available from Tevatron (CDF measures  $\Delta\Gamma_s = 0.02 \pm 0.05(\text{stat.}) \pm 0.01(\text{sys.}) \text{ ps}^{-1}$  [1] and D0  $\Delta\Gamma_s = 0.085_{-0.078}^{+0.072}(\text{stat.}) \pm 0.06(\text{sys.}) \text{ ps}^{-1}$  [2]). On the other hand, the CP violating phase in this decay is expected to be very small in the Standard Model ( $\phi_s \approx -0.03$ ). However, the angu-

lar analysis proposed here would be sensitive to non Standard Model contributions, which are expected to be rather large.

# Zusammenfassung

Nach über 20 Jahren Entwicklungsarbeit werden Ende 2009 die ersten Proton-Proton-Kollisionen am LHC in Genf erwartet. Der CMS Detektor wird die bei diesen Kollisionen erzeugten Elementarteilchen registrieren. Die innerste Komponente dieses Grossexperimentes wird von einem Silizium-Pixeldetektor gebildet, dessen Messbereich nur 4 cm vom Wechselwirkungspunkt entfernt beginnt. Hauptaufgabe dieses Pixeldetektors ist die präzise Vermessung von Teilchenspuren und deren Zerfallsvertices.

Beim Durchgang geladener Teilchen durch den Silizium-Pixeldetektor werden freie Ladungsträger erzeugt, welche sich in einem starken äusseren elektrischen Feld bewegen ( $V_{\text{bias}} \approx 100 - 600 \text{ V}$ ). Da im Zentrum des CMS-Detektors ein magnetisches Feld von 3.8 T herrscht, unterliegen die Ladungsträger einer zusätzlichen Ablenkung infolge der Lorentzkraft. Dies führt zu einer Verschiebung in der gemessenen Hitkoodinate (Lorentz-Verschiebung). Im ersten Teil dieser Arbeit wird eine Messung der Lorentz-Verschiebung vorgestellt, die auf einer Messung kosmischer Teilchen im Herbst 2008 beruht. Die Verschiebung beträgt durchschnittlich  $66 \mu\text{m}$  für den Barrel-Pixeldetektor und  $20 \mu\text{m}$  für den Vorwärts-Pixeldetektor. Weiterhin wird eine Methode entwickelt, die die Bestimmung der Lorentz-Verschiebung aus Kollisionsdaten gestattet. Die Entwicklung einer solchen Methode war notwendig, da Spuren, welche von Wechselwirkungspunkt kommen einen anderen Bereich im Einfallswinkel abdecken als kosmische Spuren. In der Ebene senkrecht zur Strahlröhre passieren kosmische Teilchen den Pixeldetektor im allgemeinen mit einem grösseren Winkel als Teilchen, welche vom Wechselwirkungspunkt kommen. Mit Hilfe der vorgestellten Methode lässt sich die Änderung der Lorentz-Verschiebung messen, die über die Laufzeit des Experiments infolge zunehmender Strahlenschäden und einer dadurch notwendigen Erhöhung der Bias-Spannung im Pixeldetektor erwartet wird.

Im zweiten Teil dieser Arbeit wird eine Methode zur Messung verschiedener Eigenschaften des  $B_s$ -Meson-Systems entwickelt. Der Pixeldetektor ist die für diese Analyse wichtigste Detektorkomponente, da er die präzise Messung der Entfernung der  $B_s$  Zerfallsvertices vom Proton-Proton-Wechselwirkungspunkt erlaubt. Eine Zerfallszeit-abhängige Winkelanalyse wird auf  $B_s \rightarrow J/\psi(\rightarrow \mu^+\mu^-)\phi(\rightarrow K^+K^-)$  Ereignisse angewendet, die geeignete Selektionskriterien erfüllen. Die Analyse einer integrierten Luminosität von  $1.3 \text{ fb}^{-1}$  gestattet die Bestimmung der Zerfallsbreiten-Differenz  $\Delta\Gamma_s$ .

zwischen den CP-Eigenzuständen  $B_s^L$  und  $B_s^H$  mit einer Unsicherheit von  $0.028 \text{ ps}^{-1}$ , was eine Verbesserung der bisher verfügbaren Messungen vom Tevatron darstellt (Messungen bei CDF ergaben  $\Delta\Gamma_s = 0.02 \pm 0.05(\text{stat.}) \pm 0.01(\text{sys.}) \text{ ps}^{-1}$  [1] und bei D0  $\Delta\Gamma_s = 0.085^{+0.072}_{-0.078}(\text{stat.}) \pm 0.06(\text{sys.}) \text{ ps}^{-1}$  [2]). Das Standardmodell sagt für die CP-verletzende Phase bei diesem Zerfall einen sehr kleinen Wert voraus ( $\phi_s \approx -0.03$ ). Die hier vorgeschlagene Winkelanalyse ist sensitiv gegenüber Beiträgen von Prozessen jenseits des Standardmodells, welche einen vergleichsweise grossen Wert ergeben.

# Chapter 1

## Introduction and Motivation

The study of  $b$ -hadrons is a magnificent tool to probe the Standard Model of Particle Physics and to look for effects beyond. The  $b$ -quark is the heaviest flavour of the six quarks that can hadronise into mesons and baryons. The even heavier top quark is too short-lived to build any bound state with other quarks.

Section 1.1 introduces quark mixing and  $CP$  violation. A detailed description of the  $B_s$  oscillations and the  $B_s \rightarrow J/\psi \phi$  decay is given in Section 1.2. Section 1.3 explains  $b$ -hadron production at the Large Hadron Collider (LHC) and Section 1.4 presents the latest results on  $B_s$  mixing from the two Tevatron experiments D0 and CDF.

### 1.1 Quark mixing and CP violation

#### 1.1.1 The CKM matrix

The three left-handed quark doublets  $\begin{pmatrix} u \\ d \end{pmatrix}_L$ ,  $\begin{pmatrix} c \\ s \end{pmatrix}_L$  and  $\begin{pmatrix} t \\ b \end{pmatrix}_L$  can mix through the weak interaction. The weak eigenstates  $d'$ ,  $s'$  and  $b'$  are linear combinations of the flavour eigenstates  $d$ ,  $s$ ,  $b$ . The weak eigenstates are related to flavour eigenstates through the *Cabibbo-Kobayashi-Maskawa* (CKM) quark mixing matrix:

$$\begin{pmatrix} d' \\ s' \\ b' \end{pmatrix} = \begin{pmatrix} V_{ud} & V_{us} & V_{ub} \\ V_{cd} & V_{cs} & V_{cb} \\ V_{td} & V_{ts} & V_{tb} \end{pmatrix} \cdot \begin{pmatrix} d \\ s \\ b \end{pmatrix}. \quad (1.1)$$

The matrix is unitary which guarantees the absence of flavour-changing neutral currents. It can be parametrised by three mixing angles and a phase as proposed by the Particle Data Group [3]:

$$\mathbf{V}_{\text{CKM}} = \begin{pmatrix} c_{12}c_{13} & s_{12}c_{13} & s_{13}e^{-i\delta} \\ -s_{12}c_{23} - c_{12}s_{23}s_{13}e^{i\delta} & c_{12}c_{23} - s_{12}s_{23}s_{13}e^{i\delta} & s_{23}c_{13} \\ s_{12}s_{23} - c_{12}c_{23}s_{13}e^{i\delta} & -c_{12}s_{23} - s_{12}c_{23}s_{13}e^{i\delta} & c_{23}c_{13} \end{pmatrix}, \quad (1.2)$$

where  $c_{ij} = \cos \theta_{ij}$  and  $s_{ij} = \sin \theta_{ij}$ . This matrix can also be represented as a product of three rotation matrices, where the central one is extended by a phase factor:

$$\mathbf{V}_{\text{CKM}} = \begin{pmatrix} 1 & 0 & 0 \\ 0 & c_{23} & s_{23} \\ 0 & -s_{23} & c_{23} \end{pmatrix} \cdot \begin{pmatrix} c_{12} & 0 & s_{13}e^{-i\delta} \\ 0 & 1 & 0 \\ -s_{13}e^{i\delta} & 0 & c_{13} \end{pmatrix} \cdot \begin{pmatrix} c_{12} & s_{12} & 0 \\ -s_{12} & c_{12} & 0 \\ 0 & 0 & 1 \end{pmatrix} \quad (1.3)$$

Based on the fact that  $s_{13} \ll s_{23} \ll s_{12} \ll 1$ , the popular *Wolfenstein* parametrisation was developed, nicely displaying the hierarchical pattern of the matrix in powers of  $\lambda = s_{12}$

$$\mathbf{V}_{\text{CKM}} = \begin{pmatrix} 1 - \lambda^2/2 & \lambda & A\lambda^3(\rho - i\eta) \\ -\lambda & 1 - \lambda^2/2 & A\lambda^2 \\ A\lambda^3(1 - \rho - i\eta) & -A\lambda^2 & 1 \end{pmatrix} + \mathcal{O}(\lambda^4), \quad (1.4)$$

with  $A = s_{23}/s_{12}$ ,  $\rho = s_{13}s_{12}/s_{23} \cos \delta$  and  $\eta = s_{13}s_{12}/s_{23} \sin \delta$ . This shows clearly that the transitions  $b \rightarrow c$  and  $b \rightarrow u$  are suppressed by a factor of  $\lambda^2$  and  $\lambda^3$ , respectively.

The unitarity of the CKM matrix implies

$$\sum_i V_{ij} V_{ik}^* = \delta_{jk}, \quad (1.5)$$

$$\sum_j V_{ij} V_{kj}^* = \delta_{ik}, \quad (1.6)$$

where the six vanishing combinations represent triangles in a complex plane. Triangles of neighbouring rows or columns are almost degenerate, meaning that two angles are almost  $90^\circ$  whereas the third angle is almost  $0^\circ$ . Thus, the most commonly used unitarity relation is given by

$$V_{ud} V_{ub}^* + V_{cd} V_{cb}^* + V_{td} V_{tb}^* = 0. \quad (1.7)$$

This equation is then divided by the best known value  $V_{cd} V_{cb}^*$  yielding a triangle (Fig. 1.1) with vertices exactly at  $(0, 0)$ ,  $(0, 1)$  and  $(\bar{\rho}, \bar{\eta})$ , where  $\bar{\rho} = \rho(1 - \lambda^2 + \dots)$  and  $\bar{\eta} = \eta(1 - \lambda^2 + \dots)$ .

One of the degenerate triangles is of importance for this analysis since it contains the  $s$ -quark mixing:

$$V_{us} V_{ub}^* + V_{cs} V_{cb}^* + V_{ts} V_{tb}^* = 0. \quad (1.8)$$

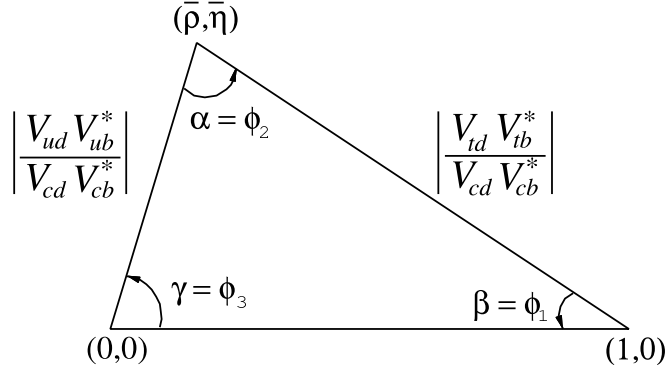


Figure 1.1: Sketch of the unitarity triangle.

dividing this equation by  $V_{cs}V_{cb}^*$  yields a triangle with vertices at  $(0,0)$ ,  $(0,1)$  and  $(\bar{\rho}_s, \bar{\eta}_s)$ .

The different mixing parameters have been measured in a huge variety of experiments [3]. Direct measurements result in  $\alpha + \beta + \gamma = (180_{-30}^{+27})^\circ$ , which is consistent with the Standard Model prediction. The best result for the CKM matrix elements can be obtained by combining all available measurements with the Standard Model constraints (i.e., three generation unitarity) in one global fit. This must also take into account theoretical predictions for hadronic matrix elements which can have significant uncertainties. The two best known fits are CKMfitter which uses frequentist statistics [4], and UTfit using a Bayesian approach [5]. Both provide similar results. The result from CKMfitter is:

$$\begin{aligned} \lambda &= 0.22521 \pm 0.00082, & A &= 0.8116_{-0.0241}^{+0.0097}, \\ \bar{\rho} &= 0.139_{-0.027}^{+0.025}, & \bar{\eta} &= 0.341_{-0.015}^{+0.016}, \end{aligned} \quad (1.9)$$

or written in terms of absolute values of the CKM matrix elements:

$$\mathbf{V}_{\text{CKM}} = \begin{pmatrix} 0.97430 \pm 0.00019 & 0.22521 \pm 0.00082 & 0.00350_{-0.00014}^{+0.00015} \\ 0.22508 \pm 0.00082 & 0.97347 \pm 0.00019 & 0.04117_{-0.00115}^{+0.00038} \\ 0.00859_{-0.00029}^{+0.00027} & 0.04041_{-0.00115}^{+0.00038} & 0.999146_{-0.000016}^{+0.000047} \end{pmatrix} \quad (1.10)$$

The resulting CKM triangles are shown in Fig. 1.2. One can clearly see the degeneracy of the  $s$ -quark triangle.

### 1.1.2 CP violation in the quark sector

Under charge conjugation (expressed by the  $C$  operator) all quantum numbers of a particle are exchanged, e.g.  $Q \rightarrow -Q$  for the electric charge. The parity operator ( $P$ ) reverses the handedness of space, so  $\vec{x} \rightarrow -\vec{x}$ . Gravitational, electromagnetic and strong interactions are  $C$  and  $P$  symmetric. The weak interaction involving  $W^\pm$  bosons however, affects only left-handed particles or right-handed antiparticles which

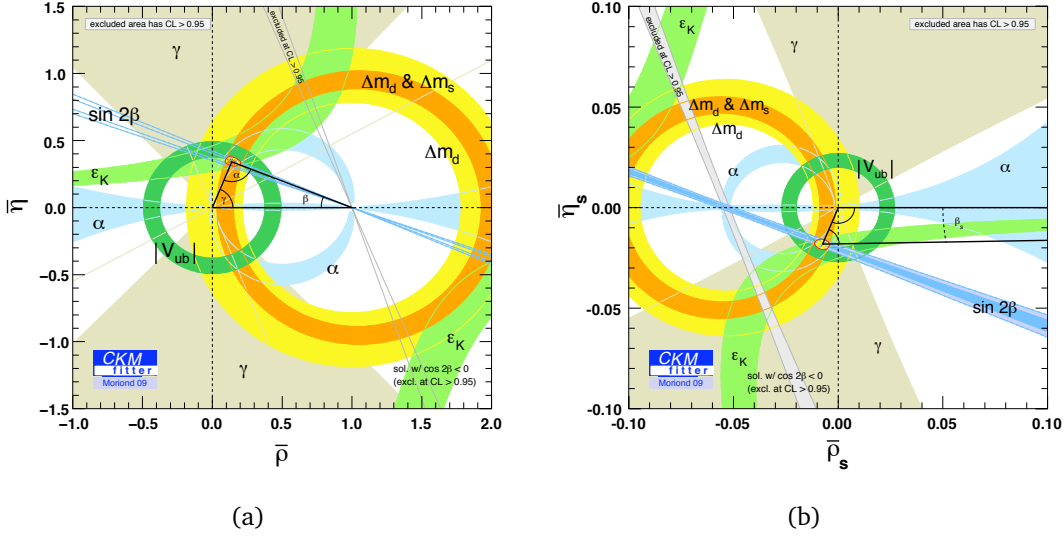


**Figure 1.2:** Constraints on the CKM parameters in the  $\bar{\rho}, \bar{\eta}$  (a) and  $\bar{\rho}_s, \bar{\eta}_s$  (b) plane. Shaded areas have 95% CL [4].

means that the interaction is neither invariant under charge conjugation nor under parity conjugation thus maximally violating both  $C$  and  $P$ .

Applying  $C$  and  $P$  transformations at the same time means changing a left- (right)-handed particle into a right- (left)-handed antiparticle, e.g.

$$e_L^- \xrightarrow{CP} e_R^+. \quad (1.11)$$

Naively one would assume that the combined transformation  $CP$  is not violated by any force. However, in 1964 it was discovered that  $CP$  is violated in the weak interaction. The only possible way this can be described in the Standard Model is through the complex phase  $\delta$  in the  $CKM$ -matrix. Since this phase always appears multiplied by the small number  $s_{13}$  ( $= V_{ub} \approx 10^{-3}$ )  $CP$  violation is suppressed. However, many models beyond the Standard Model expect additional sources of  $CP$  violation, which is for example necessary to explain the matter-antimatter asymmetry in the universe.

The next section gives an explanation of how  $CP$  violation can be measured in the meson sector, and in particular in  $B_s \rightarrow J/\psi(\rightarrow \mu^+\mu^-)\phi(\rightarrow K^+K^-)$  decays.



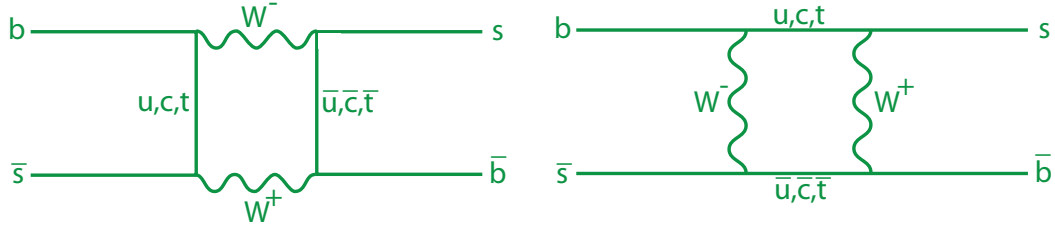


Figure 1.3: Dominant box diagrams for  $B_s \leftrightarrow \bar{B}_s$  oscillations.

## 1.2 The $B_s$ system

### 1.2.1 $B_s$ oscillations

Two different particles  $A$  and  $B$  can convert into each other provided that no conservation law is violated:

$$A \rightarrow B \rightarrow A \rightarrow \dots \quad (1.12)$$

This is the case for flavoured neutral mesons pairs ( $A, B = \bar{A}$ ) such as  $K^0 = d\bar{s}$ ,  $D^0 = c\bar{u}$ ,  $B_d = d\bar{b}$  and  $B_s = s\bar{b}$ . These oscillations are described by box diagrams as shown in Fig. 1.3 for the  $B_s$  system.

An initial state being a composition of the flavour eigenstates  $B_s$  and  $\bar{B}_s$ :

$$|\psi(0)\rangle = a(0) \cdot |B_s\rangle + b(0) \cdot |\bar{B}_s\rangle \quad (1.13)$$

will evolve in time by oscillating or decaying into all possible final states  $f_1, f_2, \dots$

$$|\psi(t)\rangle = a(t) \cdot |B_s\rangle + b(t) \cdot |\bar{B}_s\rangle + c_1(t) |f_1\rangle + c_2(t) |f_2\rangle + \dots \quad (1.14)$$

In case one is only interested in the time evolution of  $B_s$  and  $\bar{B}_s$ , time evolution can be described by a  $2 \times 2$  effective Hamiltonian  $\mathcal{H}$  which is not Hermitian to allow for decays:

$$\mathcal{H} = \mathbf{M} - \frac{i}{2}\mathbf{\Gamma}, \quad (1.15)$$

where the diagonal elements of  $\mathbf{M}$  and  $\mathbf{\Gamma}$  are associated with the flavour conserving transitions  $B_s \rightarrow B_s$  and  $\bar{B}_s \rightarrow \bar{B}_s$ , while the off-diagonal elements are associated to flavour changing transitions  $B_s \rightarrow \bar{B}_s$  and  $\bar{B}_s \rightarrow B_s$ . The heavy and light mass eigenstates which are the eigenvectors of  $\mathcal{H}$  can be constructed:

$$|B_s^L\rangle = p \cdot |B_s\rangle + q \cdot |\bar{B}_s\rangle \quad (1.16)$$

$$|B_s^H\rangle = p \cdot |B_s\rangle - q \cdot |\bar{B}_s\rangle, \quad (1.17)$$

with  $|p|^2 + |q|^2 = 1$  for normalisation. Based on the fact that no Lorentz-invariant quantum field theory can be build with a Hermitian Hamiltonian that violates CPT, CPT conservation is assumed here. The two mass eigenstates have a mass difference

$$\Delta m_s = m_s^H - m_s^L > 0 \quad (1.18)$$

and a total decay width difference

$$\Delta\Gamma_s = \Gamma_s^H - \Gamma_s^L. \quad (1.19)$$

In case of CP conservation  $|p/q| = 1$  holds, and the differences are given as  $\Delta m_s = 2|M_{12}|$  and  $\Delta\Gamma_s = 2|\Gamma_{12}|$ , where  $M_{12}$  and  $\Gamma_{12}$  are the off-diagonal elements of  $\mathbf{M}$  and  $\mathbf{\Gamma}$ .

Thus the time evolution of an initially pure flavour eigenstate  $|B_s\rangle$  ( $|\bar{B}_s\rangle$ ) is given by the Schrödinger equation:

$$i\hbar\frac{\partial}{\partial t}|B_s(t)\rangle = \mathcal{H}|B_s(t)\rangle, \quad (1.20)$$

leading to

$$|B_s(t)\rangle = g_+(t)|B_s\rangle + \frac{q}{p}g_-(t)|\bar{B}_s\rangle, \quad (1.21)$$

$$|\bar{B}_s(t)\rangle = g_+(t)|\bar{B}_s\rangle + \frac{p}{q}g_-(t)|B_s\rangle, \quad (1.22)$$

where the probabilities of flavour states staying unchanged (+) or oscillating into the other (−) are

$$g_{\pm}(t) = \frac{1}{2}\left(e^{-im_H t - \frac{1}{2}\Gamma_H t} \pm e^{-im_L t - \frac{1}{2}\Gamma_L t}\right). \quad (1.23)$$

## 1.2.2 Classification of CP violating effects

Three types of CP violating effects can be distinguished in meson decays:

CP violation in decays is present if the decay amplitude  $A_f$  of a meson  $M$  into a final state  $f$  is different from the CP conjugate decay  $\bar{A}_{\bar{f}}$  of the antiparticle  $\bar{M}$  into the final state  $\bar{f}$ :

$$\left|\frac{\bar{A}_{\bar{f}}}{A_f}\right| \neq 1. \quad (1.24)$$

In charged meson decays, where no mixing can occur, this is the only possible source of CP asymmetries.

CP violation in mixing is defined by

$$\left|\frac{q}{p}\right| \neq 1, \quad (1.25)$$

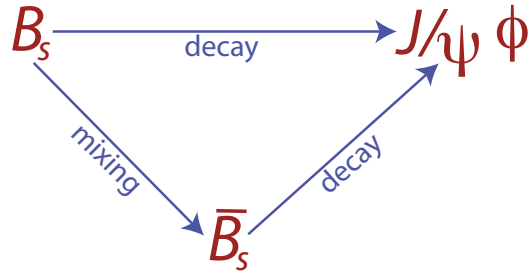


**Figure 1.4:** An example for interference between decay and mixing the system of  $B_s$  mesons.

and can be measured by the asymmetry of wrong-sign semileptonic decays induced by oscillations.

*CP violation in interference* occurs if there is an interference between the direct decay without mixing,  $M^0 \rightarrow f$ , and a decay with mixing,  $M^0 \rightarrow \bar{M}^0 \rightarrow f$ , which occur only if the final state is common to both,  $M^0$  and  $\bar{M}^0$  (see Fig. 1.4). This is defined by

$$\mathcal{I}m(\lambda_f) \neq 0, \quad (1.26)$$

with

$$\lambda_f = \frac{q\bar{A}_f}{pA_f}. \quad (1.27)$$

### 1.2.3 Helicity amplitudes

In the decay  $B_s \rightarrow J/\psi \phi$  *CP* violation through mixing can occur as shown in Fig. 1.4. The decay mainly occurs through  $b(\bar{s}) \rightarrow c\bar{c}s(\bar{s})$  transitions as illustrated in Fig. 1.5. Since this process is dominated by a single CKM amplitude ( $V_{cb}$ ) it is an excellent decay to study mixing-induced *CP* violation.

In the Standard Model it is expected that  $|p/q| \approx 1$ , meaning that the light  $B_s$  mass eigenstate  $B_s^L$  is nearly a pure *CP*-even state, and the heavy eigenstate  $B_s^H$  is a pure *CP*-odd state. In case of the decay  $B_s \rightarrow J/\psi \phi$  the final state is a composition of *CP*-odd and *CP*-even states [6, 7, 8]. Because the  $B_s$  is a pseudoscalar ( $J^P = 0^-$ ) and both  $J/\psi$  and  $\phi$  are vector mesons ( $J^{PC} = 1^{--}$ ), the orbital angular momentum between the two decay products can have the values  $L = 0, 1, 2$ . Thus one can define three amplitudes with different angular dependencies:  $A_0(t)$  (for  $L = 0$ ) is *CP*-even and longitudinally polarised, where the two transversely polarised amplitudes,  $A_\perp(t)$  (for  $L = 1$ ) is *CP*-odd and  $A_\parallel(t)$  for ( $L = 2$ ) is *CP*-even. In this context, longitudinal means that both vector mesons are longitudinally polarised with respect to the decay axis and transversal means that both are transversally polarised with respect to the

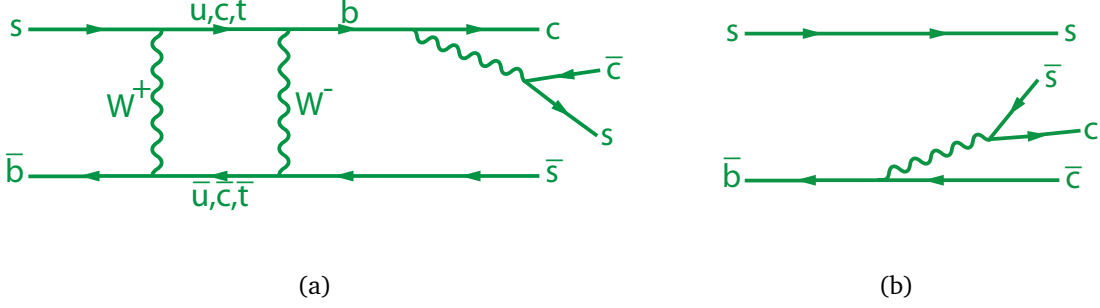


**Figure 1.5:**  $B_s \rightarrow J/\psi \phi$  decays can happen after mixing (a) and before (b).

decay axis, in one case with the linear polarisation vectors parallel ( $\parallel$ ) and in the other perpendicular ( $\perp$ ) to each other.

The differential decay rate can be written as

$$\frac{d^4\Gamma(B_s(t))}{d\Theta dt} = f(\Theta, \alpha, t) = \sum_{i=1}^6 O_i(\alpha, t) \cdot g_i(\Theta), \quad (1.28)$$

where  $O_i$  are kinematics-independent observables and  $g_i$  the angular distributions. The set of physical parameters is represented by  $\alpha$  and the angles which define the kinematics are generically denoted by  $\Theta$ . The time evolution of the different observables is given by bilinear combinations of the polarization amplitudes. For a sample of  $B_s \rightarrow J/\psi(\rightarrow \mu^+\mu^-)\phi(\rightarrow K^+K^-)$  decays without distinction whether a  $B_s$  or  $\bar{B}_s$  was produced, these are [7]:

$$\begin{aligned} O_1 &= |A_0(t)|^2 \\ &= |A_0(0)|^2 \left[ e^{-\Gamma_L t} + e^{-\Gamma_H t} - |\cos \phi_s| \left( e^{-\Gamma_H t} - e^{-\Gamma_L t} \right) \right], \\ O_2 &= |A_{\parallel}(t)|^2 \\ &= |A_{\parallel}(0)|^2 \left[ e^{-\Gamma_L t} + e^{-\Gamma_H t} - |\cos \phi_s| \left( e^{-\Gamma_H t} - e^{-\Gamma_L t} \right) \right], \\ O_3 &= |A_{\perp}(t)|^2 \\ &= |A_{\perp}(0)|^2 \left[ e^{-\Gamma_L t} + e^{-\Gamma_H t} + |\cos \phi_s| \left( e^{-\Gamma_H t} - e^{-\Gamma_L t} \right) \right], \\ O_4 &= \mathcal{I}m(A_{\parallel}^*(t)A_{\perp}(t)) \\ &= -|A_{\parallel}(0)||A_{\perp}(0)| \cos(\delta_1) \sin \phi_s (e^{-\Gamma_H t} - e^{-\Gamma_L t}), \\ O_5 &= \mathcal{R}e(A_0^*(t)A_{\parallel}(t)) \\ &= |A_0(0)||A_{\parallel}(0)| \cos(\delta_2 - \delta_1) \left[ e^{-\Gamma_L t} + e^{-\Gamma_H t} - |\cos \phi_s| \left( e^{-\Gamma_H t} - e^{-\Gamma_L t} \right) \right], \\ O_6 &= \mathcal{I}m(A_0^*(t)A_{\perp}(t)) \\ &= -|A_0(0)||A_{\perp}(0)| \cos(\delta_2) \sin \phi_s (e^{-\Gamma_H t} - e^{-\Gamma_L t}). \end{aligned} \quad (1.29)$$

The width difference is defined as  $\Delta\Gamma_s = \Gamma_s^H - \Gamma_s^L$  and the mean is  $\bar{\Gamma}_s = (\Gamma_s^H + \Gamma_s^L)/2$ . Since the overall phase of the polarization states is not observable, two strong phases are defined as  $\delta_1 \equiv \arg |A_{\parallel}^* A_{\perp}|$  and  $\delta_2 \equiv \arg |A_0^* A_{\perp}|$ . These are CP conserving, and

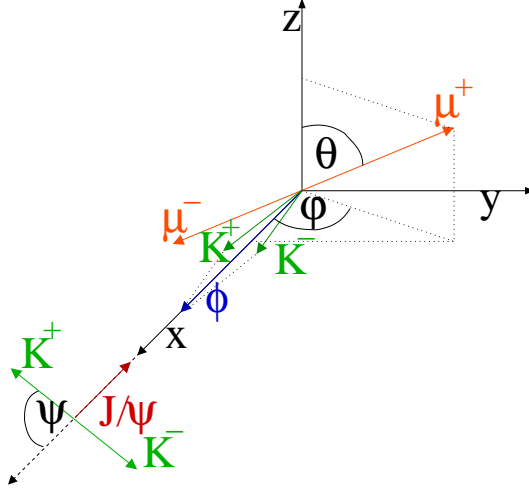


**Figure 1.6:** Definition of the three physical angles used to describe the decay.

are expected to be 0 (mod  $\pi$ ) in the absence of final-state interactions [7]. Here,  $A_0(0)$ ,  $A_{\parallel}(0)$  and  $A_{\perp}(0)$  are the magnitudes of the amplitudes at  $t = 0$ , with the constraint  $|A_0(0)|^2 + |A_{\parallel}(0)|^2 + |A_{\perp}(0)|^2 = 1$  to ensure the correct normalization of the probability density function. Assuming  $SU(3)$  flavour-symmetry, the magnitudes and the two strong phases are equal for the decay  $B_s \rightarrow J/\psi \phi$  and  $B_d \rightarrow J/\psi K^*$  in unmixed samples [7]. The measurement of these parameters is of interest to study and improve the phenomenological models used to calculate all hadronic effects.

In these decays the kinematics are uniquely defined by a set of three angles. The transversity basis is used in this analysis, in which the set of variables is  $\Theta = (\cos \theta, \psi, \cos \varphi)$ . In this base  $(\theta, \varphi)$  are the polar and azimuthal angles of the momentum of the  $\mu^+$  in the  $J/\psi$  rest frame. This coordinate system is defined such that the  $\phi$  moves in the positive  $x$  direction and the  $z$  axis is perpendicular to the plane of the decay  $\phi \rightarrow K^+K^-$  as seen from the rest frame of the  $J/\psi$  (Fig. 1.6). Unit vectors and the aforementioned angles can be written in terms of the unit momentum vectors  $\mathbf{p}$  of the involved particles as follows:

$$\begin{aligned}
 \mathbf{x} &= \mathbf{p}_{\phi}, \\
 \mathbf{y} &= \frac{\mathbf{p}_{K^+} - \mathbf{p}_{\phi}(\mathbf{p}_{\phi} \cdot \mathbf{p}_{K^+})}{|\mathbf{p}_{K^+} - \mathbf{p}_{\phi}(\mathbf{p}_{\phi} \cdot \mathbf{p}_{K^+})|}, \\
 \mathbf{z} &= \mathbf{x} \times \mathbf{y}, \\
 \sin \theta \cos \varphi &= \mathbf{p}_{\mu^+} \cdot \mathbf{x}, \\
 \sin \theta \sin \varphi &= \mathbf{p}_{\mu^+} \cdot \mathbf{y}, \\
 \cos \theta &= \mathbf{p}_{\mu^+} \cdot \mathbf{z}.
 \end{aligned} \tag{1.30}$$

The angle  $\psi$  is defined in the rest frame of the  $\phi$  as the negative cosine of the angle between the  $K^+$  direction and the  $J/\psi$  direction:

$$\cos \psi = -\mathbf{p}_{K^+} \cdot \mathbf{p}_{J/\psi}. \tag{1.31}$$

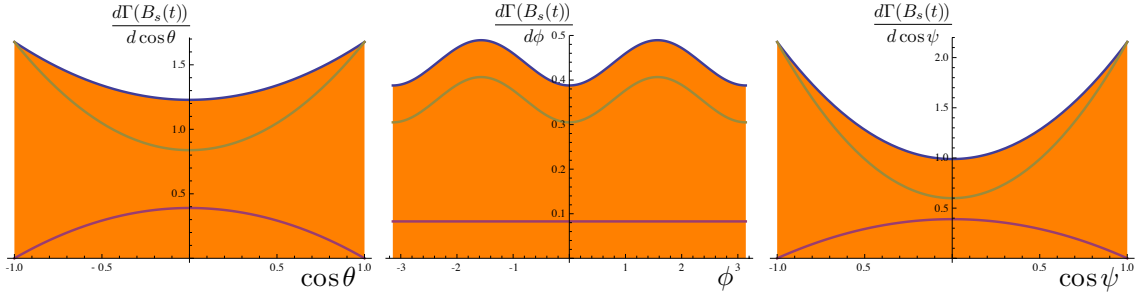


**Figure 1.7:** Projections of the differential decay rate  $d^4\Gamma(B_s(t))/d\Theta dt$  on the three angular axes. The  $CP$ -even and  $CP$ -odd contributions are indicated by the green and pink line respectively. Input values used are given in Tab. 1.1.

The individual angular distributions in Eq. 1.28 are then given by the following combinations of trigonometric functions [7]:

$$\begin{aligned}
 g_1 &= 2 \cos^2 \psi (1 - \sin^2 \theta \cos^2 \varphi), \\
 g_2 &= \sin^2 \psi (1 - \sin^2 \theta \sin^2 \varphi), \\
 g_3 &= \sin^2 \psi \sin^2 \theta, \\
 g_4 &= \sin^2 \psi \sin 2\theta \sin \varphi, \\
 g_5 &= 1/\sqrt{2} \sin 2\psi \sin^2 \theta \sin 2\varphi, \\
 g_6 &= 1/\sqrt{2} \sin 2\psi \sin 2\theta \cos \varphi.
 \end{aligned} \tag{1.32}$$

The differential decay rate as function of only one angle at a time is presented in Fig. 1.7 with the  $CP$ -even and  $CP$  odd contributions displayed separately with input values from Tab. 1.1.

**Table 1.1:** Input values for the  $B_s$  mixing parameters, decay amplitudes, strong and weak phases in the simulation of the  $B_s \rightarrow J/\psi\phi$  Monte Carlo sample [9].

parameter	assumed value
$\tau_s = 1/\bar{\Gamma}_s$	$1.405 \times 10^{-12}$ s
$\Delta\Gamma_s/\bar{\Gamma}_s$	-0.2
$\Delta m_s$	$17.8 \text{ ps}^{-1}$
$ A_0(0) ^2/\Gamma_s$	0.570
$ A_{\parallel}(0) ^2/\Gamma_s$	0.217
$ A_{\perp}(0) ^2/\Gamma_s$	0.213
$\delta_1$	$\pi$
$\delta_2$	0
$\phi_s$	-0.04

### 1.2.4 Predictions from the Standard Model

In the  $B_s \rightarrow J/\psi(\rightarrow \mu^+\mu^-)\phi(\rightarrow K^+K^-)$  analysis the parameters of greatest interest are the width difference  $\Delta\Gamma_s = \Gamma_s^H - \Gamma_s^L$  and the weak phase  $\phi_s$ . The width difference can be written as [3]

$$\begin{aligned} \Delta\Gamma_s &\approx 2|\Gamma_{12}| & (1.33) \\ &= \frac{G_F^2 m_b^2 \eta'_B m_{B_s} B_{B_s} f_{B_s}^2}{4\pi} \left[ (V_{ts}^* V_{tb})^2 + V_{ts}^* V_{tb} V_{cs}^* V_{cb} \mathcal{O}\left(\frac{m_c^2}{m_b^2}\right) + (V_{cs}^* V_{cb})^2 \mathcal{O}\left(\frac{m_c^4}{m_b^4}\right) \right], \end{aligned}$$

where  $G_f$  is the Fermi constant,  $m_W$  the  $W$  boson mass and  $m_b$  and  $m_c$  the masses of the  $b$ - and  $c$ -quark;  $m_{B_s}$ ,  $f_{B_s}$  and  $B_{B_s}$  are the  $B_s$  mass, weak decay constant and bag parameter, respectively. The QCD correction  $\eta'_B$  is of order unity. The result is expected to be  $\Delta\Gamma = -(0.147 \pm 0.060) \cdot \Gamma_s = -(0.096 \pm 0.039) \text{ ps}^{-1}$  [10].

The weak phase is directly connected to the height of the unitarity triangle by

$$\begin{aligned} \phi_s &= \left[ \arg(V_{cs}^* V_{cb}) - \arg(V_{ts}^* V_{tb}) \right] & (1.34) \\ &= 2\lambda^2 \eta. \end{aligned}$$

On the other hand  $\phi_s$  is directly connected to the angle  $\beta_s$  in the nearly degenerate  $s$ -quark CKM triangle:

$$\phi_s = -2\beta_s. \quad (1.35)$$

$\phi_s$  is expected to be very small in the Standard Model, theoretical calculations predict  $\phi_s = (4.2 \pm 1.4) \cdot 10^{-3}$  [10] while the CKMFitter group evaluates  $0.96^\circ < \beta_s < 1.13^\circ$  at 95% CL resulting in  $\phi_s \approx -(0.04 - 0.03)$  using measured Standard Model parameters as input [4]. But most models beyond the Standard Model would significantly increase this number making it an interesting quantity to measure.

## 1.3 $b$ -hadron production at the LHC

In contrast to  $e^+e^-$  colliders where  $b$ -meson production is mainly a simple process, such as  $e^+e^- \rightarrow Z \rightarrow B\bar{B}$  for the LEP experiments, or  $e^+e^- \rightarrow \Upsilon(4s) \rightarrow B\bar{B}$  at  $b$ -factory experiments, Babar and Belle,  $b$ -hadron production at hadron colliders as LHC or Tevatron is more complicated. A  $b$ -quark is produced in the proton-(anti)proton collision, which can be divided in three main processes: *flavour creation*, *flavour excitation* and *gluon splitting* [11]. Those will be described in the following.

*Flavour creation* or *pair creation* is the leading order process in  $\alpha_s$  and can be subdivided in gluon-gluon fusion  $gg \rightarrow b\bar{b}$  (Fig. 1.8) and light quark annihilation  $q\bar{q} \rightarrow b\bar{b}$  (Fig. 1.9) with gluon-gluon fusion being the more dominant one. Since the  $b$  and

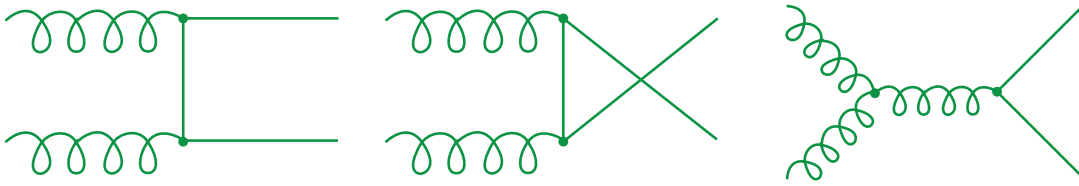


**Figure 1.8:** Leading order  $\mathcal{O}(\alpha_s^2)$  diagrams for  $b\bar{b}$  production in gluon-gluon fusion.

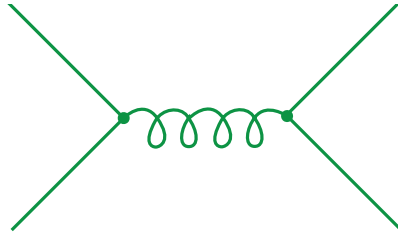


**Figure 1.9:** Leading order  $\mathcal{O}(\alpha_s^2)$  diagram for  $b\bar{b}$  production in quark-antiquark annihilation.

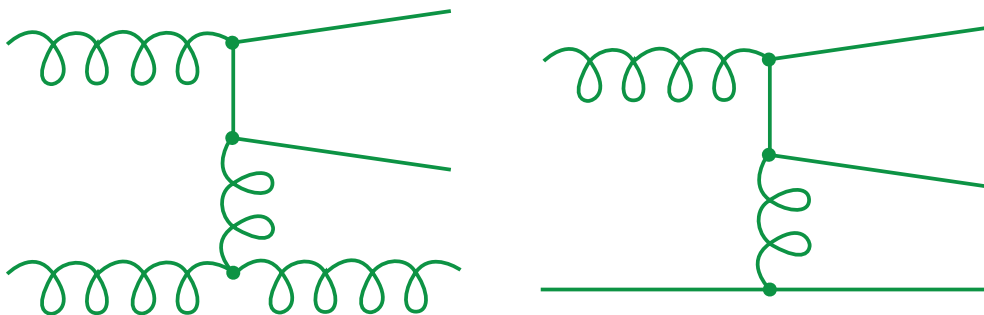
$\bar{b}$  quarks are produced back-to-back in their centre-of-mass frame, they will also be back-to-back in the plane transverse to the beam direction, resulting in two well-separated  $b$ -jets in the detector.

*Flavour excitation* is a next-to-leading order process in which a parton of one of the colliding protons is scattered off a  $b$ -quark which is present in the quark sea of the other proton (Fig. 1.10). Being a sea  $b$ -quark it must originate from  $g \rightarrow b\bar{b}$ . Since usually only one of the  $b$ -quarks undergoes hard QCD scatter, the other will proceed in the initial proton direction and escape undetected.

*Gluon splitting* is another next-to-leading order process in which the  $b\bar{b}$  pair is produced by a virtual gluon (Fig. 1.11). The two  $b$ -quarks tend to be very close together in phase-space. Their decay products may appear to come from a single parent.

The dominant contribution to the  $b\bar{b}$  cross-section at the LHC will not be the leading order process, but the next-to-leading order flavour excitation process (Fig. 1.10), followed by pair production (Fig. 1.8 and 1.9) and then gluon splitting (Fig. 1.11). Fig. 1.12 shows the total cross section for  $b$  production as a function of  $\sqrt{s}$  [11].

**Figure 1.10:** Next-to-leading order  $\mathcal{O}(\alpha_s^3)$  diagrams for  $b\bar{b}$  production in flavour excitation.





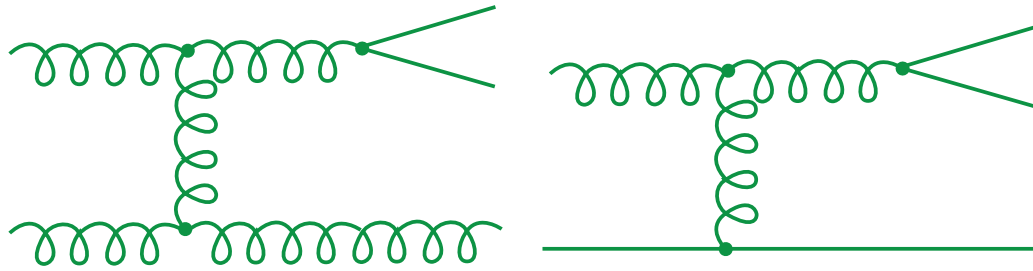


**Figure 1.11:** Next-to-Leading order  $\mathcal{O}(\alpha_s^3)$  diagrams for  $b\bar{b}$  production in gluon splitting.

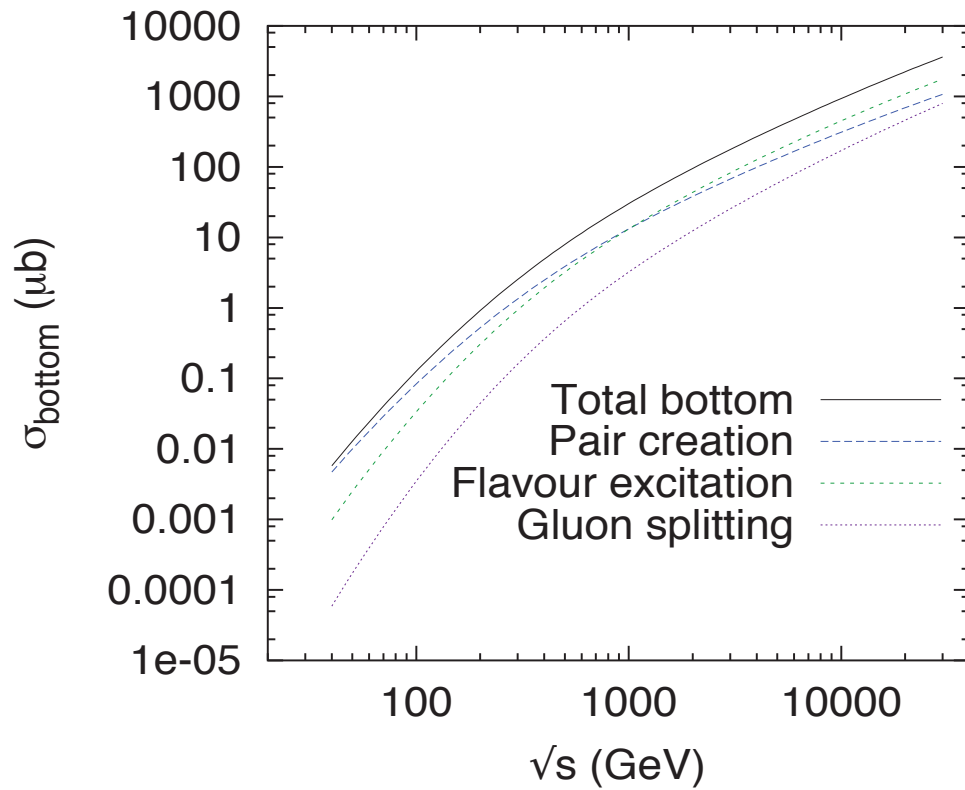


**Figure 1.12:** The total bottom cross sections for  $pp$  collisions as a function of  $E_{CM} = \sqrt{s}$ . The contributions from pair creation, flavour excitation and gluon splitting are shown separately [11].

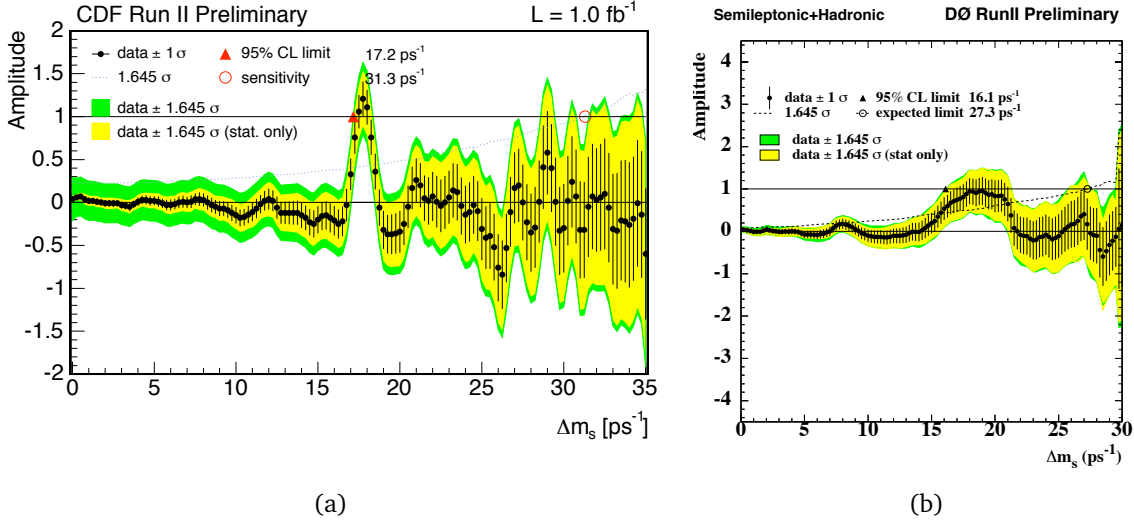


**Figure 1.13:** Results of the Amplitude Scan for a combination of all analyses  $B_s$  decays for CDF (a) and D0 (b); from [13] and [15].

Once the  $b\bar{b}$  pair is produced in the proton-proton collision, both fragmentise into  $b$ -hadrons. The probability of a quark  $Q$  to fragment into a meson of type  $Q\bar{q}$  is given by the fragmentation-function. From this, one can derive the probability that a certain meson is produced from a  $b(\bar{b})$  quark. In case of  $B_s$  production at the LHC this is expected to be  $B(\bar{b} \rightarrow B_s) = (10.7 \pm 1.1)\%$ . The experimentally measured branching ratios for the full decay are [12]

$$\mathcal{B}(B_s \rightarrow J/\psi \phi) = (9.3 \pm 3.3) \cdot 10^{-4}, \quad (1.36)$$

$$\mathcal{B}(J/\psi \rightarrow \mu^+ \mu^-) = (5.88 \pm 0.10) \cdot 10^{-2}, \quad (1.37)$$

$$\mathcal{B}(\phi \rightarrow K^+ K^-) = (49.1 \pm 0.6) \cdot 10^{-2}. \quad (1.38)$$

## 1.4 Results on the $B_s$ system from Tevatron

The  $b$ -factories Babar and Belle run below the threshold of  $B_s \bar{B}_s$  production. The best results on  $B_s$  mixing come from the Tevatron. The first observation of  $B_s - \bar{B}_s$  oscillations has been made by the CDF experiment for 1 fb<sup>-1</sup> [13]. They use the amplitude method given in [14] to extract  $\Delta m_s = 17.77 \pm 0.10(\text{stat}) \pm 0.07(\text{sys}) \text{ ps}^{-1}$  with a  $5\sigma$  oscillation significance (Fig. 1.13(a)). More recently, D0 obtained with 2.4 fb<sup>-1</sup> an independent  $2.9\sigma$  evidence for  $B_s$  oscillations with  $\Delta m_s = 18.53 \pm 0.93(\text{stat}) \pm 0.30(\text{sys}) \text{ ps}^{-1}$  [15] consistent with the CDF measurement (Fig. 1.13(b)).

To measure  $\Delta\Gamma_s$  and the  $CP$  violating phase  $\phi_s$  CDF and D0 analysed 2.8 fb<sup>-1</sup> of data. The angular distribution of  $B_s \rightarrow J/\psi(\rightarrow \mu^+ \mu^-)\phi(\rightarrow K^+ K^-)$  decays (Section 1.2.3) was used to extract these values with an unbinned maximum likelihood fit. Assuming

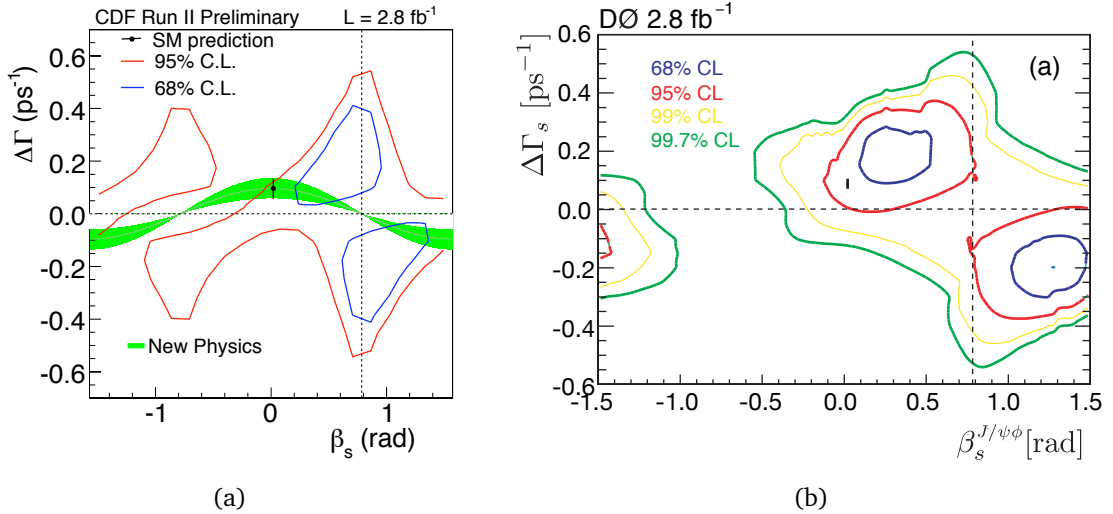


**Figure 1.14:** Confidence intervals on the  $\Delta\Gamma - \beta_s$  plane obtained by CDF (a) and D0 (b). Note that  $\phi_s = -2\beta_s$ . The green band in (a) indicates the possible regions for new physics; from [1] and [16].

no  $CP$  violation ( $\phi_s = 0$ ) CDF measures  $\Delta\Gamma_s = 0.02 \pm 0.05(\text{stat.}) \pm 0.01(\text{sys.}) \text{ ps}^{-1}$  [1] and D0  $\Delta\Gamma_s = 0.085^{+0.072}_{-0.078}(\text{stat.}) \pm 0.06(\text{sys.}) \text{ ps}^{-1}$  [2]. Results for a fit with  $\phi_s$  as a free parameter are presented in confidence intervals in Fig. 1.14(a) as the errors are non Gaussian. CDF observes a  $1.8\sigma$  deviation [1] from the expected SM values and D0 observes a  $1.7\sigma$  deviation [16]. The Standard Model predictions ( $\Delta\Gamma_s = 0.096 \pm 0.039 \text{ ps}^{-1}$  and  $\phi_s = (4.2 \pm 1.4) \cdot 10^{-3}$ ) are taken from [10]. It is interesting to note that both experiments observe similar shifts from the SM prediction. New measurements are therefore necessary to confirm or to rule out this deviation.

## 1.5 Summary

In this Chapter the CKM mechanism and how it enables  $B_s - \bar{B}_s$  mixing and  $CP$  violation was introduced. Then the possibility to extract parameters such as  $\Delta\Gamma_s$  and  $\phi_s$  in an angular analysis of  $B_s \rightarrow J/\psi(\rightarrow \mu^+\mu^-)\phi(\rightarrow K^+K^-)$  decays was presented. Latest Tevatron results show a precise measurement of  $\Delta m_s$  whereas the uncertainties on the  $\Delta\Gamma_s$  and  $\phi_s$  are still large with an interesting deviation of almost  $2\sigma$  from the expected Standard Model prediction. This shows that further studies of these quantities are of great importance. The high  $b$ -hadron cross section at the LHC will make CMS a factory for  $b$ -hadrons, thus also for  $B_s$  mesons. With the branching ratios given in section 1.3 a total of 2.88 million  $B_s \rightarrow J/\psi(\rightarrow \mu^+\mu^-)\phi(\rightarrow K^+K^-)$  events is expected for  $1 \text{ fb}^{-1}$  (without any kinematic selection cuts).



# Chapter 2

## LHC and the CMS experiment

### 2.1 The Large Hadron Collider

The Large Hadron Collider (LHC) at CERN in Geneva will be operating at the end of 2009. It will give the possibility to investigate physics at a new energy range, including the search for the Higgs boson and phenomena beyond the Standard Model, such as Supersymmetry.

In order to accelerate protons to an energy of 7 TeV and to reach the design luminosity of  $10^{34} \text{ cm}^{-2}\text{s}^{-1}$ , several accelerators are used (Fig. 2.1). Protons with an energy of 50 MeV are generated in the LINAC2, a linear particle accelerator. In the Proton Synchrotron Booster (PSB), they are accelerated to 1.4 GeV and then injected into the Proton Synchrotron (PS), where they reach an energy of 26 GeV. The Super Proton Synchrotron further accelerates them to the LHC injection energy of 450 GeV. The protons are accumulated in the LHC ring over a period of 20 minutes and then accelerated to their peak energy of 7 TeV in another 20 minutes. They will circulate for up to 24 hours in the ring, colliding at the four intersection points where the experiments are located.

The LHC [17, 18, 19] itself is situated in the former Large Electron Positron (LEP) tunnel constructed between 1983 and 1988. It has a circumference of 27 km and is approximately 100 m below the ground. Eight arcs with a length of 2.5 km each and eight straight sections of 530 m make up the ring. The four experiments, ATLAS and CMS (as multi-purpose high energy experiments), LHCb looking for quark mixing and CP violation and ALICE investigating heavy ion collisions are hosted in four of the eight straight sections.

Due to the high center-of-mass energy of 14 TeV, a magnetic dipole field of 8.3 T is needed [17], making it necessary to use super-conducting (NbTi) magnets with super-fluid helium cooling. As the LHC is a proton-proton collider, two rings are

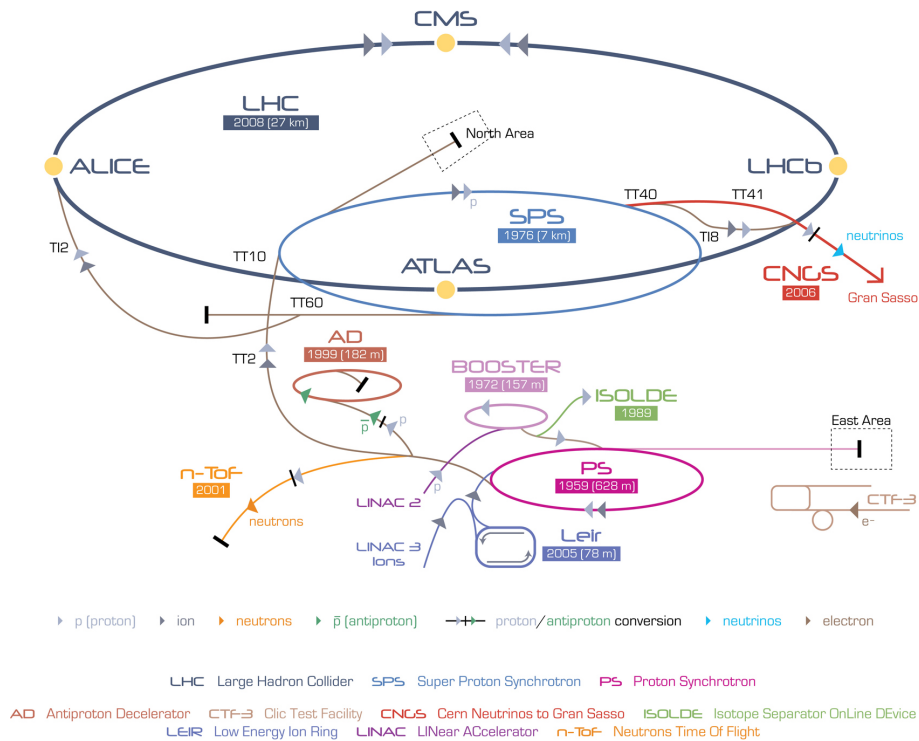


**Figure 2.1:** The different accelerators at CERN which are used for the LHC, see text, and other CERN facilities (courtesy CERN).

needed, to be hosted in the limited space of the LEP tunnel with a diameter of 3.8 m. Therefore the two rings are embedded in a single magnetic structure with two sets of superconducting coils and a common yoke, see Fig. 2.2 and 2.3.

On 10 September 2008, the first beam at 450 GeV circulated around the 27 km LHC ring. Unfortunately, 9 days later a serious incident occurred while raising the currents in the magnets, postponing the first collisions in the LHC for more than one year. The incident was due to a faulty electrical connection, damaging 29 magnets and causing loss of approximately six tons of liquid helium. 53 dipole magnets needed to be lifted to ground in order to be cleaned or replaced. Furthermore, additional safety systems will be installed to minimise damage in the event of another incident. The first beam is planned for November 2009 with first collisions a few weeks later at a center-of-mass energy of 7 TeV.

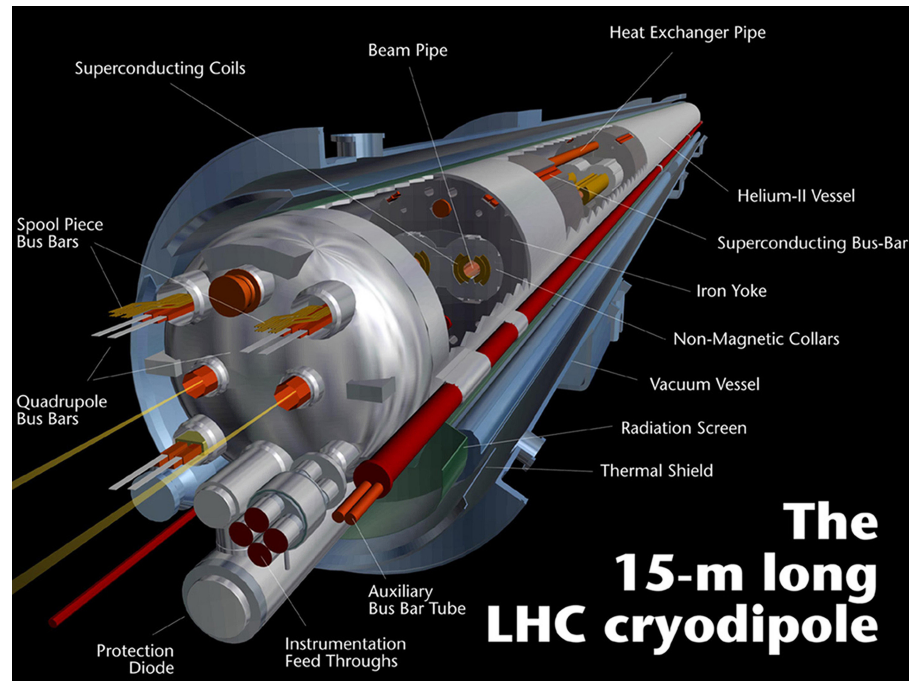


**Figure 2.2:** An artistic view of the LHC cryogenic dipoles containing the two beam-pipes (courtesy CERN).

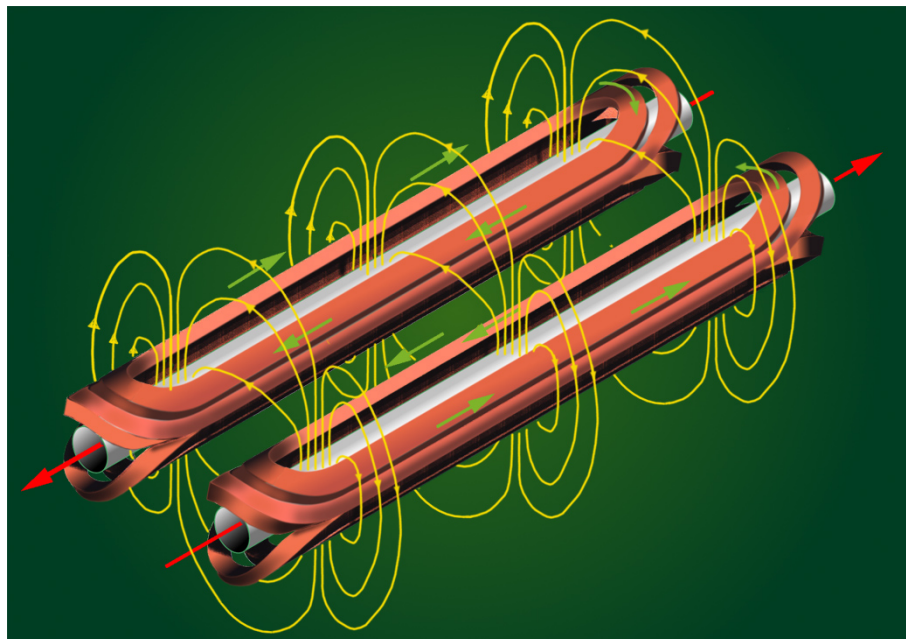


**Figure 2.3:** The magnetic field in the LHC dipoles deflecting the protons in two beam-pipes running in opposite direction (courtesy CERN).

## 2.2 The CMS detector

The Compact Muon Solenoid (CMS) is one of the two multi-purpose experiments at LHC [20]. One of its goals is to clarify the nature of electroweak symmetry breaking for which the Higgs mechanism is supposedly responsible. At the beginning, measurements of known properties of particles such as mass and width of  $b$ -mesons,  $J/\psi$  and  $\Upsilon$  or  $W^\pm$  and  $Z$  will ensure that the detector is understood.

At a centre-of-mass energy of  $\sqrt{s} = 14$  TeV, the total  $p\bar{p}$  cross section is  $\sigma \approx 100$  mb, leading to about  $10^9$  inelastic events per second at the LHC design luminosity of  $\mathcal{L} = 10^{34} \text{ cm}^{-2}\text{s}^{-1}$ . A high performance trigger is needed to reduce this rate to about 100 events per second, which is the rate at which events can be stored. The detector components have to be fast since collisions happen every 25 ns producing 1000 charged tracks on average. Thus high granularity with good time resolution is needed to ensure low occupancy. This results in a high number of detector channels. The high rate of particles requires also that detectors and readout electronics are radiation hard.

From the physics point of view, further requirements should be satisfied: muons should be well identified and their momentum measured with high precision ( $\mathcal{O}(1\%)$ ) from a few GeV to 1 TeV. A good momentum resolution and charge identification for charged particles is necessary as well as a precise vertex reconstruction to identify long-lived particles such as  $b$ -mesons and  $\tau$ -leptons. Furthermore, a good energy resolution is desirable for electromagnetic objects such as electrons and photons as well as for hadronic objects. A fine granularity to achieve good isolation is also mandatory.

The coordinate system adopted by CMS has its origin centered at the nominal collision point in the detector centre, the  $y$ -axis pointing upwards, and the  $x$ -axis pointing radially inwards towards the center of the LHC. Thus, the  $z$ -axis points along the beam direction towards the Jura mountains from LHC Point 5. The azimuthal angle  $\phi$  is measured from the  $x$ -axis in the  $x - y$  plane and the radial coordinate in this plane is denoted by  $r$ . The polar angle  $\theta$  is measured from the  $z$ -axis. The pseudorapidity is defined as  $\eta = -\ln \tan(\theta/2)$ . Thus, momentum and energy transverse to the beam direction, denoted by  $p_T$  and  $E_T$ , respectively, are computed from the  $x$  and  $y$  components. The imbalance of energy measured in the transverse plane is denoted by  $E_T^{\text{miss}}$ .

The general layout of the CMS detector (Fig. 2.4) is that of a standard multi-purpose particle physics detector, measuring all particles produced in the primary interaction (except neutrinos) with an almost hermetic coverage. An important design decision for such a detector is the choice of the magnetic field configuration which has great importance for the measurement of the momentum of muons and other charged particles. Since a large bending power is needed to measure precisely the momentum of high energy particles, superconducting magnet technology is used for the CMS mag-



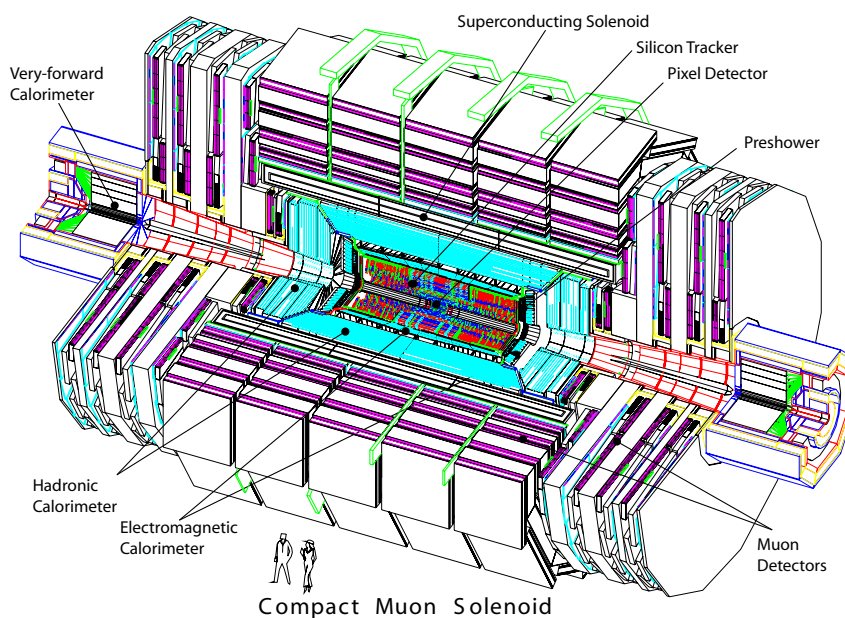


**Figure 2.4:** A perspective view of the CMS detector [20].

net. This is realised by a 3.8 T solenoid with an iron return yoke embedded in the outermost detector components, the muon detectors. This design led to the name of CMS, which is small (21.6 m long with 14.6 m diameter) but heavy (12500 t) compared to its LHC counterpart ATLAS (7000 t, 44 m length, 25 m height [21]). The detector components are arranged cylindrically around the beam-pipe, with a barrel part in the centre and endcaps at both ends, as can be seen in Fig. 2.4 and 2.5. The detector was pre-assembled on the surface in 5 barrel wheels and 3 endcap disks for each end. Taking into account the very limited space underground this facilitated the construction making simultaneous work on different detector components possible. In addition, the modular design allows to move the different substructures apart from each other to access and maintain the innermost detectors, if necessary.

The tracking and parts of the calorimetry systems are hosted inside the coil. The total tracking volume is 5.8 m long and 2.6 m in diameter. The innermost tracking detector is the silicon pixel detector, located only 4 cm from the beam-line and made of 3 barrel layers and 2 disks at each end. It is followed by the second tracking device, the silicon strip detector, using 10 barrel layers and 12 disks of silicon strips.

The electromagnetic calorimeter (ECAL) is made of lead tungstate ( $\text{PbWO}_4$ ) crystals with a coverage in pseudorapidity up to  $|\eta| = 3.0$ . The scintillation light is detected by silicon avalanche photodiodes (APDs) in the barrel region and vacuum phototriodes (VPTs) in the endcap region which can operate in the strong magnetic field. Its thickness is at least 25 radiation lengths. To reject  $\pi^0$  decays, a pre-shower system is installed in front of the endcap ECAL.

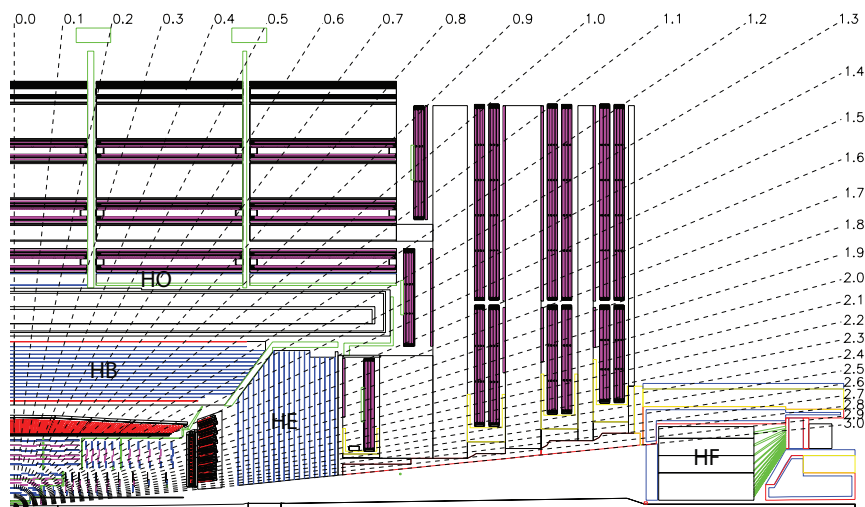


**Figure 2.5:** Schematic  $r - z$  view of the CMS detector. The dotted lines indicate the angle  $\theta$  labelled by the corresponding pseudorapidity.

The hadronic calorimeter (HCAL) which covers a pseudorapidity range of up to  $|\eta| = 3.0$  is a brass/scintillator sampling calorimeter with a barrel (HB) and endcap (HE) component. Light produced in the scintillator is channelled to hybrid photodiodes via optical fibres. To improve the containment of hadronic showers in the barrel part, an outer calorimeter is placed outside the solenoid coil, operating as tail catcher for late starting showers. Thus the HCAL covers nearly 11 interaction lengths over the full pseudorapidity range. A coverage up to  $|\eta| = 5$  is provided by an iron/quartz-fibre calorimeter (HF) where the Cherenkov light emitted by quartz-fibres is detected by photomultipliers.

In Fig. 2.6 a photo of the insertion of the silicon strip tracker into the CMS detector is shown. First cosmic events with the full CMS detector in autumn 2008. Fig. 2.7 shows a cosmic muon traversing the full detector, producing hits in all detector components including the silicon pixel detector.

The next paragraphs describe in detail the detector components of importance for this analysis. First the solenoid will be discussed in Section 2.2.1, then the inner tracking system will be outlined in Section 2.2.2, with particular emphasis on the silicon pixel detector, since the measurement of the Lorentz drift in the silicon pixel modules (see Chapter 3) was part of this work and because this detector is crucial to measure secondary vertices. The muon detectors will be introduced in Section 2.2.3 followed by the trigger system for the CMS detector in Section 2.2.4.

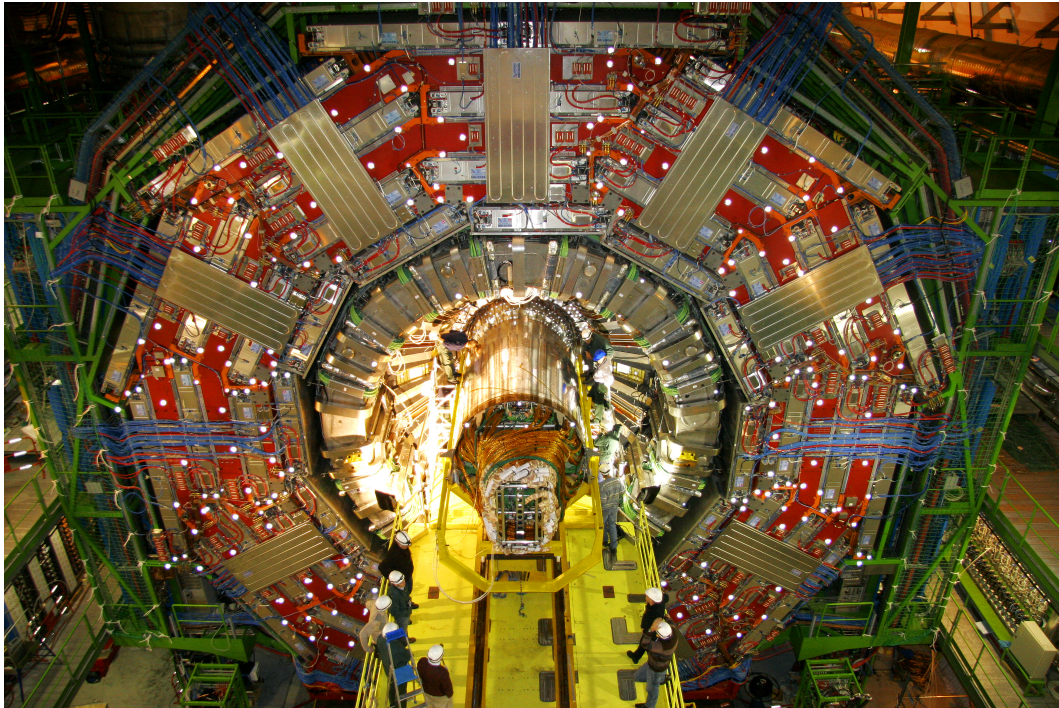


**Figure 2.6:** *The CMS detector in the underground cavern during insertion of the silicon strip tracker (courtesy CERN).*

### 2.2.1 The solenoid

This part of the detector is of great importance to this analysis since it enables the transverse momentum measurement of charged particles such as muons and kaons used in the  $B_s \rightarrow J/\psi(\rightarrow \mu^+\mu^-)\phi(\rightarrow K^+K^-)$  analysis.

The CMS solenoid magnet, being the biggest solenoid magnet ever built, is a distinctive design feature and engineering challenge (See Fig. 2.8 for an artistic view and [20, 22] for more details). In contrast to previous detector magnets it uses 4 layers of winding to reach the maximum field of 4 T. Although it is large, with a diameter of 6 m and a length of 12.5 m, it is relatively thin ( $\Delta R/R \approx 0.1$ ), minimising multiple scattering of traversing. The 220 t cold mass contains the stabilised reinforced NbTi conductor cooled with liquid helium at a temperature of 4.6 K. At maximum current the stored energy is 2.6 GJ. The high ratio between stored energy and cold mass of 11.6 kJ/kg leads to a large mechanical deformation during energising (0.15%).

The flux is returned through a 10'000 t iron yoke which is composed of 11 large elements, 6 endcap disks and 5 barrel wheels, with a weight from 400 t to 1920 t for the central wheel including coil and cryostat. It is saturated at 1.8 T. The different elements can be moved apart on air cushions.

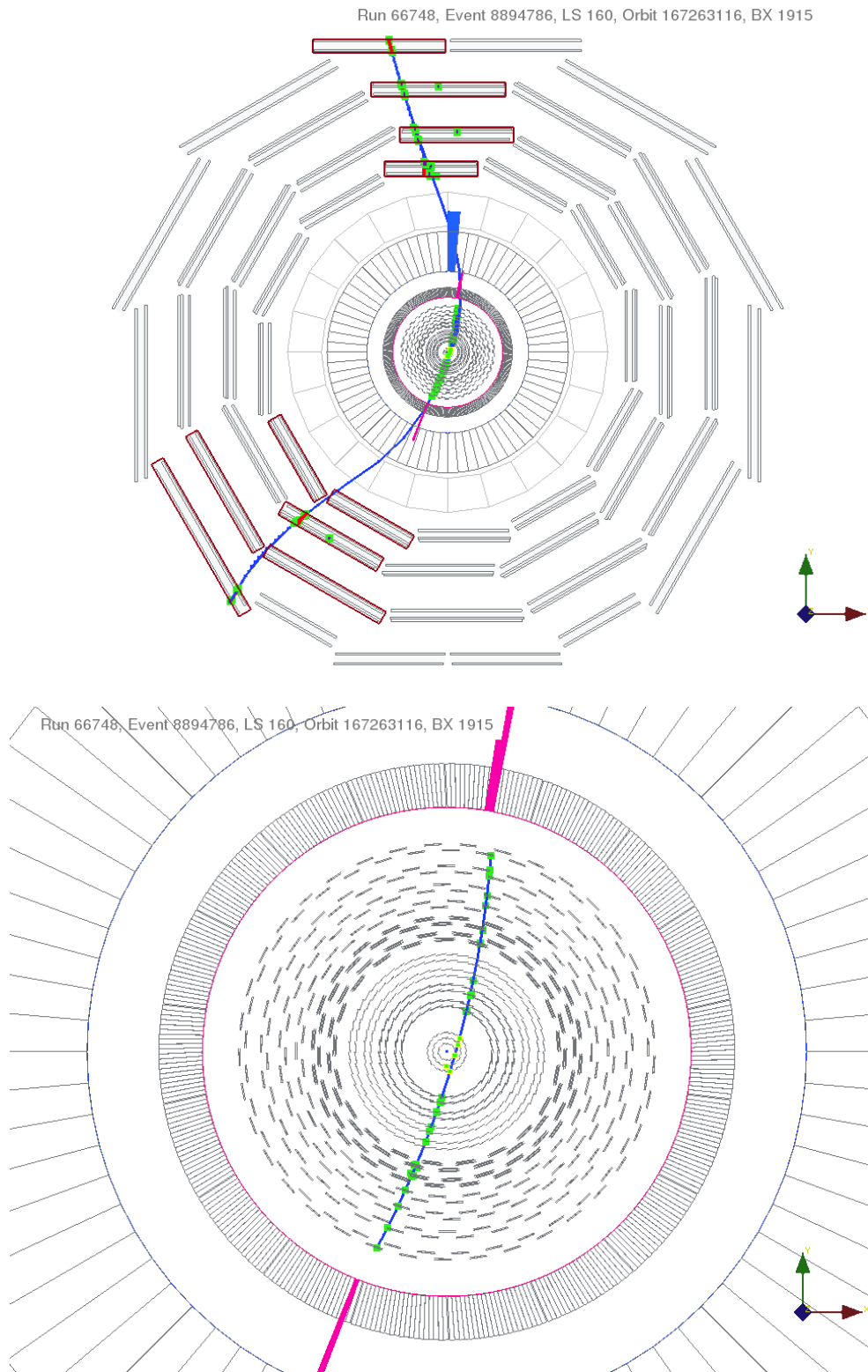


**Figure 2.7:** A cosmic muon traversing the CMS detector (top), with hits in the muon chambers and in the tracker indicated in green and energy deposits in the calorimeter in pink (electromagnetic) and blue (hadronic). The magnetic field in the center is 3.8 T. The lower plot shows a close-up of the tracker for the same event.



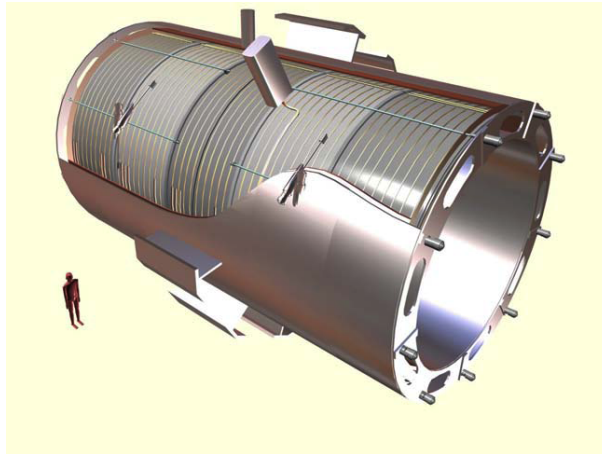


**Figure 2.8:** General artistic view of the 5 modules composing the cold mass inside the cryostat, with details of the supporting system (vertical, radial and longitudinal tie rods) [20].

### 2.2.2 Inner tracking system

The aim of the inner tracking system is an efficient measurement of trajectories of charged particles emerging from LHC collisions, as well as a precise measurement of secondary vertices of long-lived particles such as  $b$ -hadrons and  $\tau$ -leptons. At LHC design luminosity ( $\mathcal{L} = 10^{34} \text{ cm}^{-2}\text{s}^{-1}$ ), an average of about 1000 particles will emerge from more than 20 overlapping proton-proton collisions per bunch crossing (i.e. every 25 ns). Thus high granularity and fast response are needed to keep the detector occupancy as low as 1%. This leads to a high power density of detector electronics, making an efficient cooling imperative. Moreover, the detector will suffer from severe radiation damage due to the harsh environment. At a distance of 4 cm from the collision point a charged particle flux of up to 100 MHz/cm<sup>2</sup> is expected. To be able to use the inner tracking system for 10 years (with the exception of the first 3 layers, which will have to be replaced after 2-3 years), it was decided to use silicon technology for the full inner tracking system. This resulted in the biggest silicon tracker ever.

The layout of the inner tracking system is illustrated in Fig. 2.9. The total tracking system provides a coverage up to  $|\eta| = 2.5$ . In total, 200 m<sup>2</sup> of active silicon are used. An homogeneous magnetic field of 3.8 T over the whole tracker volume is provided by the solenoid.

To keep the occupancy below 1%, pixel detectors have to be used up to a radius of 10 cm, whereas in the outer regions strip detectors can be used. In the following a description of the two different components of the inner tracking system will be given, where particular emphasis is laid on the silicon pixel detector to which the Univer-

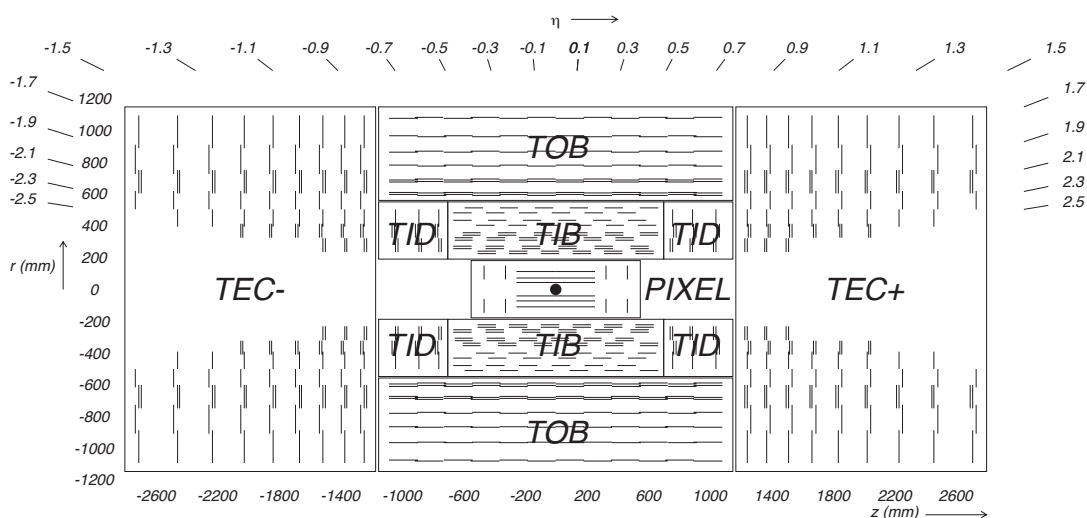


**Figure 2.9:** Schematic cross section through the CMS tracker. Each line represents a detector module. Double lines indicate back-to-back modules which deliver stereo hits. The innermost detector consists of the barrel and forward pixel detector. The intermediate region holds the Tracker Inner Barrel and Disks (TIB/TID). The outer parts are the Tracker Outer Barrel (TOB) surrounding the TIB and TID and the Tracker EndCaps (TEC) [20].

sity of Zürich contributed. The pixel Lorentz drift measurement is then presented in Chapter 3.

### 2.2.2.1 Silicon pixel detector

The silicon pixel detector with a pixel size of  $100 \times 150 \mu\text{m}^2$  in  $r - \phi$  and  $z$  direction, allows a 3D vertex reconstruction. The precise tracking points yield a small impact parameter resolution (starting from  $100 \mu\text{m}$  for  $1 \text{ GeV}/c$  decreasing to less than  $10 \mu\text{m}$  for momenta above  $100 \text{ GeV}/c$  [23]) and thus a good secondary vertex reconstruction for a pseudorapidity up to  $|\eta| = 2.5$ , matching the silicon strip detector acceptance.

The 59 cm long barrel consists of 3 cylindrical layers at radii of 4.4 cm, 7.3 cm and 10.2 cm, each divided into two half-cylinders. A half-cylinder contains ladders and half-ladders that provide the support structure and cooling for the pixel modules. The half-ladders, which are positioned at the edges of the half-cylinders, overlap to ensure full hermetic coverage. Each ladder (half-ladder) contains eight modules (eight half-modules) as illustrated in Fig. 2.10, adding up to a total of 672 full-modules and 96 half-modules, or a total of 48 million pixels.

The layout of a module is shown in Fig. 2.11. Two (one for half-modules) silicon nitride basestrips are used to fix the module on the support structure. The sensors

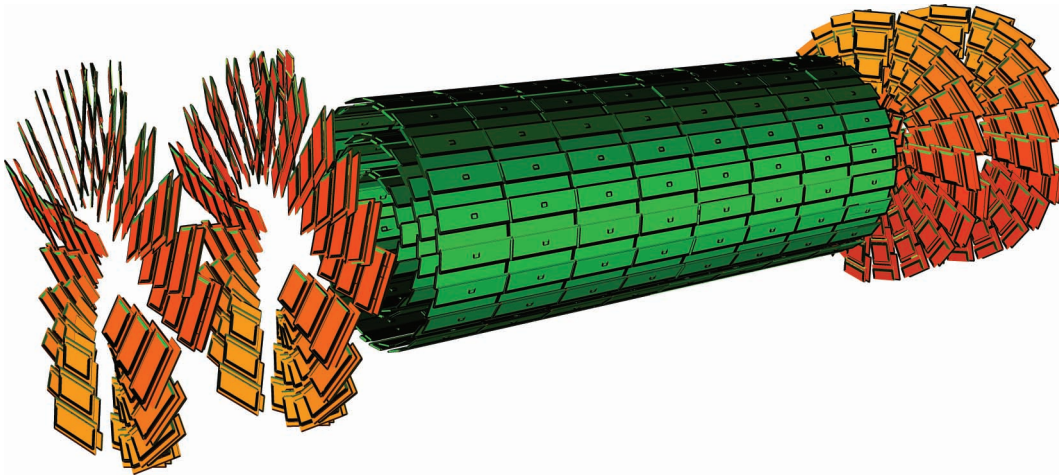


**Figure 2.10:** Sketch of the CMS forward and barrel pixel detectors. The barrel pixel detector consists of three central layers whereas the forward pixel detector consists of two disks on each side .

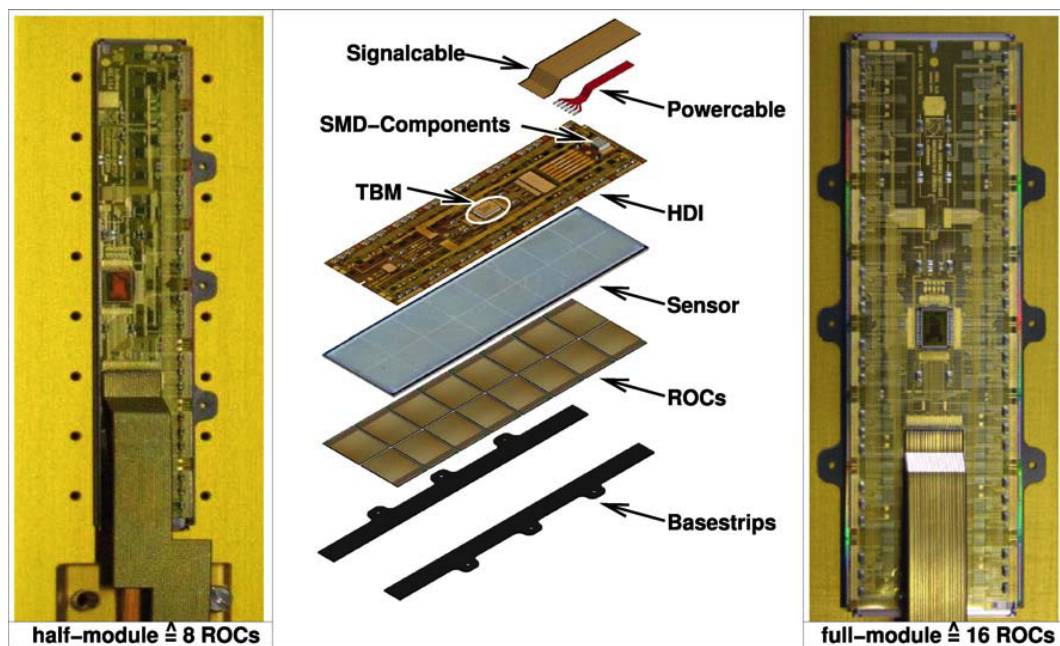


**Figure 2.11:** Exploded view (middle panel) of a barrel pixel detector full module (right panel) and picture of an assembled half module (left panel) [20].

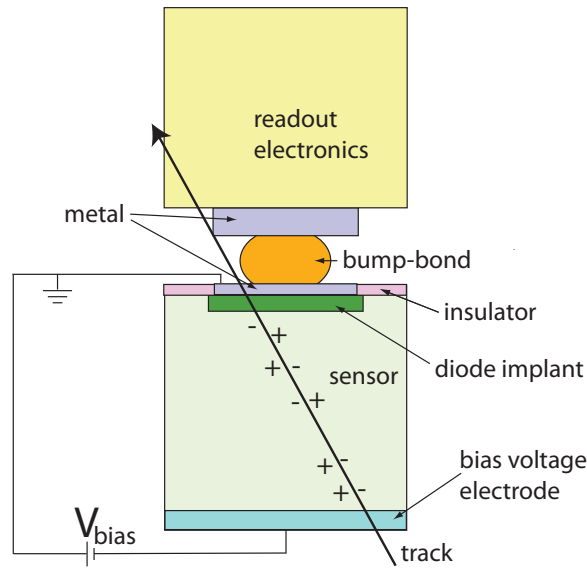


**Figure 2.12:** *Sketch of the cross section of a hybrid pixel sensor.*

consist of high dose n-implants introduced into a high resistance n-substrate. A rectifying pn-junction is placed on the back side of the sensor surrounded by a multiguard ring structure, allowing to keep all sensor edges at ground potential. The sensor thickness is  $285\ \mu\text{m}$ . The double side processing leads to higher costs, but provides a high signal charge at moderate bias voltages ( $< 600\ \text{V}$ ) even when the detector is irradiated by high hadron fluences. For each module (half-module) 16 (8) readout chips (ROC) are connected with the sensors through the bump bonding technique (See Fig. 2.12). The High Density Interconnect (HDI) distributes power and control signals to the chip and transmits the readout from the double column periphery of the ROCs to the Token Bit Manager (TBM). The TBM itself is a chip that controls readout and programming of each module. Wire bonds are used to connect the ROC and the HDI as well as the HDI and TBM. A two layer kapton/copper compound cable with 21 traces transmits the readout and control signal. Since TBM and ROCs are both produced in radiation hard  $0.25\ \mu\text{m}$  CMOS technology, the lifetime of the module is limited only by radiation damage to the sensor.

The magnetic field in the barrel pixel detector is perpendicular to the drift direction, leading to Lorentz drift spreading the charge of the collected signal charge over more than one pixel. Using a zero-suppressed readout scheme with analogue pulse height readout, charge sharing allows to achieve a spatial resolution in the range of  $15 - 20\ \mu\text{m}$ .

The forward pixel detector consists of 2 endcap disks on each side located at  $\pm 34.5\ \text{cm}$  and  $\pm 46.5\ \text{cm}$  from the interaction point along the beam direction. The disks have inner and outer radii of approximately  $6\ \text{cm}$  and  $15\ \text{cm}$  and are subdivided into half disks, each including 12 trapezoidal blades (Fig. 2.13). These are arranged in a





**Figure 2.13:** *The FPix half-disk cooling channels mounted in the outer half-ring structure. The turbine-like geometry is apparent. Panels are mounted on both sides of the cooling channels [20].*

turbine-like geometry to enhance charge sharing due to Lorentz drift in the magnetic field. The sensors are slightly thinner than the barrel sensors with a thickness of  $270\ \mu\text{m}$ . Each blade is a sandwich of two back-to-back modules around a U-shaped cooling channel with rectangular front and back sensors overlapping to provide full coverage. There are 672 sensors of five different sizes in the forward pixel detector resulting in about 18 million pixel cells.

The properties of both, the barrel and forward pixel detectors are summarised in Tab. 2.1.

**Table 2.1:** *Properties of the CMS pixel detector [20].*

	barrel	forward
active area	$1\ \text{m}^2$	
pixels	66'000'000	
layer	3	2
thickness	$285\ \mu\text{m}$	$270\ \mu\text{m}$
pixel size	$100\ \mu\text{m} \times 150\ \mu\text{m}$	
extention in $z$	$-29.5\ \text{cm} < z < 29.5\ \text{cm}$	$34.5\ \text{cm} <  z  < 46.5\ \text{cm}$
extention in $r$	$4\ \text{cm} < r < 10.2\ \text{cm}$	$6\ \text{cm} < r < 15\ \text{cm}$
$\sigma$	$15\ \mu\text{m} \times 20\ \mu\text{m}$	$15\ \mu\text{m} \times 15\ \mu\text{m}$

### 2.2.2.2 Silicon strip detector

The silicon strip detector with a total length of 5.8 m and an outer diameter of 2.5 m is composed of three different subsystems (Fig. 2.9). It has a total active area of 198 m<sup>2</sup> with 9.3 million strips. The tracker inner barrel and disks (TIB and TID) are made of 320  $\mu\text{m}$  thick silicon micro-strip sensors. The TIB consists of four concentric cylinders at radii of 25.5 cm, 33.9 cm, 41.85 cm and 49.8 cm extending from  $-70$  cm to  $70$  cm along the  $z$ -axis. The inner two layers have a strip pitch of 80  $\mu\text{m}$  whereas the outer two have 120  $\mu\text{m}$ , yielding a resolution in  $r - \phi$  of 23  $\mu\text{m}$  and 35  $\mu\text{m}$ , respectively (all resolutions given in RMS). The TID consists of three identical disks on each side with an inner and outer radius of approximately 20 cm and 50 cm, placed in  $z$  between  $\pm 80$  cm and  $\pm 90$  cm. Each disk is made up of three rings with varying strip pitch between 100 – 141  $\mu\text{m}$ .

The TIB and TID are surrounded by the tracker outer barrel (TOB) which consists of one single mechanical structure supporting 668 self-contained sub-assemblies called rods. Extending in  $z$  between  $-118$  cm and  $+118$  cm it consists of 6 barrel layers at radii of 60.8 cm, 69.2 cm, 78.0 cm, 86.6 cm, 96.5 cm and 108.0 cm. The TOB layers are made of 500  $\mu\text{m}$  thick micro-strip sensors with a pitch of 183  $\mu\text{m}$  for the inner four layers and 122  $\mu\text{m}$  for the outer two layers, providing a resolution in  $r - \phi$  of 53  $\mu\text{m}$  and 35  $\mu\text{m}$ , respectively.

The tracker endcaps (TEC) reside at  $z$ -positions between  $\pm 124$  cm and  $\pm 282$  cm, with a radial coverage between 22.5 cm and 113.5 cm. They consist of nine disks made up of up to seven rings of silicon micro-strip detectors, with a thickness of 320  $\mu\text{m}$  for the inner four rings and 500  $\mu\text{m}$  for the outer three. The radial strips have pitches between 97  $\mu\text{m}$  and 184  $\mu\text{m}$ .

In order to provide a measurement of the second coordinate ( $z$  for the barrel and  $r$  for the disks), modules with a stereo angle of 100 mrad are mounted on some of the modules. As shown in Fig. 2.9, this is the case for the first two layers of the TIB and TOB, the first two rings of the TID and the first two and fifth ring of the TEC yielding a  $z$  resolution of 230/530  $\mu\text{m}$  for the TIB/TOB, and a resolution depending on the strip pitch for the TID/TEC. This tracker layout ensures at least nine hits in the silicon strip tracker with at least four of them being 2-dimensional for pseudorapidities up to  $|\eta| = 2.4$ . The tracker acceptance ends at  $|\eta| = 2.5$  (Fig. 2.9).

The properties of the silicon strip detectors are summarised in Tab. 2.2.

Fig. 2.14 shows the material thickness of the CMS tracker (including pixel detector) in units of radiation lengths, which is kept as small as possible to reduce multiple scattering. It increases from  $0.4 X_0$  at  $\eta \approx 0$  to almost  $2 X_0$  at  $|\eta| \approx 1.4$ , decreasing again to about  $1 X_0$  at  $|\eta| = 2.5$ .

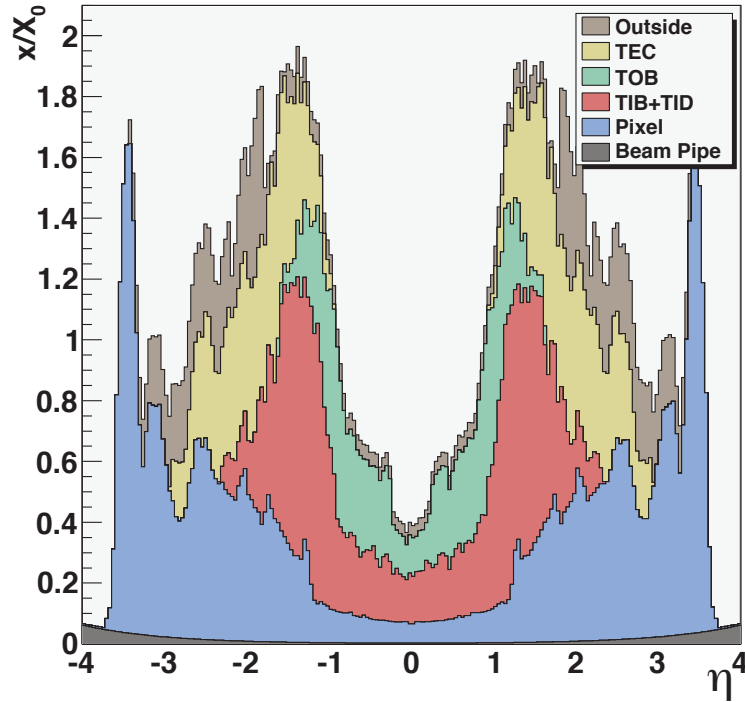


**Figure 2.14:** Total integrated material budget of the CMS tracker in terms of radiation length  $x/X_0$  as a function of pseudorapidity. The contributions of various subdetectors are stacked [24].

silicon strip tracker	outer	inner
active area	198 m <sup>2</sup>	
channels	9'300'000	
barrel	TIB	TOB
layers	4	6
stereo layer	1,2	1,2
thickness	320 μm	500 μm
$r - \phi$ pitch	80 μm(1,2) / 120 μm(3,4)	183 μm(1-4) / 122 μm(5,6)
$\sigma(r - \phi)$	23 μm / 35 μm	53 μm / 35 μm
$\sigma(z)$	230 μm	530 μm
forward	TID	TEC
disks	3	9
rings	3	up to 7
stereo rings	disk 1,2	1,2,5
thickness	320 μm	320 μm(1-4) / 500 μm(5-7)
$r - \phi$ pitch	100 – 141 μm	97 – 184 μm

**Table 2.2:** Properties of the CMS silicon strip detectors [20].

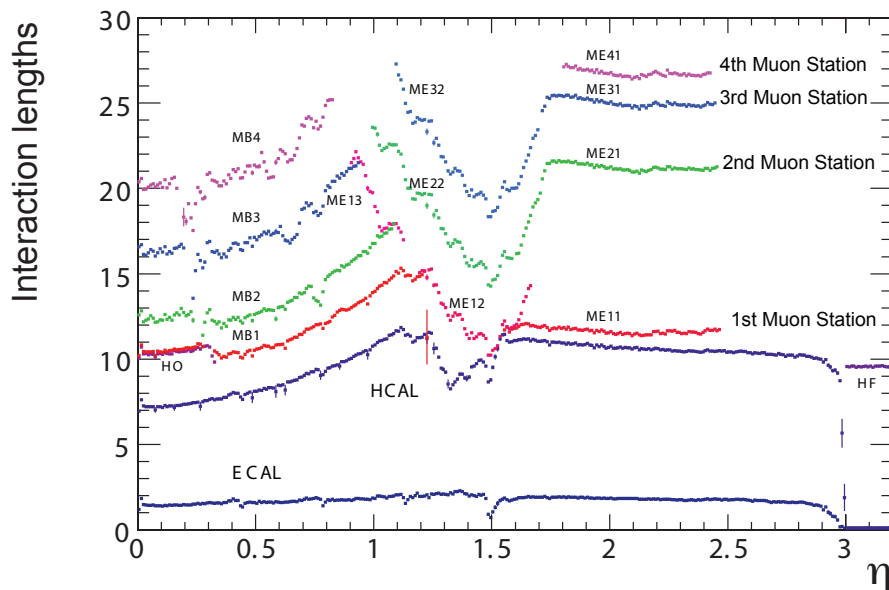


**Figure 2.15:** Material thickness in interaction lengths after the ECAL, HCAL, and at the depth of each muon station as a function of pseudorapidity [20].

### 2.2.3 The CMS muon system

As implied by the experiment's name, the identification and momentum measurement of muons is of central importance to CMS. Muons can be distinguished from hadrons thanks to the large amount of material before the muon system (Fig. 2.15) which absorbs all hadrons. Muon identification is of fundamental importance for several physics processes such as the  $H \rightarrow 4\mu$  channel and the decay  $B_s \rightarrow J/\psi(\rightarrow \mu^+\mu^-)\phi(\rightarrow K^+K^-)$  which is the subject of this thesis. A muon system with good muon momentum resolution, good trigger capability and wide angular coverage is needed. In addition, the system should be robust and inexpensive because of the large area to be covered (the muon system consists of about 25'000 m<sup>2</sup> of detection planes).

Due to the shape of the solenoid magnet, the muon system was naturally driven to have a cylindrical barrel section and 2 planar endcap regions. Three different types of gaseous detectors were chosen: drift tubes (DT) to measure momentum in the barrel region and cathode strip chambers (CSC) in the endcap disks to cope with the higher fluxes in the forward hemispheres [20]. Resistive plate chambers (RPC) are also installed in the barrel and endcap region to provide a fast and independent trigger to complement the self-triggering capabilities of the DTs and CSCs. The regions covered by the three detector types are shown in Fig. 2.16.

The DTs cover a pseudorapidity region up to  $|\eta| = 1.2$  and are divided into four stations embedded in the layers of the flux return yoke. Each of the first three stations (MB1, MB2, MB3) contain eight chambers, in two groups of four, which measure the

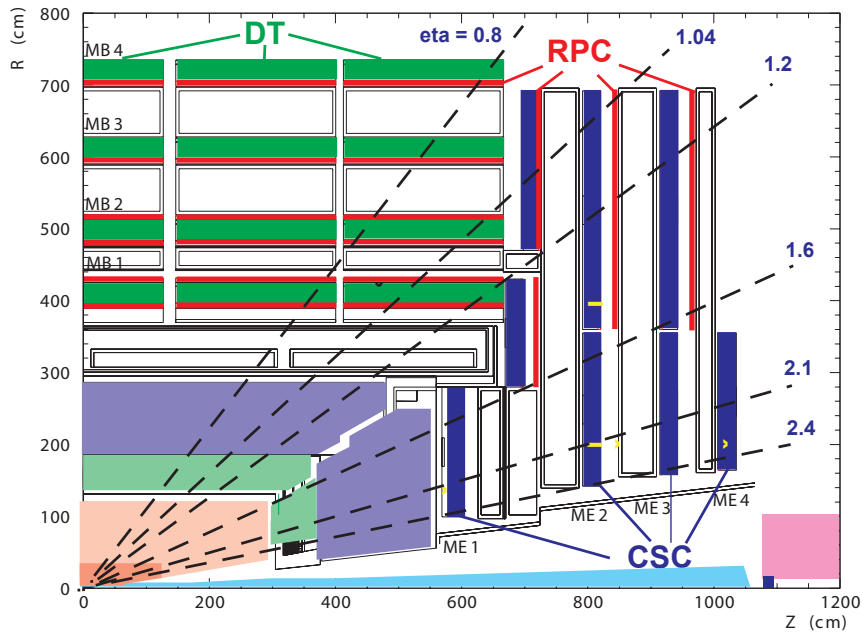


**Figure 2.16:** Schematic  $r - z$  view of the muon system. Drift tubes (DT) are shown in green, resistive plate chambers (RPC) in red and cathode strip chambers in blue.

muon coordinate in the  $r - \phi$  bending plane, and four chambers which provide a measurement in the  $z$  direction. The fourth station (MB4) does not contain any  $z$  planes. The two sets of four chambers in each station are separated as much as possible to achieve the best angular resolution. See also Fig. 2.17 for the positioning in the return yoke.

Four CSC stations (six layers each) are installed in the endcap region with chambers positioned in the return yoke perpendicular to the beam line, providing a coverage in pseudorapidity of  $0.9 < |\eta| < 2.4$ . The cathode strips of each chamber run radially outwards and provide a precision measurement in the  $r - \phi$  plane. The anode wires run approximately perpendicular to the strips providing a measurement of  $\eta$ . The CSCs provides robust pattern recognition for rejection of non-muon backgrounds and efficient matching of hits to those in other stations and to the CMS inner tracker.

The RPCs are double-gap chambers, operated in avalanche mode to ensure good operation at high rates. They produce a fast response, with good time resolution but coarser position resolution than the DTs or CSCs. The exact position of the RPCs can be seen in Fig. 2.16. The RPCs provide a fast, independent, and highly-segmented trigger with a sharp  $p_T$  threshold over a large range in rapidity ( $|\eta| < 1.6$ ).

The muon transverse-momentum resolution for the muon system alone, the tracker alone and for the combination of both is illustrated in Fig. 2.18. For lower momentum multiple scattering dominates the resolution in the muon chamber and the silicon tracker gives the best momentum estimate. At high momentum where multiple scat-

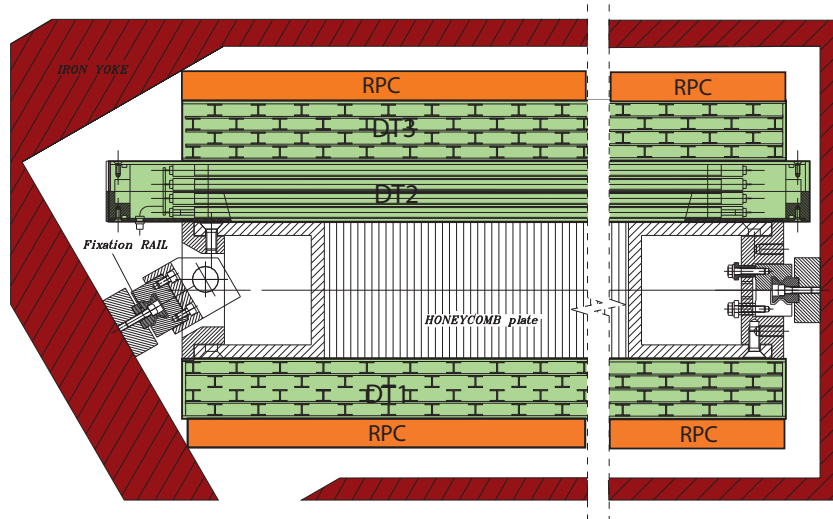


**Figure 2.17:** Drawing of a DT chamber (green) inside the iron yoke ( $r - \phi$  projection). One can see the 2 super-layers with wires along the beam direction (DT1 and DT3) and the other super-layer perpendicular to it (DT2). In between is a honeycomb plate with supports attached to the iron yoke. The RPCs (orange) are glued to the bottom and/or top faces of the DT chambers, depending on chamber type [20].

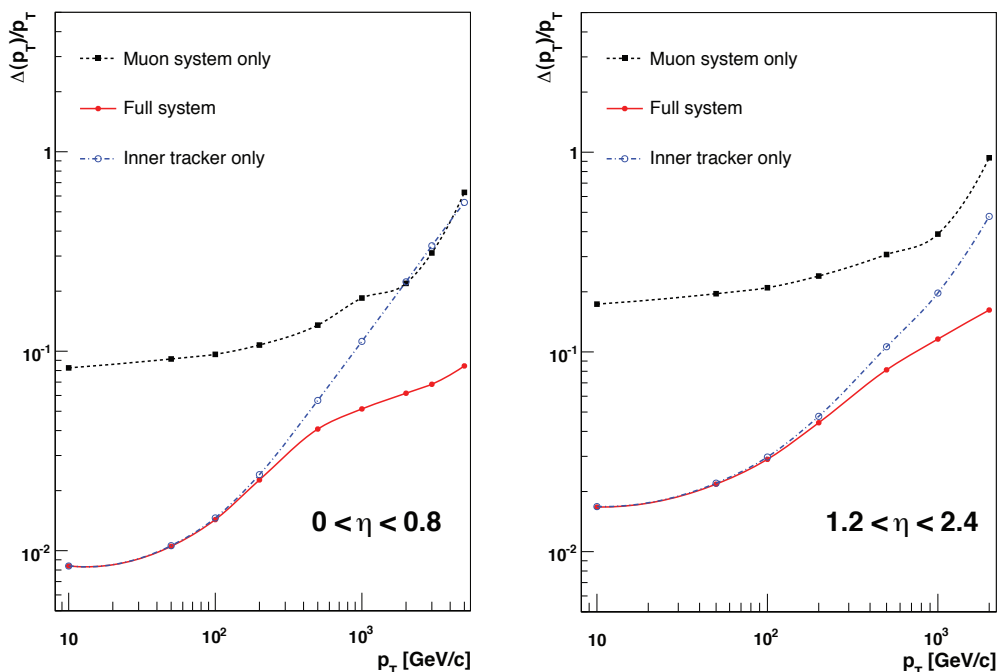


**Figure 2.18:** Muon transverse-momentum resolution as a function of transverse-momentum for the muon system only, the inner tracking only, and both. Left panel:  $|\eta| < 0.8$ , right panel:  $1.2 < |\eta| < 2.4$  [20].

tering and energy loss are negligible the muon trajectory in the muon chambers can be extrapolated back to the collision region. thus improving the muon transverse-momentum resolution.

## 2.2.4 Trigger and data acquisition

At the LHC, proton-proton beam crossings will occur at a rate of 40 MHz with several overlapping events each crossing (about 20 for the design luminosity of  $\mathcal{L} = 10^{34} \text{ cm}^{-2}\text{s}^{-1}$ ). Thus a reduction to a much lower number of events is necessary. CMS uses a two-stage trigger system. The Level-1 trigger consists of custom-designed, programmable electronics. The design output rate of this system is 100 kHz. The Level-1 trigger is organised in three steps. *Local triggers* use energy deposits in the calorimeter and track segments or hit patterns in the muon chambers. This information is combined by the *regional trigger* to build trigger objects such as electrons and muons. The *global trigger* finally takes a decision based on these objects. Since decision time is  $3.2 \mu\text{s}$ , the high resolution data is held in pipelined memories in the front-end electronics in the meantime. It is important to note that no inner tracking system information is used at the Level-1 trigger stage.

The high-level trigger (HLT) can access the full readout data and uses software implemented algorithms in the CMS software framework running on a PC-farm to reduce the event-rate to about 100 Hz. The trigger used for the  $B_s \rightarrow J/\psi(\rightarrow \mu^+\mu^-)\phi(\rightarrow K^+K^-)$  analysis will be described in Chapter 4.

An event was selected by the trigger system has to pass through the Data Acquisition (DAQ) chain before being stored, transferred and reconstructed by the CMS offline computing system. The data and the simulated samples are distributed over the Worldwide LHC Computing Grid (WLCG) [25] and can be processed in various computer centres with hierarchical architecture (Tiers) [26].





# Chapter 3

## Measurement of the Lorentz angle

### 3.1 Introduction

The CMS pixel detector [27] (see Chapter 2), is located inside a 3.8 T superconducting solenoid. Electron-hole pairs produced by charged particles traversing the pixel sensors will thus experience the Lorentz force and drift under the combined magnetic and electric forces (see Fig. 3.1). The charge deposit is therefore collected by several adjoint pixels. Charge sharing can be used to improve the spatial resolution. This is of course possible due to the analog readout and a noise level much lower than the signal.

During LHC operation, radiation damage will reduce the performance of the silicon sensors. The increasing number of defects in the silicon crystals affects the Lorentz angle in several ways [27]. Trapping of charge carriers leads to a reduction of the collected charge which has to be compensated by a higher bias voltage [28], leading to a reduced Lorentz deflection [29]. The spatial resolution of the pixel detector depends, among other factors, on the knowledge of the Lorentz deflection, since the reconstructed hit positions need to be corrected accordingly. Test beam studies have shown that the Lorentz angle at 4 T varies from  $23^\circ$  for an unirradiated sensor to  $8^\circ$  for a highly irradiated sensor due to the required increase of the bias voltage from 150 V to 600 V. Decreasing the temperature from  $10^\circ$  to  $-20^\circ$  can slightly increase the Lorentz drift again (see Fig. 3.2(a), [29]). Furthermore, the initially uniform electric field across the sensor bulk changes after irradiation and the linear correlation between drift length and depth in the sensor bulk is no longer valid (see Fig. 3.2(b), [30]).

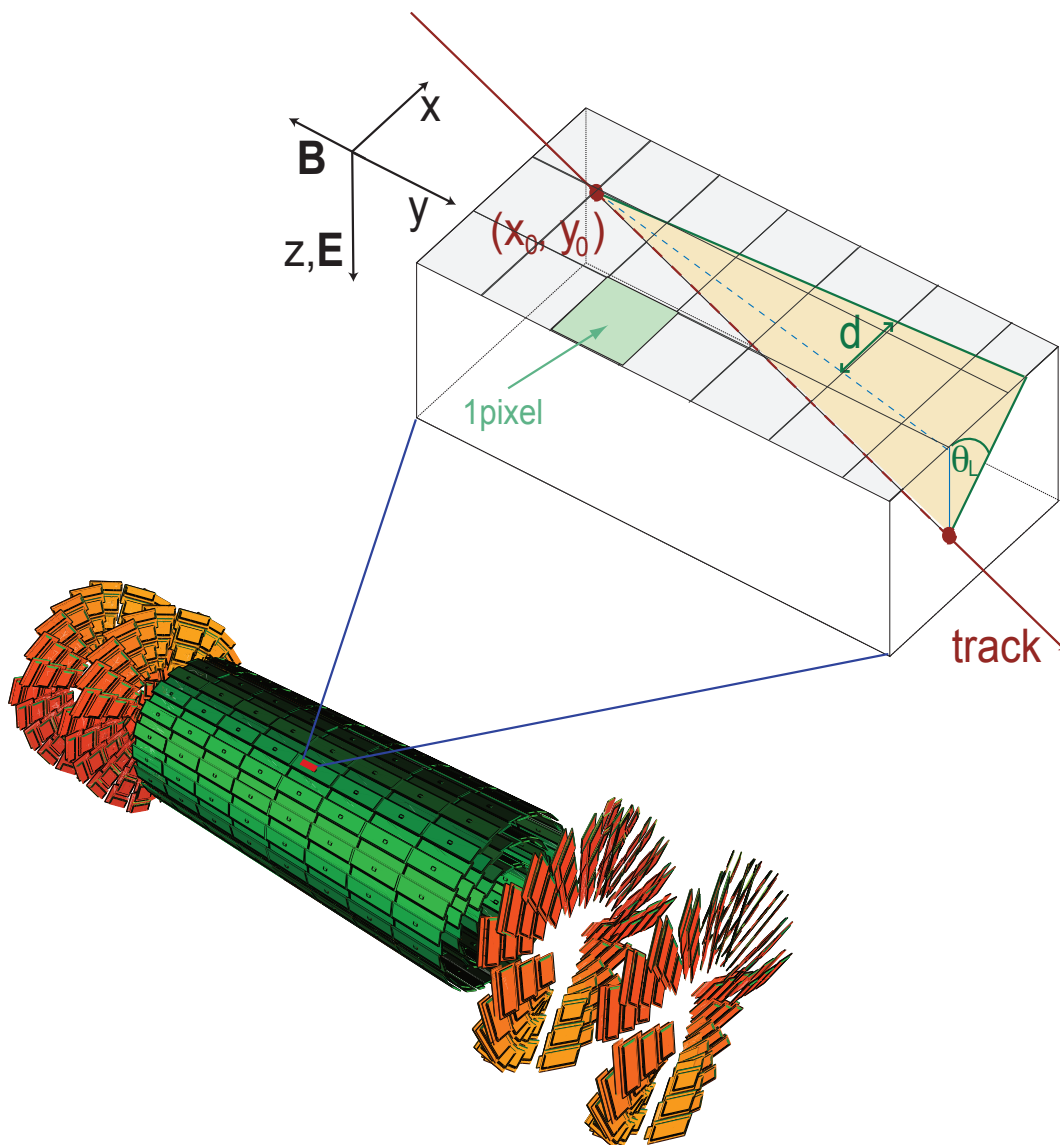


**Figure 3.1:** Sketch of a track passing through the barrel pixel sensor. The plane in which the charge carriers drift is shaded. The Lorentz angle is labelled as  $\theta_L$ .

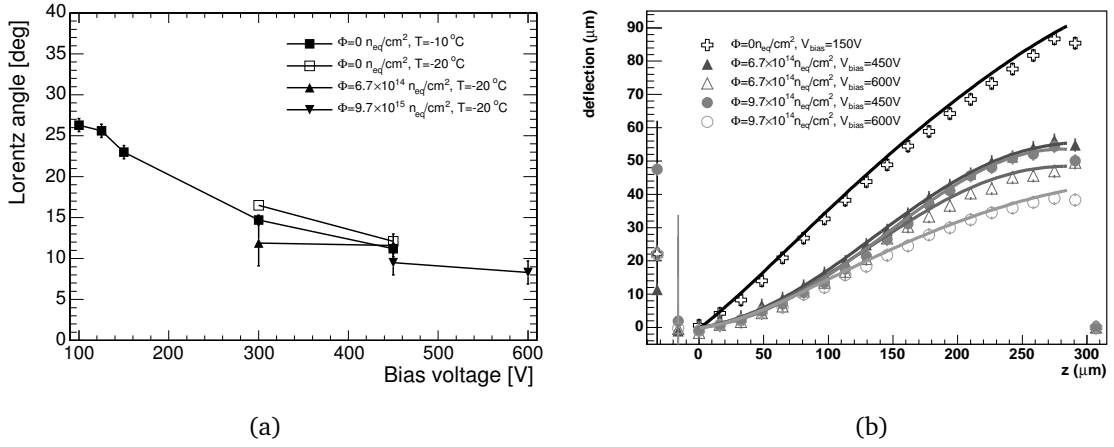


**Figure 3.2:** (a) Lorentz angle measured with sensors irradiated to different fluences as function of the bias voltage [29]. (b) Charge carriers deflection (drift length) measured as a function of depth in the silicon bulk (markers) compared to a simulation (solid lines) for different bias voltages and irradiation fluences. [30].

The charge carriers in the conduction band of a Silicon crystal move as quasi-free particles according to the following equation of motion [31],

$$m^* \cdot \frac{d\mathbf{v}}{dt} = q \cdot \mathbf{E} + q \cdot r_H \cdot (\mathbf{v} \times \mathbf{B}) - \frac{|q|}{\mu(E)} \cdot \mathbf{v}, \quad (3.1)$$

where  $m^*$  is the effective electron mass ( $\approx 0.25m_e$ ),  $q$  is the charge carriers charge ( $q = \pm e$ ),  $r_H$  is the Hall factor (close to 1) and  $\mu(E)$  is the mobility function that describes the damping caused by phonon interactions. Since the drift time is much smaller than the damping time  $m^*\mu(E)/q$ , the velocity can be assumed to be uniform [31]. For general electric and magnetic fields the solution is

$$\mathbf{v} = \frac{\mu \cdot (q \cdot \mathbf{E} + |q| \cdot \mu \cdot r_H \cdot (\mathbf{E} \times \mathbf{B}) + q \cdot \mu^2 \cdot r_H^2 \cdot (\mathbf{E} \cdot \mathbf{B}) \cdot \mathbf{B})}{|q| \cdot (1 + \mu^2 \cdot r_H^2 \cdot |\mathbf{B}|^2)}. \quad (3.2)$$

In the case of drifting electrons ( $q = -e$ ), an electric field in the  $z$  direction ( $\mathbf{E} = E \cdot \mathbf{e}_z$ ), and a general magnetic field ( $\mathbf{B} = B_x \cdot \mathbf{e}_x + B_y \cdot \mathbf{e}_y + B_z \cdot \mathbf{e}_z$ ) the velocity can be expressed in component form as

$$\begin{aligned} v_x &= -\frac{\mu \cdot E}{1 + \mu^2 \cdot r_H^2 \cdot |\mathbf{B}|^2} \cdot (\mu \cdot r_H \cdot B_y + \mu^2 \cdot r_H^2 \cdot B_z \cdot B_x) \\ v_y &= \frac{\mu \cdot E}{1 + \mu^2 \cdot r_H^2 \cdot |\mathbf{B}|^2} \cdot (\mu \cdot r_H \cdot B_x - \mu^2 \cdot r_H^2 \cdot B_z \cdot B_y) \\ v_z &= -\frac{\mu \cdot E}{1 + \mu^2 \cdot r_H^2 \cdot |\mathbf{B}|^2} \cdot (1 + \mu^2 \cdot r_H^2 \cdot B_z^2). \end{aligned} \quad (3.3)$$

The Lorentz angle in the  $x$  direction is thus given by

$$\tan \theta_L = \frac{v_x}{v_z} = \frac{\mu \cdot r_H \cdot B_y + \mu^2 \cdot r_H^2 \cdot B_z \cdot B_x}{1 + \mu^2 \cdot r_H^2 \cdot B_z^2}. \quad (3.4)$$

In the barrel pixel detector the magnetic field is anti-parallel to the  $y$  direction ( $\mathbf{B} = -B\mathbf{e}_y$ ), thus the Lorentz angle is of the simple form

$$\tan \theta_L = -\mu \cdot r_H \cdot B. \quad (3.5)$$

For the forward pixel detector the expression becomes more complicated due to the non-zero magnetic field components  $B_y = -B \cdot \sin 20^\circ$  and  $B_z = B \cdot \cos 20^\circ$

$$\tan \theta_L = -\frac{\mu \cdot r_H \cdot B \cdot \sin 20^\circ}{1 + \mu^2 \cdot r_H^2 \cdot B^2 \cdot \cos^2 20^\circ}. \quad (3.6)$$

The mobility function  $\mu(E)$  can be expressed by the following empirical function [32]

$$\mu = \frac{\mu_0}{\left(1 + \left(\frac{E}{E_c}\right)^\beta\right)^{1/\beta}}, \quad (3.7)$$

with  $\mu_0 = v_m/E_c$ , where  $v_m$  is a temperature dependent constant,  $E_c$  is a function of doping and temperature and  $\beta$  a function of temperature [32]. Since the value of  $r_H$  has an uncertainty of about 10% and the value of  $\mu$  highly depends on the knowledge of temperature, irradiation dose and resulting electric field in the sensor, the Lorentz angle  $\theta_L$  or  $\mu \cdot r_H$  need to be measured from data and cannot be calculated with sufficient precision. Assuming the values from [32] for an unirradiated sensor with a uniform electric field the results are  $\mu \cdot r_H = 0.115$  for the barrel pixel detector using a bias voltage of  $V_{\text{bias}} = 100$  V and  $\mu \cdot r_H = 0.0713$  for the forward pixel detector using a bias voltage of  $V_{\text{bias}} = 300$  V, both at a temperature of 293 K. These values lead to Lorentz angles of  $23.6^\circ$  and  $5.0^\circ$  for the barrel and forward pixel sensors, respectively.

## 3.2 Measurement of the Lorentz angle from cosmic ray data

A large data sample of cosmic muons traversing the CMS detector was recorded in autumn 2008. The sample contains about 300 million events triggered by the muon detectors and calorimeters, described in [33]. Approximately 85000 events contained tracks with hits in the pixel detector. This sample is used to determine the Lorentz angle of the fully installed CMS pixel detector for the first time.

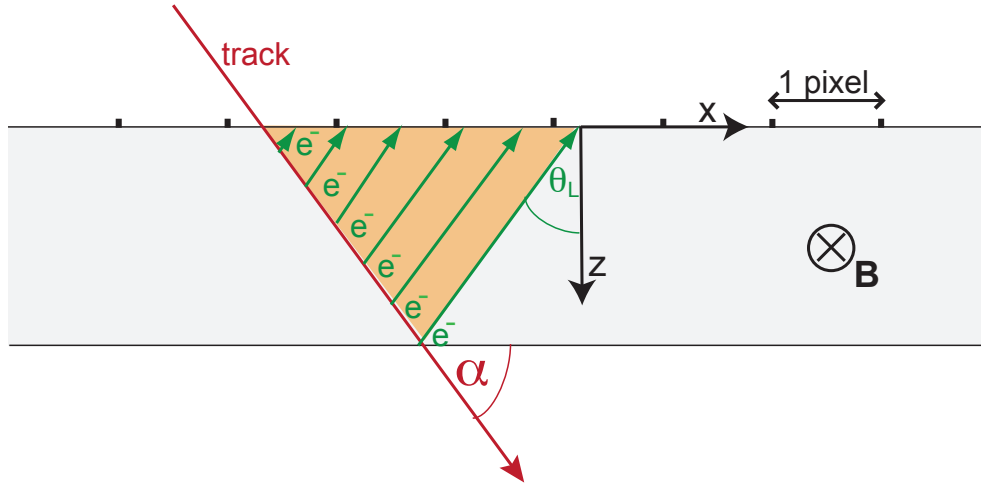


**Figure 3.3:** Sketch showing how charge carriers drift in a barrel silicon pixel sensor. Due to the Lorentz effect they do not drift parallel to the electric field, but are subject to a force which shifts the detection coordinate along the  $x$  direction.

The Lorentz angle is measured from cosmic data using the *minimal-cluster-size* method: Due to the combined electric and magnetic field in the pixel sensor, the electrons drift according to Eq. 3.3. This means, the cluster size in the  $x$  direction is changed with respect to the case without magnetic field, where the electrons would only drift along the  $z$  direction parallel to the electric field. The cluster width in the  $x$  direction is minimal when the track points in or opposite to the drift direction of the charge carriers (i.e. the track is parallel or antiparallel to the green arrows in Fig. 3.3), thus the Lorentz angle can be measured via the following relation:

$$\tan \theta_L = \cot \alpha_{\min} = \frac{v_x}{v_z}, \quad (3.8)$$

with  $\alpha_{\min}$  being the angle for which the cluster size in the  $x$ -direction reaches its minimum.  $\alpha$  is one of the impact angles of the track (Fig. 3.4) defined as the projections of the track,

$$\begin{aligned} \alpha &= \arctan^*(p_z/p_x), \\ \beta &= \arctan^*(p_z/p_y), \\ \gamma &= \arctan^*(p_x/p_y), \end{aligned} \quad (3.9)$$

where  $p_x$ ,  $p_y$ , and  $p_z$  are the momentum components in the local coordinate system of the pixel module and the  $\arctan^*(a/b)$  function determines the arc tangent of  $a/b$ , using the signs of the arguments to determine the quadrant of the return value. The possible values are in the range from  $-180^\circ$  to  $180^\circ$ :

$$\begin{aligned} 0^\circ &< \arctan^*(a/b) \leq 90^\circ && \text{for } a, b \geq 0, \\ 90^\circ &< \arctan^*(a/b) \leq 180^\circ && \text{for } a \geq 0, b < 0, \\ -90^\circ &< \arctan^*(a/b) \leq 0^\circ && \text{for } a < 0, b \geq 0 \\ -180^\circ &< \arctan^*(a/b) \leq -90^\circ && \text{for } a, b < 0. \end{aligned} \quad (3.10)$$

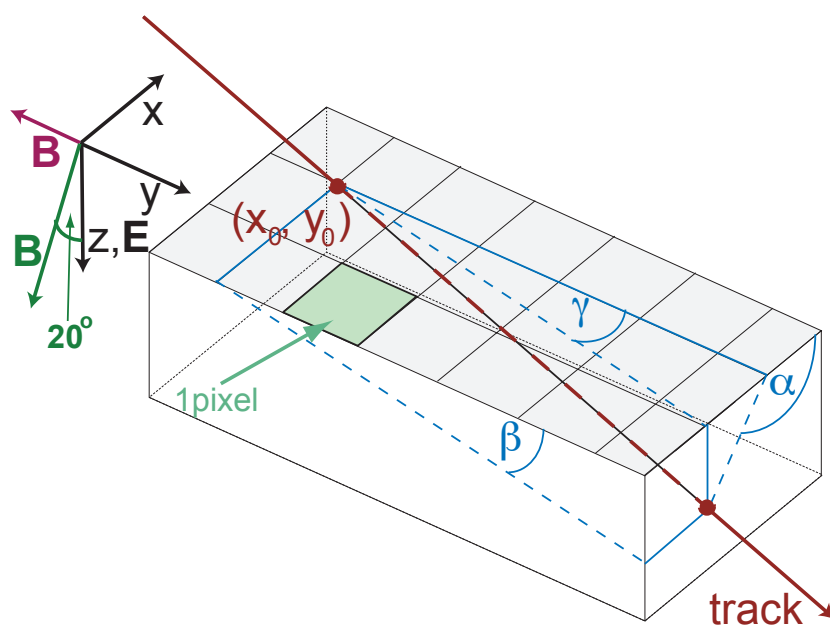


**Figure 3.4:** Sketch showing the local coordinate system in the pixel sensor and the three angles  $\alpha, \beta, \gamma$  defining a track. The magnetic field is indicated for barrel sensors in magenta and for forward sensors in green.

Tracks are reconstructed with the so-called cosmic track finder algorithm [34], using the pixel detector and the silicon strip tracker. The spatial alignment of the pixel detector is detailed in [35]. The precision of the detector position with respect to the particle trajectories after alignment has been derived to be  $3 - 4 \mu\text{m}$  RMS in the barrel and  $14 \mu\text{m}$  in the endcap along both coordinates. In order to assure a correct reconstruction it is required that the reduced  $\chi^2$  per degree of freedom meets  $\chi^2/\text{ndof} < 2$  for tracks (Fig. 3.5). The average ndof is 60 for the barrel pixel detector and 50 for the forward pixel detector.

To avoid dead areas, double size pixels are read out at the edges of each region covered by one ROC. Clusters containing one or more of these large or edge pixels are excluded. In addition, a cluster size along the  $y$  direction of at least two pixels is required for the final Lorentz angle extraction. This requirement was introduced due to problems encountered with clusters containing only one pixel [36]. A cut on the total cluster size however, would bias the result in the cluster size along the  $x$  direction, so it was decided to cut on the perpendicular direction  $y$ .

The distributions of selected hits in  $\alpha$  and  $\beta$  are given in Fig. 3.6 for the barrel and forward pixel detectors. There are no entries in the 2nd and 4th quadrant because both  $\alpha$  and  $\beta$  are always positive if  $p_z > 0$  and negative if  $p_z < 0$ , due to the definition of the angles (Eq. 3.9 and 3.10). The asymmetries around  $90^\circ$  and  $-90^\circ$  in  $\beta$  of these distributions arise from the fact that the majority of muons come through the vertical supply shaft of the CMS detector on one side of the cavern.

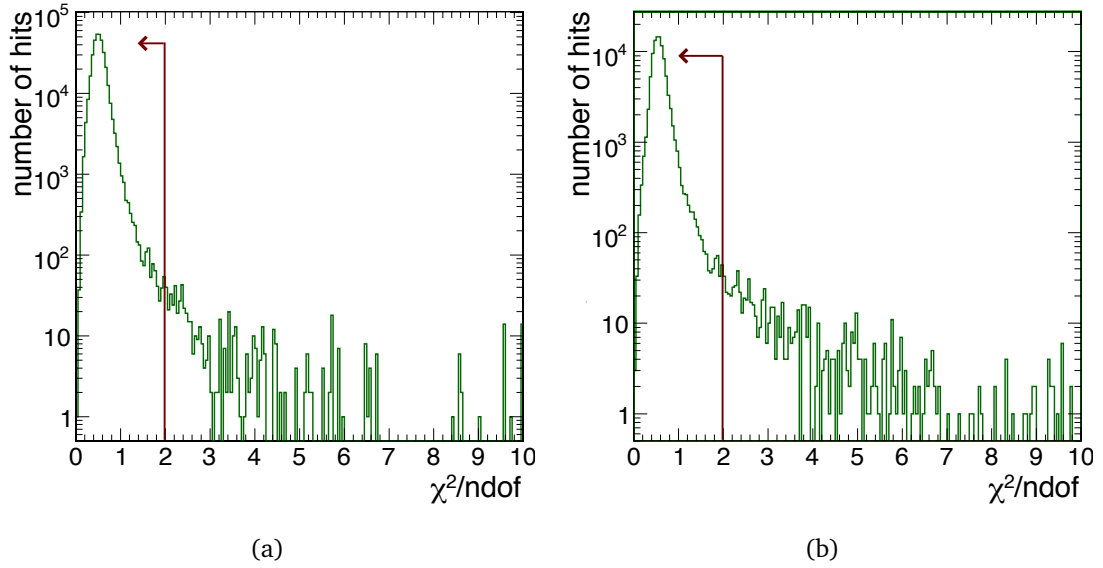


**Figure 3.5:**  $\chi^2/\text{ndof}$  distribution for the track fit. In (a) for the barrel pixel detector and in (b) for the forward pixel detector. To assure a correct reconstruction it is required that  $\chi^2/\text{ndof} < 2$ .

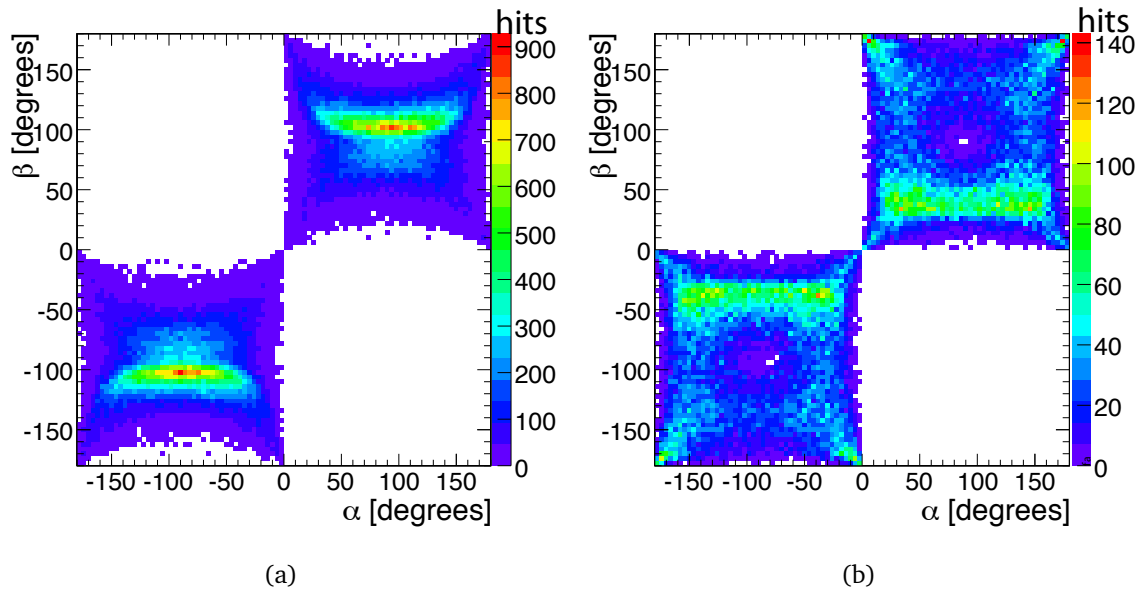


**Figure 3.6:** Frequency histogram of impact angles  $\alpha$  and  $\beta$  (a) for the barrel sensors and (b) for the forward pixel detectors.

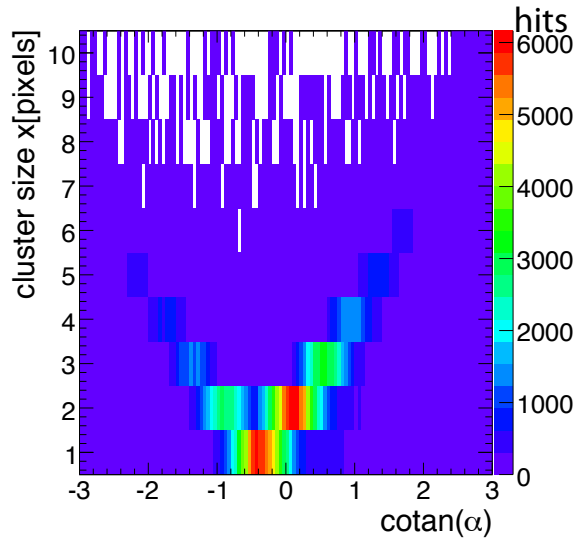


**Figure 3.7:** Distribution of cluster size in  $x$  direction vs. the impact angle  $\alpha$ .

In Fig. 3.7, the distribution of the different cluster-sizes in the  $x$  direction is plotted versus the incident angle  $\alpha$  for the barrel pixel detector. The correlation of the cluster size with  $\alpha$  can clearly be seen. The accumulation of events around  $\cot \alpha$  is due to tracks which are parallel or antiparallel to the drift direction and lead to dominantly clusters of size 1. The average cluster-size for each bin in  $\cot(\alpha)$  is plotted in Fig. 3.8. The minimum is extracted by fitting the following function to the data:

$$f(\cot(\alpha)) = \begin{cases} A + \sqrt{C_{\text{RMS}}^2 + L_{\text{slope}}^2 \cdot (\cot \alpha - \cot \alpha_{\text{min}})^2} & \text{for } \cot \alpha < \cot \alpha_{\text{min}} \\ A + \sqrt{C_{\text{RMS}}^2 + R_{\text{slope}}^2 \cdot (\cot \alpha - \cot \alpha_{\text{min}})^2} & \text{for } \cot \alpha \geq \cot \alpha_{\text{min}} \end{cases} \quad (3.11)$$

where  $\cot \alpha_{\text{min}}$  is the position in  $\cot \alpha$  of the minimal cluster size,  $A$  is the minimum in cluster size,  $L_{\text{slope}}$  and  $R_{\text{slope}}$  are the slopes of the left and right part of the function, respectively.  $C_{\text{RMS}}$  is a measure of the broadening of the minimum, which should, in case of perfect resolution, be zero.

The results of the fit are shown in Tab. 3.1. Although the left and right hand slope of the fit function should have the same value, this is not the case for the barrel pixel detector at 3.8 T. This effect was investigated using PIXELAV [37, 38], a detailed simulation of the pixel sensors. From these studies, I conclude that the effect arises from the charge readout threshold of  $(5200 \pm 1500)$  electrons which might lead to the exclusion of pixels at the edges of the cluster that are below this threshold. Because the electrons do not drift parallel to the electric field, this effect is asymmetric, leading to the different slopes on the left and right side.

The different values for the barrel and forward pixel detectors at 3.8 T are due to the different orientations of the sensors towards the magnetic fields, as described in



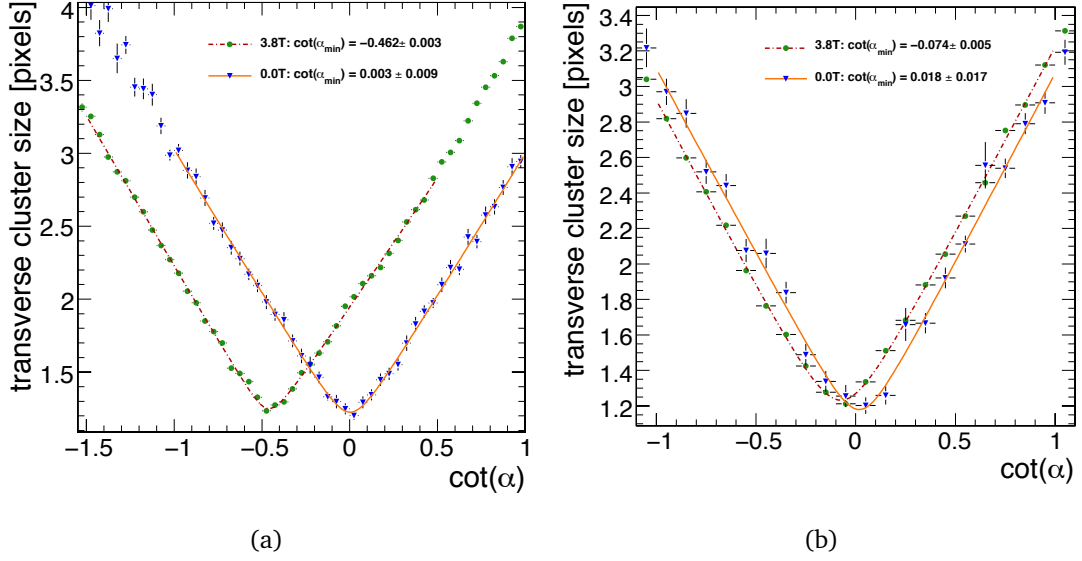


**Figure 3.8:** Average cluster size along the local  $x$  direction as a function of impact angle  $\alpha$  measured in the barrel (a) and forward (b) pixel detector. Circles correspond to the measurement with 3.8 T while triangles correspond to the measurement without magnetic field. Dashed lines show the fit to the data points.

Section 3.1. In the barrel detector, the electric field is perpendicular to the magnetic field, resulting in a maximum Lorentz deflection. For the forward pixel detector, the electric and magnetic field directions have an angle of  $20^\circ$ , resulting in an approximately 80% smaller Lorentz drift. Another factor is the different bias voltage applied to the sensors, 100 V for the barrel and 300 V for the forward pixels. For both barrel and forward pixel detectors, the values measured for 0 T agree well with no Lorentz drift, as expected.

The average cluster size in the local  $y$  direction is plotted in Fig. 3.9 as a function of  $\cot \beta$  for the barrel pixel detector. Here  $\cot \beta_{\min}$  is expected to be zero. Again, the

**Table 3.1:** Fit parameters for the measurements of the Lorentz angle from cosmic data for the barrel and forward pixel detector with and without magnetic field.

	barrel pixel		forward pixel	
	3.8 T	0 T	3.8 T	0 T
$\cot(\alpha_{\min})$	$-0.462 \pm 0.003$	$0.003 \pm 0.009$	$-0.074 \pm 0.005$	$0.018 \pm 0.017$
$C_{\text{RMS}}$	$0.135 \pm 0.019$	$0.192 \pm 0.040$	$0.313 \pm 0.037$	$0.219 \pm 0.097$
$L_{\text{slope}}$	$2.057 \pm 0.019$	$1.979 \pm 0.057$	$2.138 \pm 0.040$	$2.091 \pm 0.110$
$R_{\text{slope}}$	$1.781 \pm 0.018$	$1.961 \pm 0.058$	$2.123 \pm 0.032$	$2.140 \pm 0.110$
$A$	$1.113 \pm 0.012$	$1.032 \pm 0.040$	$0.920 \pm 0.029$	$0.959 \pm 0.072$
$\chi^2/\text{ndof}$	20.56/35	20.56/35	30.84/15	18.67/15

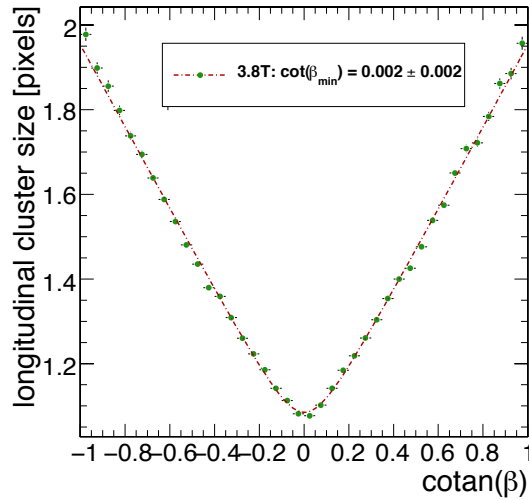


**Figure 3.9:** Cluster size along the local  $y$  direction as a function of impact angle  $\beta$  measured in the barrel pixel detector. Circles correspond to the measurement with 3.8 T while dashed lines show the fit to the data points.

result agrees well with expectation.

In Tab. 3.2 the measured values are compared to the values extracted from the PIXELAV simulation, using the same extraction method (*minimal-cluster-size* method). In the simulation the values of the reverse bias voltage are set to 100 V and 300 V for the barrel and forward pixel detectors, respectively. The sensor temperature was set to  $20^\circ$  and the Hall factor was assumed to be 1.02. The dependence of the charge carrier mobility on the electric field is taken from [32]. Good agreement between the measured data and the simulation is observed. Systematic errors on the predicted values are dominated by the uncertainty on the Hall mobility and can be as large as 10%.

In addition, a second method is applied to extract the Lorentz drift using the sample simulated with PIXELAV. This method compares the true impact position (obviously only available in simulation) to the reconstructed one as a function of the assumed Lorentz angle in the hit reconstruction (correcting the hit position for the Lorentz

**Table 3.2:** Comparison between the Lorentz angles extracted from cosmic data and the values obtained from the PIXELAV simulation, using the *minimal-cluster-size* method. The Lorentz angle can be obtained directly by minimising the reconstructed hit residuals (see text). The uncertainties are purely statistical.

$\theta_L$	cosmic data	PIXELAV simulation	
	<i>minimal-cluster-size</i>	<i>minimal-cluster-size</i>	<i>minimal-residual</i>
barrel	$(24.8 \pm 0.1)^\circ$	$(24.3 \pm 0.1)^\circ$	$(21.75 \pm 0.02)^\circ$
forward	$(4.2 \pm 0.3)^\circ$	$(4.2 \pm 0.3)^\circ$	$(3.80 \pm 0.02)^\circ$

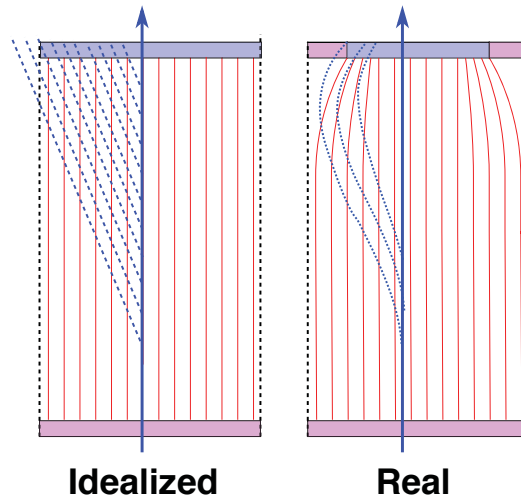


**Figure 3.10:** An illustration of the focussing effect. For an idealised detector the implant area covers the hole pixel. In reality, the implant is smaller than the pixel size, leading to a distortion of the electric field close to the implant. The electric field lines are shown in red and the drift lines of the charge carriers in blue.

drift). These residuals should be smallest for the correct Lorentz angle (*minimal-residual* method). A minimum for the residuals is achieved for a 10% lower value of the Lorentz angle (see Tab. 3.2). Since this is the value for an optimal position reconstruction, this value will be used as an input for the hit reconstruction.

This difference between the two methods using the same sample of simulated hits can be explained by the focussing effect: For the *minimal-cluster-size* method, the drift of the charge carriers is assumed to be linear, which is an approximation. As illustrated in Fig. 3.10, the implants are smaller than the pixel size, leading to a distortion of the electric field close to the implants. Thus the charge carriers are focused towards the implants. The focussing effect is modelled in the PIXELAV simulation and naturally captured by the *minimal-residual* method, but not by the *minimal-cluster-size* method due to the assumption of linear drift. This results in a smaller shift of the hit position seen by the *minimal-residual* method.

In order to test the assumption that the difference in the extracted Lorentz angle for the different measurement methods is due to this focussing effect, a simulation without this effect was used (the electric field was assumed to be linear throughout the detector, with implants covering the full pixel size). This simulation showed no difference between the two measurement methods (*minimal-cluster-size* and *minimal-residual*). This shows that there is a bias in the measurement of the average Lorentz angle from cosmic data, for which a correction of 10% has to be applied in order to use the value obtained in the reconstruction.

### 3.3 Measurement of the Lorentz angle from collision data

In proton-proton collision events, the Lorentz angle cannot be measured with the *minimal-cluster-size* method. This is due to the fact that the impact angle  $\alpha$  for tracks coming from the interaction point is always in the range of  $80^\circ \lesssim |\alpha| \lesssim 100^\circ$ . To cover the initial Lorentz angle, tracks up to at least  $120^\circ$  or  $-60^\circ$  for negative  $\alpha$  would be needed to obtain a sufficient fit range for the method. Thus a different method will be used for collision data, the so-called *grazing-angle* technique.

This method uses tracks which have a grazing angle in the beam direction (local  $y$  direction), i.e. a small angle  $\beta$ . As shown in Fig. 3.1, in the absence of a magnetic field, electrons produced by the track in red would be read out in pixels along the blue dashed line, as they drift along the electric field lines. In case of a magnetic field, electrons will drift such that they are read out in the pixels along the green line on the sensor surface. In the *grazing-angle* technique, the depth in which the charge carriers are produced, as well as their displacement along the  $x$  direction are estimated from track parameters. To obtain several measurement points in depth, a certain length in the  $y$  direction, from which the depth is obtained, is required. From the average displacement for different production depths, the Lorentz angle can be obtained. It is given by the slope of the resulting average displacement as a function of production depth.

A study of this *grazing-angle* technique on simulated events is presented. This study assumes a magnetic field of 4 T in the barrel pixel detector and uses single muon events with full CMS detector simulation, unless otherwise stated. This simulation assumes a linear drift of the electrons. The Lorentz angle can be set to different values.

In principle, all types of particles would be suitable for the measurement. To avoid nuclear interactions or electromagnetic showers, only muon tracks were used. Events for the measurement of the Lorentz angle are selected as follows:

- *Track selection:* Tracks associated with segments in the muon chambers are tagged as muon tracks. The muon reconstruction is described in [39]. Muon tracks are required to have a minimum transverse momentum of 3 GeV/ $c$  and a reduced  $\chi^2$  of less than two (see Fig. 3.11(a)).
- *Cluster selection:* In order to measure the drift length as a function of depth, only tracks with shallow impact angle with respect to the local  $y$  axis are used, which corresponds to tracks with a high pseudorapidity. Pixel hits in the muon track are therefore required to contain at least four pixels with signals above threshold along the local  $y$  direction (corresponding to approximately  $|\beta| < 35^\circ$  or  $|\beta| > 145^\circ$ ). Furthermore, to ensure a correct hit reconstruction and to avoid

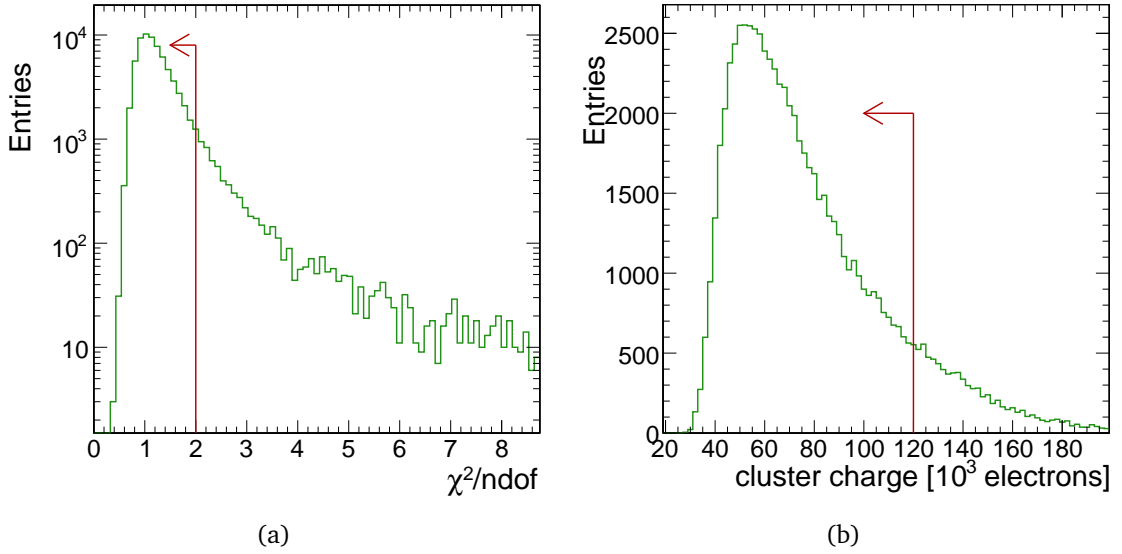


**Figure 3.11:** (a)  $\chi^2/\text{ndof}$  distribution for the track fits (simulation). To ensure a correct reconstruction, a  $\chi^2/\text{ndof} < 2$  is required. (b) Charge distribution deposited by a 10 GeV/c muon track which crosses the pixel ring located at  $\eta = 2$ . The charge is required to be less than 120 000 electrons.

satellite clusters due to secondary electrons, the total cluster charge has to be smaller than 120'000 electrons (see Fig. 3.11(b)). In addition, edge or double sized pixels are excluded.

The impact position is measured by extrapolating the track trajectory to each detector layer. For track reconstruction strip and pixel silicon detectors are used. The charge collected in the pixel sensor is shown as a function of the distance to the impact position in Fig. 3.12(a), with  $\Delta x$  and  $\Delta y$  defined as:

$$\begin{aligned}\Delta x &= x - x_0, \\ \Delta y &= y - y_0,\end{aligned}\tag{3.12}$$

where  $(x_0, y_0)$  is the track impact position on the sensor side bump-bonded to the readout chip, and  $(x, y)$  is the centre of the pixel cell. Without a magnetic field, the direction of the cluster's largest extension would be parallel to the track projection on the  $(x, y)$  plane. The width in  $x$  of the charge distribution is given by the pixel pitch along  $x$  (100  $\mu\text{m}$ ) while its length in  $y$  is given by  $z/\tan\beta$ .

The  $x$ -displacement of the electrons due to the magnetic field has to be calculated as function of the depth at which they were produced. The impact angles of the track (Fig. 3.4) are defined in Eq. 3.9. One can then calculate the displacement  $d$  due to the magnetic field and the production depth  $z$  of the electrons as follows:

$$\begin{aligned}d &= \Delta x - \Delta y \cdot \tan\gamma, \\ z &= \Delta y \cdot \tan\beta.\end{aligned}\tag{3.13}$$

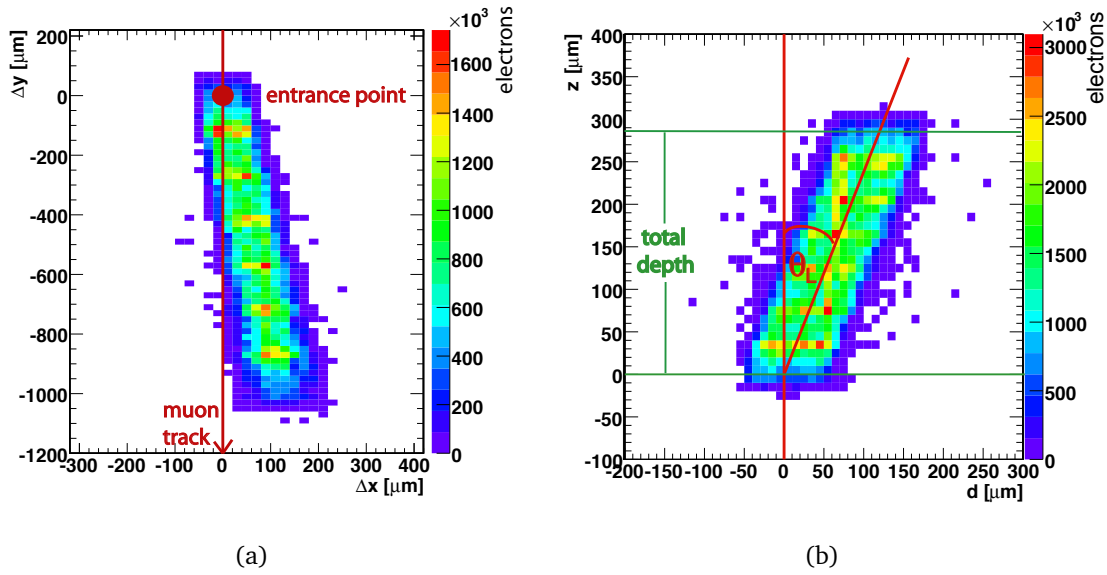


**Figure 3.12:** (a) Pixel charge distribution as a function of distance to the track impact coordinates in  $x$  and  $y$ . (b) Electron production depth  $z$  versus their displacement  $d$ . Both figures are for muon tracks crossing the barrel ring located at  $\eta = 2$ .

The  $x$ -displacement of the electrons as function of depth is determined from a large number of tracks (Fig. 3.12). The tangent of the Lorentz angle is equal to the slope of the distribution: The average displacement of an electron created at a certain depth is obtained from Fig. 3.12(b). A linear fit is performed over the total thickness of the sensor, excluding the first and last  $50 \mu\text{m}$  where the charge drift is systematically displaced by the finite size of the pixel cell (Fig. 3.13(a)).

Since irradiation will not be uniform across the detector, the Lorentz angle has to be determined independently for different regions of pseudorapidity. The barrel pixel detector is subdivided into three layers, which are further subdivided into eight rings, corresponding to the eight modules along the direction of the beam-pipe (see Fig. 3.14). Fit results for an assumed Lorentz angle of  $23^\circ$  in the simulation are shown in Fig. 3.13(b). The results match the assumed value to an accuracy of 2%, although the two central rings (4,5) in the outermost layer clearly require more statistics. Due to the requirement of the shallow angle in the  $y$  direction, resulting in a high pseudorapidity, only tracks which are highly displaced from the nominal interaction point ( $\approx 15 \text{ cm}$ ) hit the two central pixel detector rings, resulting in a smaller track sample at central rapidities.

### 3.3.1 Study of systematic errors

In this section, possible sources of systematic uncertainties impairing the Lorentz angle measurement are investigated.

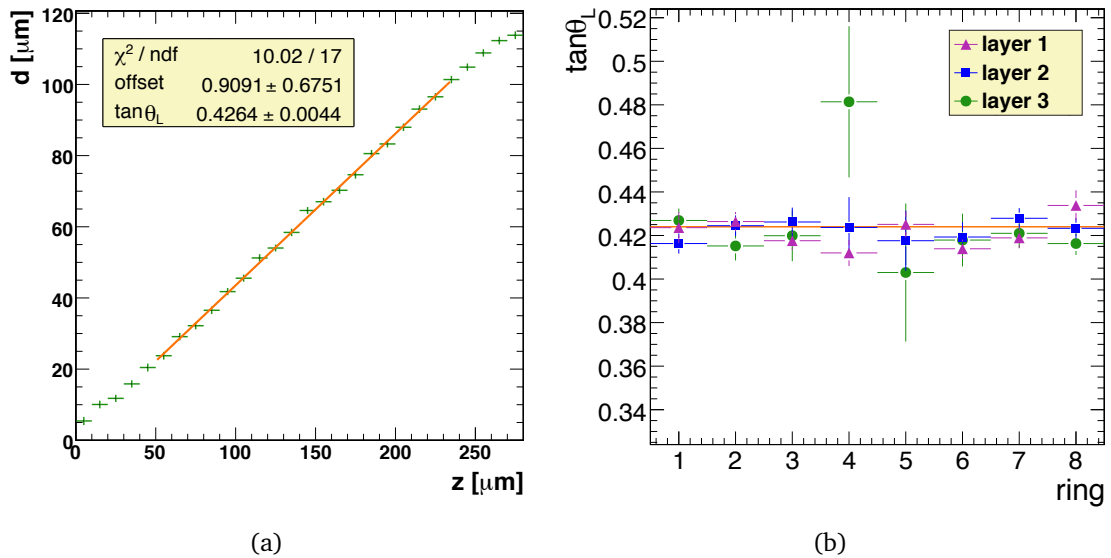


**Figure 3.13:** (a) Average displacement  $d$  of electrons as a function of production depth  $z$  in the silicon sensor bulk. The solid line shows the fit. (b) Results for  $\tan\theta_L$  for the three barrel layers and eight detector rings. The solid line shows the simulated value of  $\tan\theta_L = 0.424$  corresponding to  $\theta_L = 23^\circ$ .

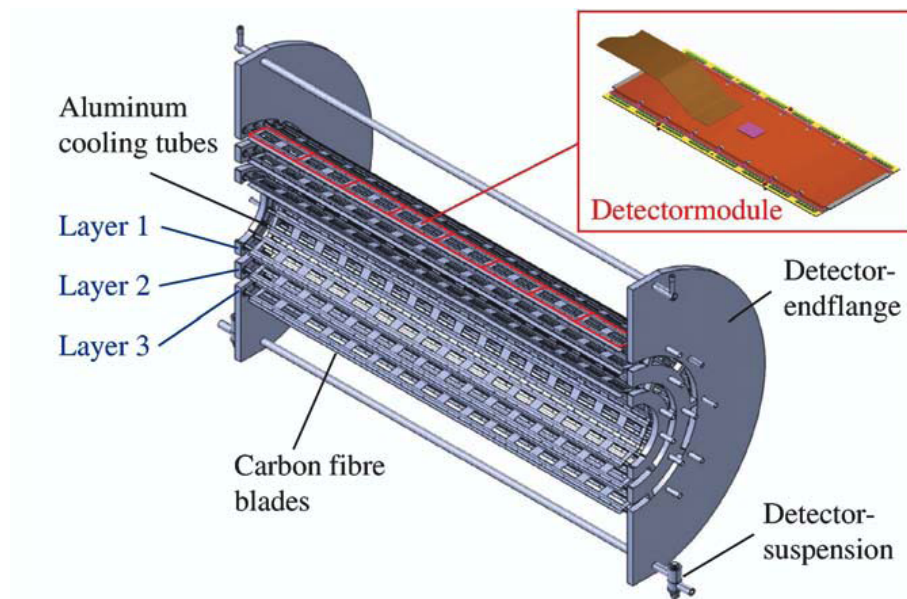


**Figure 3.14:** Mechanical layout of one barrel pixel detector half shell. Eight detector modules are mounted on each ladder (shown in red) leading to eight rings of pseudorapidity.

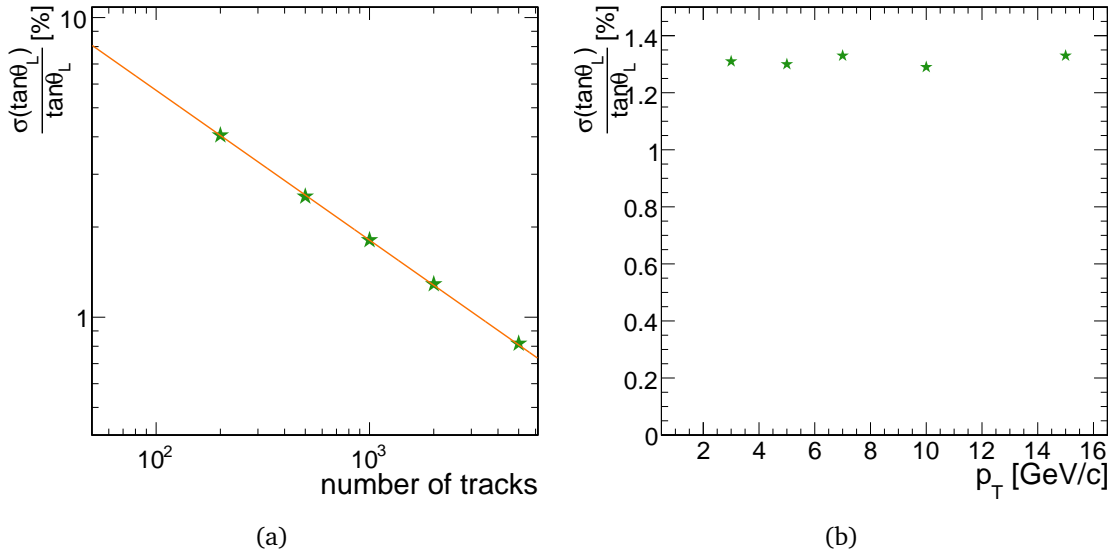


**Figure 3.15:** (a) Relative uncertainty of  $\tan\theta_L$  as a function of the number of tracks. The solid stars show the measurement while the line shows the fit, assuming a square-root-dependency on the number of tracks. As shown in Fig.(b), the relative uncertainty is independent of the transverse muon momentum down to 3 GeV/c.

First, the dependence of the uncertainty of the Lorentz angle measurement on the number of tracks is examined. As shown in Fig. 3.15(a), the relative uncertainty of  $\tan\theta_L$  is inversely proportional to the square root of the number of tracks. To achieve a relative uncertainty of 2%, approximately 1000 tracks are needed in each ring. For a Lorentz angle of  $23^\circ$ , this corresponds to an uncertainty of less than  $0.5^\circ$  or a displacement in  $x$  of  $1.14\ \mu\text{m}$ .

Therefore, to maximise the number of muon tracks, the muon transverse momentum cut should be set as low as possible. I investigated whether multiple scattering would increase the relative uncertainty for low momentum muons. The Lorentz angle is measured for muon samples generated at different momenta. As shown in Fig. 3.15(b), there is no dependence of the relative uncertainty of  $\tan\theta_L$  on the transverse momentum down to 3 GeV/c nor is there a bias on the measurement. Based on this result, muons with a transverse momentum as low as 3 GeV/c are used for the measurement of the Lorentz angle. Muons with lower transverse momentum cannot be reconstructed with the CMS detector.

### 3.3.1.1 Different simulation values of the Lorentz angle

Since the Lorentz angle decreases with increasing bias voltage, the measurable drift length will be smaller. To determine whether smaller Lorentz angles can be measured, I applied the *grazing-angle* method to data with Lorentz angles set to  $15^\circ$  and  $8^\circ$



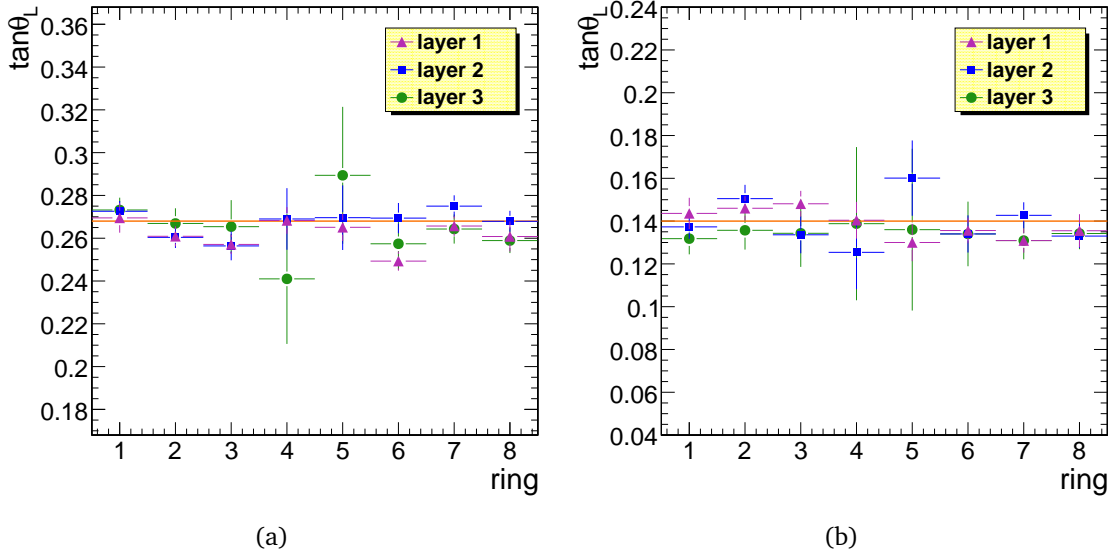


**Figure 3.16:** Results for  $\tan\theta_L$  for the three layers and eight detector rings for an input value of  $\tan\theta_L = 0.268$  ( $\theta_L = 15^\circ$ , (a)) and  $\tan\theta_L = 0.140$  ( $\theta_L = 8^\circ$ , (b)).

in the simulation. Fig. 3.16 shows the results: The absolute uncertainties of the measurements are similar to the ones for  $\theta_L = 23^\circ$  (see Fig. 3.13(b)).

Hit reconstruction from raw detector data requires an estimated Lorentz angle as input. The actual Lorentz angle measurement is then based on these reconstructed hits. Thus it is important to demonstrate that a wrong Lorentz angle assumption in the hit reconstruction does not bias the measured Lorentz angle.

This can be seen from Eq. 3.13: A wrong Lorentz angle yields a wrong position in  $x$  but not in  $y$ . Thus the function  $d(z)$  in Fig. 3.13(a) is offset by a constant only, but its slope  $\tan\theta_L$  is unchanged.

To investigate the influence of a wrong Lorentz angle assumption numerically, a sample of events simulated with  $\theta_L = 23^\circ$  in the barrel pixel detector was reconstructed assuming  $\theta_L = 18^\circ$  (i.e. a value 20% too small), which implied a systematic shift of  $15\ \mu\text{m}$  in the measured pixel hit  $x$ -position. All other parameters in the simulation and reconstruction were left unchanged. The measured Lorentz angle agrees with the simulated value of  $\theta_L = 23^\circ$  and is not biased by the wrong value assumed in the pixel hit reconstruction (see Fig. 3.17).

### 3.3.1.2 Impact of wrong Lorentz angle on hit resolution

An error of the Lorentz angle used during hit reconstruction leads to a systematic shift in its position. The reconstructed  $x$ -position will be shifted by

$$\delta x = \delta [\tan\theta_L] \cdot \bar{z}, \quad (3.14)$$

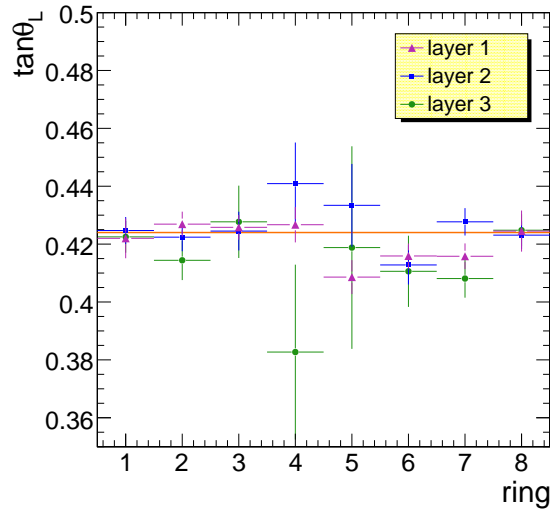


**Figure 3.17:**  $\tan \theta_L$  measured for the three layers as a function of the detector ring number. The solid line shows the simulated value of  $\tan \theta_L = 0.424$  corresponding to  $\theta_L = 23^\circ$ . A wrong Lorentz angle of  $\tan \theta_L = 0.320$  corresponding to  $\theta_L = 18^\circ$  was assumed in the reconstruction.

where  $\delta [\tan \theta_L]$  is the error of  $\tan \theta_L$  and  $\bar{z} = 285/2 \mu\text{m}$  is the mean depth of charge carrier production. An error of 2% on  $\tan \theta_L$  leads to a shift of  $1.14 \mu\text{m}$ . To verify this the shift was measured on a sample of generated single muon events by setting  $\tan \theta_L$  in the reconstruction 2% lower than in the simulation, namely  $\theta_L = 22.6^\circ$ . As shown in Fig. 3.18, the measured shift  $\delta x$  is  $1.5 \pm 0.2 \mu\text{m}$ , close to the expected value. The width of the distribution is not changed. The shift is significantly smaller than the position resolution. The alignment procedure of the pixel detector is expected to absorb this shift, because it will not be possible to distinguish between a real shift of a detector module and the shift due to the Lorentz angle.

### 3.3.1.3 Tracker misalignment studies

Results presented so far in Section 3.3 are obtained assuming a perfect alignment of the detectors in the tracker. To investigate the sensitivity of the method to misalignment, the study is repeated assuming the imperfect alignment that could be expected after accumulating an integrated luminosity of about  $10 \text{ pb}^{-1}$ . In this scenario, an educated guess is made on how well the position of the detectors will be known after taking data for a luminosity of  $10 \text{ pb}^{-1}$ . The RMS position uncertainty of the sensors, ladders, and half cylinders is assumed to be  $60 \mu\text{m}$ ,  $10 \mu\text{m}$ , and  $10 \mu\text{m}$ , respectively. Two sets of simulated Drell-Yan events are used: one sample is reconstructed assuming perfect alignment, while the second is reconstructed with the misaligned scenario, using a total of about 400 000 events. The reason for using the Drell-Yan samples was of practical origin. They were already available and didn't need to be generated, sav-

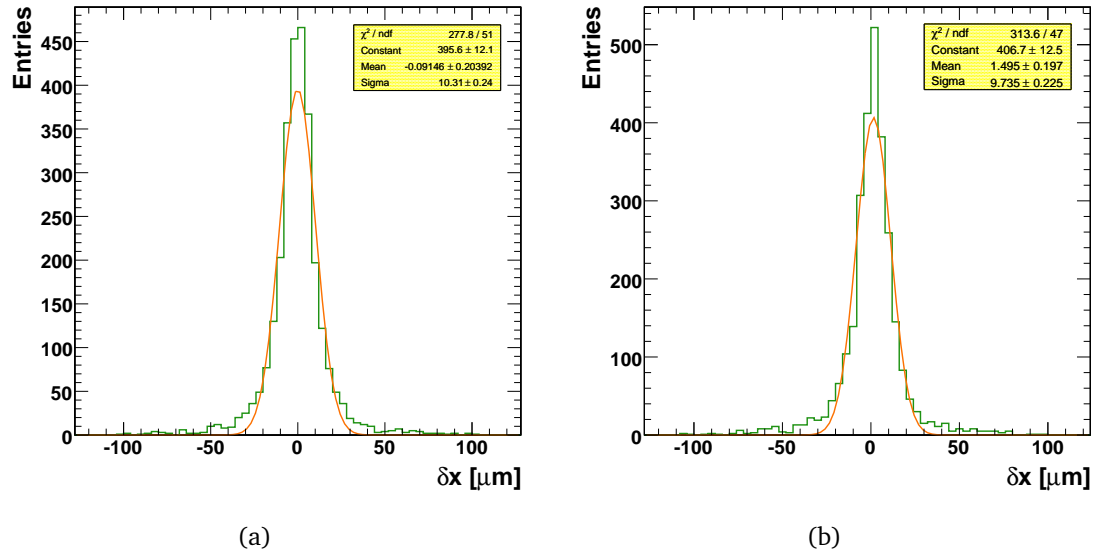


**Figure 3.18:** Residual distribution of reconstructed hits in the x-direction, (a) for the correct Lorentz angle, (b) for a Lorentz angle of  $22.6^\circ$  instead of  $23^\circ$ , leading to a shift of  $1.5 \mu\text{m}$ .

ing much time. Fig. 3.19 shows the results. The measured values agree with the simulation in both cases and the achieved precision is roughly 0.5% for most rings, reaching 4% for the outermost central rings.

## 3.4 Conclusions

With a sample of 85 000 tracks from cosmic rays passing through the pixel detector in October 2008, the Lorentz angle was measured in the silicon pixel detector using the *minimal-cluster-size* method. The measured values are  $24.8 \pm 0.1^\circ$  for the barrel pixel detector (where the magnetic field is perpendicular to the electric field) and  $4.2 \pm 0.3^\circ$  for the forward pixel detector (here the angle between the electric and magnetic fields is  $20^\circ$  as shown in Fig. 3.4 ).

The extracted values for the barrel as well as for the forward detectors agree well with the values extracted from a detailed simulation of the silicon sensors (PIXELAV) using the same *minimal-cluster-size* method (Tab. 3.2). However, the average Lorentz angle is in fact 10% lower due to the strong focussing field near the sensors. Thus an effective Lorentz angle of  $21.75^\circ$  for the barrel pixel and  $3.8^\circ$  for the forward pixel detectors will be used.

Measuring the Lorentz angle for a 0 T magnetic field yielded values compatible with  $0^\circ$ , as expected. The measurement was repeated in the longitudinal direction for the

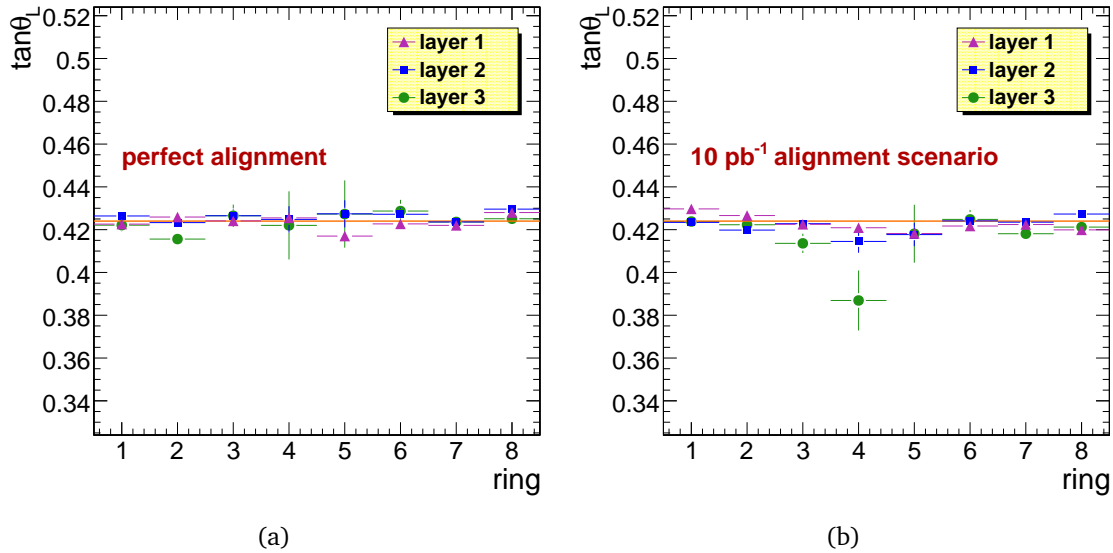


**Figure 3.19:** Measured  $\tan \theta_L$  for each of the three layers as a function of detector ring number. Simulated Drell Yan events are reconstructed for a perfectly aligned detector (a) and for the  $10 \text{ pb}^{-1}$  alignment scenario (b).

barrel detector, where no displacement due to the Lorentz drift is expected. Again, the result is compatible with  $0^\circ$ .

A method to measure the Lorentz angle in the barrel pixel detector with tracks from collision data was also developed (*grazing-angle technique*). Due to the different range of impact angle  $\alpha$ , the *minimal-cluster-size* method cannot be used. Due to the expected inhomogeneous irradiation the measurement will be performed for eight sensor positions (rings) along the beam direction and for the three layers of the pixel barrel detector independently. Muons were used for this study since they have a low probability to undergo multiple scattering and thus provide an accurately measured track. This method offers the possibility to measure the Lorentz angle with a precision of 2% (i.e.  $0.5^\circ$ ) using only 1000 tracks for each pixel ring. This will lead to an inaccuracy of  $1.5 \mu\text{m}$  in the  $x$ -direction which is much smaller than the hit resolution of  $10 \mu\text{m}$ . For a larger number of tracks used in the Lorentz angle measurement, the uncertainty will decrease accordingly.

I showed that for muon tracks down to  $3 \text{ GeV}/c$ , the lowest trigger threshold for muons, can be used. This will provide samples with much more than 1000 muon tracks per ring for this measurement. For the central rings one requires vertices displaced by  $\approx 15 \text{ cm}$  along the beam-line direction from the detector center. More integrated luminosity will therefore be needed to achieve the same accuracy as for the other modules. High quality hadron tracks in addition to muon tracks could be used to increase the overall statistics.

Furthermore we have proven that the absolute accuracy in the Lorentz angle mea-

surement with the *grazing-angle* method does not depend on the value of the Lorentz angle. Thus, this provides a method to monitor the Lorentz angle for the barrel pixel detector throughout its lifetime. I have demonstrated that a 20% error in the assumed Lorentz angle in the pixel hit reconstruction does not bias the Lorentz angle measurement. Additional tests show that the impact of misalignment in the startup phase of the CMS detector does not increase the uncertainty in the Lorentz angle measurement.



# Chapter 4

## Study of the decay

$$B_s \rightarrow J/\psi (\rightarrow \mu^+ \mu^-) \phi (\rightarrow K^+ K^-)$$

As already discussed in Chapter 1, the decay  $B_s \rightarrow J/\psi (\rightarrow \mu^+ \mu^-) \phi (\rightarrow K^+ K^-)$  is of particular interest since it allows to study many properties of the  $B_s$  system, such as the differences between the widths ( $\Delta\Gamma_s$ ) and masses ( $\Delta m_s$ ) of the two weak eigenstates  $B_s^L$  and  $B_s^H$ . Furthermore, this decay provides one of the best ways to determine the height of the unitarity triangle, called  $\eta$  in the Wolfenstein parametrisation, by measuring the CP violating phase  $\phi_s = 2\lambda^2\eta$  (see Chapter 1). Therefore, the decay  $B_s \rightarrow J/\psi (\rightarrow \mu^+ \mu^-) \phi (\rightarrow K^+ K^-)$  has been chosen to be one of the channels of highest interest during the initial runs of CMS [40, 41].

The aim of the analysis presented here is a study of the measurement of the width difference  $\Delta\Gamma_s$  on a sample of untagged  $B_s \rightarrow J/\psi (\rightarrow \mu^+ \mu^-) \phi (\rightarrow K^+ K^-)$  candidates, where untagged means that no distinction between  $B_s$  and  $\bar{B}_s$  is made. Events are selected with a dedicated trigger and offline reconstruction for  $B_s$  events. In this thesis a likelihood fit of the time-dependent angular distributions is developed, tested and applied to simulated  $B_s$  events. The sensitivity to  $\Delta\Gamma_s$  and  $\phi_s$  is estimated for a luminosity of  $1.3 \text{ fb}^{-1}$ .

The simulation of the signal and background samples is discussed in Section 4.1. The trigger selection is described in Section 4.2 and the offline selection and reconstruction are presented in Section 4.3. The maximum likelihood fit is described in Section 4.4, and its validation test in Section 4.4.1. The results are presented in Section 4.4.5, followed by a discussion of the systematic uncertainties in Section 4.4.6.

## 4.1 Signal and background samples

For the samples composed of events with decays of  $B$  hadrons, the Monte Carlo generation started from a sample of 56 million parton-level  $b\bar{b}$  events, selected out of a total of 2.5 billion inclusive QCD events generated with the PYTHIA 6.215 generator [42]. The three different contributions to the total cross section (parton fusion, flavour excitation and gluon splitting) are taken into account (for this, the MSEL=1 card was used).

The datasets of interest were produced by forcing the fragmentation of  $b$  quarks to specific final states and applying kinematic cuts to select those events in which the final state particles are inside the acceptance of the CMS detector. This step of the simulation was performed using the SIMUB generator [43], which is dedicated to the production of  $B$  physics events and was developed by the  $B$  physics group of the CMS collaboration. SIMUB is interfaced to PYTHIA to perform hadronization of partons to the final state particles. This is necessary since in PYTHIA the angular distributions of the final decay products (as described in Chapter 1) are not taken into account. Therefore, SIMUB takes over the generation for the decay of interest, fully reproducing the angular distributions of the decay products. Using the generated SIMUB data as input, the CMS detector response was simulated using GEANT4 [44] using a full detector description (see [41] for more details). Since the detector simulation is very time consuming (several minutes per event), events were pre-selected after generation with SIMUB and before detector simulation. This pre-selection is outlined in the following sections. All samples are simulated for a centre-of-mass energy of  $\sqrt{s} = 14$  TeV and with pile-up corresponding to a luminosity of  $\mathcal{L} = 2 \times 10^{33} \text{ cm}^{-2}\text{s}^{-1}$ .

### 4.1.1 Simulation of the $B_s \rightarrow J/\psi \phi$ signal

A sample of approximately 500'000 signal events has been generated, forcing one of the  $b$  quarks to hadronize as a  $B_s$  (or  $\bar{B}_s$ ) meson and to decay through the decay chain  $B_s/\bar{B}_s^0 \rightarrow J/\psi (\rightarrow \mu^+ \mu^-) \phi (\rightarrow K^+ K^-)$ . The parameters used as input in the simulation are summarized in Tab. 4.1. The following kinematic cuts were applied on the generated particles:

$$\begin{aligned} p_T(\mu) &> 3 \text{ GeV}/c & \text{for} & & |\eta(\mu)| < 1.2, \\ p_T(\mu) &> 2 \text{ GeV}/c & \text{for} & & 1.2 \leq |\eta(\mu)| < 2.5, \\ p_T(K) &> 0.8 \text{ GeV}/c & \text{for} & & |\eta(K)| < 2.5. \end{aligned} \quad (4.1)$$

The cross section for this channel at an LHC energy of  $\sqrt{s} = 14$  TeV, including the kinematic cuts, may be written as follows:

$$\begin{aligned} \sigma(B_s \rightarrow J/\psi \phi) &= \sigma(b\bar{b}) \cdot 2 \cdot B(\bar{b} \rightarrow B_s) \cdot \mathcal{B}(B_s \rightarrow J/\psi \phi) \cdot \\ &\cdot \mathcal{B}(J/\psi \rightarrow \mu^+ \mu^-) \cdot \mathcal{B}(\phi \rightarrow K^+ K^-) \cdot \epsilon_{\text{kin}}, \end{aligned} \quad (4.2)$$



parameter	assumed value
$\tau_s = 1/\bar{\Gamma}_s$	$1.405 \times 10^{-12} \text{ s}$
$\Delta\Gamma_s/\bar{\Gamma}_s$	-0.2
$\Delta m_s$	$17.8 \text{ ps}^{-1}$
$ A_0(0) ^2/\Gamma_s$	0.570
$ A_{\parallel}(0) ^2/\Gamma_s$	0.217
$ A_{\perp}(0) ^2/\Gamma_s$	0.213
$\delta_1$	$\pi$
$\delta_2$	0
$\phi_s$	-0.04

**Table 4.1:** Input values for the  $B_s$  mixing parameters, decay amplitudes, strong and weak phases in the simulation of the  $B_s \rightarrow J/\psi\phi$  Monte Carlo sample [9].

where  $\mathcal{B}(A \rightarrow B)$  is the branching fraction for the decay  $A \rightarrow B$ . The factor  $\epsilon_{kine} = (2.5890 \pm 0.0024) \cdot 10^{-2}$ , which is the probability for the final decay products (on generation level) to pass the kinematic cuts, is obtained from the SIMUB Monte Carlo generator (the quoted error is statistical). The total cross section on  $b\bar{b}$  production at  $\sqrt{s} = 14 \text{ TeV}$  is expected to be  $\sigma(b\bar{b}) = 100 - 1000 \mu\text{b}$  [45]. For the startup energies of  $\sqrt{s} = 10 \text{ TeV}$  and  $\sqrt{s} = 7 \text{ TeV}$  the cross section is expected to drop with respect to  $\sqrt{s} = 14 \text{ TeV}$  by approximately 25% and 50% respectively [46]. Throughout this analysis a cross section of  $\sigma(b\bar{b}) = 500 \mu\text{b}$  is assumed and the experimentally measured values [12] are taken for the branching ratios:

$$\begin{aligned}
\mathcal{B}(\bar{b} \rightarrow B_s) &= (10.7 \pm 1.1) \cdot 10^{-2}, \\
\mathcal{B}(B_s \rightarrow J/\psi\phi) &= (9.3 \pm 3.3) \cdot 10^{-4}, \\
\mathcal{B}(J/\psi \rightarrow \mu^+\mu^-) &= (5.88 \pm 0.10) \cdot 10^{-2}, \\
\mathcal{B}(\phi \rightarrow K^+K^-) &= (49.1 \pm 0.6) \cdot 10^{-2},
\end{aligned}$$

the predicted cross section for  $B_s$  production and decay is

$$\sigma(B_s \rightarrow J/\psi(\rightarrow \mu^+\mu^-)\phi(\rightarrow K^+K^-)) = 74 \pm 27 \text{ pb}. \quad (4.3)$$

The error on this estimate does not include the error induced by the uncertainties on the total  $b\bar{b}$  cross section at LHC energies and the uncertainties on the transverse momentum distribution of  $b$  quarks, which can be as large as 50% [47]. However, since both the signal and the background are proportional to the same  $b\bar{b}$  cross section, the signal-to-background ratio is unaffected by the corresponding uncertainty.

#### 4.1.2 Simulation of the $B_d \rightarrow J/\psi K^*$ background

A sample of almost 500'000 events has been generated, forcing one of the  $b$  quarks to hadronize as a  $B^0$  (or  $\bar{B}^0$ ) meson, and to decay into  $J/\psi(\rightarrow \mu^+\mu^-)K^*(\rightarrow K^+\pi^-)$ . The

parameter	assumed value
$\tau_d = 1/\Gamma_d$	$1.528 \times 10^{-12}$ s
$\Delta\Gamma_d/\Gamma_d$	0
$\Delta m_d$	$0.509$ ps <sup>-1</sup>
$ A_0(0) ^2/\Gamma_d$	0.570
$ A_{\parallel}(0) ^2/\Gamma_d$	0.217
$ A_{\perp}(0) ^2/\Gamma_d$	0.213
$\delta_1$	$\pi$
$\delta_2$	0

**Table 4.2:** Input values for the  $B_d$  mixing parameters, decay amplitudes, strong and weak phases in the simulation of the  $B_d \rightarrow J/\psi K^*$  Monte Carlo sample [9].

parameters used as input for the simulation are summarized in Tab. 4.2. The same kinematic cuts are applied as in the case of the signal sample (with the substitution of a kaon with a pion in the final state). The cross section for this decay chain may be written as follows:

$$\begin{aligned} \sigma(B_d \rightarrow J/\psi K^*) &= \sigma(b\bar{b}) \cdot 2 \cdot B(\bar{b} \rightarrow B_d) \cdot \mathcal{B}(B_d \rightarrow J/\psi K^*) \cdot \\ &\quad \cdot \mathcal{B}(J/\psi \rightarrow \mu^+ \mu^-) \cdot \mathcal{B}(K^{*0} \rightarrow K^+ \pi^-) \cdot \epsilon_{\text{kin}} \end{aligned} \quad (4.4)$$

with  $\epsilon_{\text{kin}} = (1.7972 \pm 0.0020) \cdot 10^{-2}$  obtained from the Monte Carlo generator. Assuming  $\sigma(b\bar{b}) = 500 \mu\text{b}$  at 14 TeV, and taking for the branching ratios the experimentally measured values [12]:

$$\begin{aligned} B(\bar{b} \rightarrow B_d) &= (39.8 \pm 1.0) \cdot 10^{-2}, \\ \mathcal{B}(B_d \rightarrow J/\psi K^*) &= (1.31 \pm 0.07) \cdot 10^{-3}, \\ \mathcal{B}(J/\psi \rightarrow \mu^+ \mu^-) &= (5.88 \pm 0.10) \cdot 10^{-2}, \end{aligned}$$

with  $\mathcal{B}(K^{*0} \rightarrow K^+ \pi^-) = 2/3$  by isospin symmetry, the predicted cross section is

$$\sigma(B_d \rightarrow J/\psi K^* \rightarrow \mu^+ \mu^- K^+ \pi^-) = 366 \pm 22 \text{ pb} . \quad (4.5)$$

Again, the error quoted on this estimate does not include the error induced by the uncertainties on the total  $b\bar{b}$  cross section at LHC energies and the uncertainties on the transverse momentum distribution of  $b$  quarks.

### 4.1.3 Simulation of the $b \rightarrow J/\psi X$ background

Two inclusive samples of events containing decays of  $B$  hadrons to final states with a  $J/\psi$  resonance were simulated, discarding the decays to the exclusive final states previously described to prevent double counting. The  $J/\psi$  was forced to decay into a pair of muons.

In sample **A** 380'000 events were generated with only the kinematic cuts used for the muons in the signal sample applied (see Eq. 4.1).

To increase the background statistics, 154'000 events were generated for sample **B** selecting only events which might fake a  $B_s \rightarrow J/\psi \phi$  decay:

- a pair of oppositely charged particles (assuming kaons) with  $p_T > 0.5$  GeV/c and  $|\eta| < 2.5$  forming a fake  $\phi$  candidate was searched for in a region ( $|\Delta\eta| < 1.5, |\Delta\varphi| < 1.5$ ) around the  $J/\psi$  direction and with invariant mass within 30 MeV/c<sup>2</sup> of the world-average  $\phi$  mass ( $0.99$  GeV/c<sup>2</sup>  $< m(K^+K^-) < 1.05$  GeV/c<sup>2</sup>).
- the fake  $\phi$  candidate was requested to form a fake  $B_s$  candidate in combination with the  $J/\psi$  with an invariant mass within 300 MeV/c<sup>2</sup> of the world-average  $B_s$  mass ( $5.07$  GeV/c<sup>2</sup>  $< m(\mu^+\mu^-K^+K^-) < 5.67$  GeV/c<sup>2</sup>).

For the inclusive background samples, no detailed simulation of angular distributions of the final decay products was performed, and  $B$  hadron decays were simulated with PYTHIA (phase space distributed). The cross section for this decay chain at LHC energies (14 TeV), including the kinematic cuts, may be written as follows:

$$\sigma(b \rightarrow J/\psi X) = \sigma(b\bar{b}) \cdot 2 \cdot B(b \rightarrow J/\psi) \cdot \mathcal{B}(J/\psi \rightarrow \mu^+\mu^-) \cdot \epsilon_{sel}.$$

The factor  $\epsilon_{sel}$  for this decay, obtained from the Monte Carlo generator, is  $(4.088 \pm 0.006) \cdot 10^{-2}$  for the sample **A** and  $(4.69 \pm 0.01) \cdot 10^{-3}$  for the sample **B**. Assuming  $\sigma(b\bar{b}) = 500$   $\mu\text{b}$  at 14 TeV, and taking the experimentally measured values [12]

$$\begin{aligned} \mathcal{B}(\bar{b} \rightarrow J/\psi) &= (1.16 \pm 0.10) \cdot 10^{-2}, \\ \mathcal{B}(J/\psi \rightarrow \mu^+\mu^-) &= (5.88 \pm 0.10) \cdot 10^{-2}, \end{aligned}$$

for the branching ratios, the predicted cross section is then

$$\sigma(b \rightarrow J/\psi X) = 27.9 \pm 2.4 \text{ nb} \quad (4.6)$$

for sample **A**, and

$$\sigma(b \rightarrow J/\psi X) = 3.20 \pm 0.3 \text{ nb} \quad (4.7)$$

for sample **B**.

Again, the error on this estimate does not include the uncertainty on the total  $b\bar{b}$  cross section at LHC energies and the uncertainties on the transverse momentum distribution of  $b$  quarks; however, since both signal and background are proportional to that cross section, the signal-to-background ratio is unaffected by the uncertainty.

#### 4.1.4 Direct $J/\psi$ production at LHC

The direct production of  $J/\psi$  mesons is an important background at trigger level. Measurements at the Tevatron [48] have shown that predictions of the colour-singlet

sample	# generated events	cross-section	corresponding luminosity
$B_s \rightarrow J/\psi \phi$	507'888	$74 \pm 27$ pb	$6.8 \text{ fb}^{-1}$
$B_d \rightarrow J/\psi K^*$	486'000	$366 \pm 22$ pb	$1.3 \text{ fb}^{-1}$
<b>A:</b> $b \rightarrow J/\psi X$	380'000	$27.9 \pm 2.4$ nb	$13.6 \text{ pb}^{-1}$
<b>B:</b> $b \rightarrow J/\psi X$	154'000	$3.20 \pm 0.3$ nb	$48 \text{ pb}^{-1}$
direct $J/\psi$	270'000	$176 \pm 2$ nb	$1.53 \text{ pb}^{-1}$

**Table 4.3:** Number of generated events for the signal and different background channels, as well as their cross-section and the corresponding integrated luminosity.

model, which is presently the one implemented in the PYTHIA generator, underestimates the production by several orders of magnitude. Perturbative QCD is used in this model to generate  $c\bar{c}$  pairs, which then hadronize to a charmonium state in a non-perturbative way.

This discrepancy has led to a different approach [49] which has been implemented in a modified version of PYTHIA 6.225, tuned on Tevatron data. A  $c\bar{c}$  pair is first formed taking into account all perturbative QCD diagrams, regardless of the final colour state. The  $c\bar{c}$  state is then transformed into a colour-singlet by non-perturbative processes, such as the emission of a soft gluon.

This version of PYTHIA has been used to simulate a sample of  $J/\psi$  decaying into two muons with the same kinematic cuts as applied on the signal sample. The  $J/\psi$  production cross section is calculated to be  $140.6 \mu\text{b}$ . With the  $J/\psi \rightarrow \mu^+\mu^-$  branching ratio and the kinematic cuts, a cross section of  $176 \pm 2$  nb is expected. Again the uncertainty is statistical only; the uncertainties on the total cross section for  $J/\psi$  production and on the  $p_T$  distribution are not included. A sample of 270 000 events has been generated, corresponding to an integrated luminosity of  $1.53 \text{ pb}^{-1}$ .

All samples are summarised in Tab. 4.3.

## 4.2 Trigger reconstruction and selection

### 4.2.1 Level-1 Trigger

The  $B_s \rightarrow J/\psi(\rightarrow \mu^+\mu^-)\phi(\rightarrow K^+K^-)$  decay chain is selected at Level-1 by the di-muon trigger stream (see Section 2.2.4 for a description of the Level-1 trigger). At low luminosity ( $\mathcal{L} = 2 \times 10^{33} \text{ cm}^{-2}\text{s}^{-1}$ ) it is foreseen [50] to use an identical threshold of 3 GeV/c on the transverse momentum for both muons, while still keeping a low bandwidth occupancy of 0.9 kHz (out of the 100 kHz total Level-1 rate). Such a low  $p_T$  threshold ensures a very high selection efficiency for this channel. The di-

sample	$B_s \rightarrow J/\psi \phi$	direct $J/\psi$	<b>A:</b> $b \rightarrow J/\psi X$	<b>B:</b> $b \rightarrow J/\psi X$	$B_d \rightarrow J/\psi K^*$
$\sigma$ (nb)	0.074	176	27.9	3.20	0.366
L1 $\epsilon$	0.5764(7)	0.4890(13)	0.5041(13)	0.4972(13)	0.58.61(13)
L1 R (Hz)	0.0853(1)	173.1(4)	28.93(7)	3.192(8)	0.471(1)
OS:					
L1 $\epsilon$	0.4576(6)	0.3691(12)	0.3819(13)	0.3825(13)	0.4691(13)
L1 R (Hz)	0.0677(1)	130.7(4)	21.92(7)	2.455(8)	0.377(1)

**Table 4.4:** Efficiency  $\epsilon$  (defined with respect to the number of generated events) and Level-1 trigger rate  $R$  of the di-muon trigger selection before and after the requirement that at least two triggered muons have opposite charge sign (OS). The errors are statistical. Systematic uncertainties will be discussed in Section 4.4.6.

muon trigger rate is also low enough for lower quality muon candidates in the endcap region, recovering full geometrical acceptance of the muon detector up to  $|\eta| < 2.4$ .

The efficiency of the Level-1 di-muon Trigger applied to the Monte Carlo sample of the signal channel is reported in Tab. 4.4, together with the efficiencies on the different background samples. Imposing the additional requirement that two of the reconstructed muon candidates have opposite charge, the efficiency on the signal sample is lowered from 0.576 to 0.458 due to the high fraction of muon candidates with incorrect charge assignment. While it would be possible to recover this efficiency loss at Level-1 by omitting the requirement that muon candidates have different charges, we shall see that the error in the charge assignment would still lead to an incorrect definition of the region in which the High Level Trigger reconstruction searches for the muon (region of interest). Therefore, it was decided to discard these events anyway.

The distribution of residuals in pseudo-rapidity  $\eta$  of the muons (difference between  $\eta_{L1}^{\text{rec}}$  returned by the L1 trigger and the generated value  $\eta^{\text{sim}}$ ) is shown in Fig. 4.1. The distribution of the muons is almost flat in  $\eta$  for the region of interest for this analysis ( $|\eta| \lesssim 2.5$ ). With an uncertainty of  $\sigma_\eta = 0.05$ , the rapidity is already quite well estimated at Level-1.

The value of the  $\varphi$  angle returned by the Level-1 Trigger is measured at the second muon chamber station [51], and is therefore measured after the muon tracks have been deflected in the magnetic field. This effect is illustrated in Fig. 4.2. The red arrow shows the original direction of the muon and the green arrow shows the direction of the muon measured by the second muon chamber. The discrepancy in  $\varphi$  between these two directions is about  $\pm 0.4$  or  $\pm 23^\circ$  (positive deflection for negative muons, negative deflection for positive muons). The distributions of residuals in the angle  $\varphi$  (difference between  $\varphi_{L1}^{\text{rec}}$  returned by the L1 trigger and the generated value of  $\varphi^{\text{sim}}$ ) are shown in Fig. 4.3, for positive and negative muons separately. The  $\varphi$  resolution distribution is shown again in Fig. 4.4 after applying a fixed correction  $\Delta\varphi$  of  $+0.4$  rad for positive muons and of  $-0.4$  rad for negative muons. While the distribution is

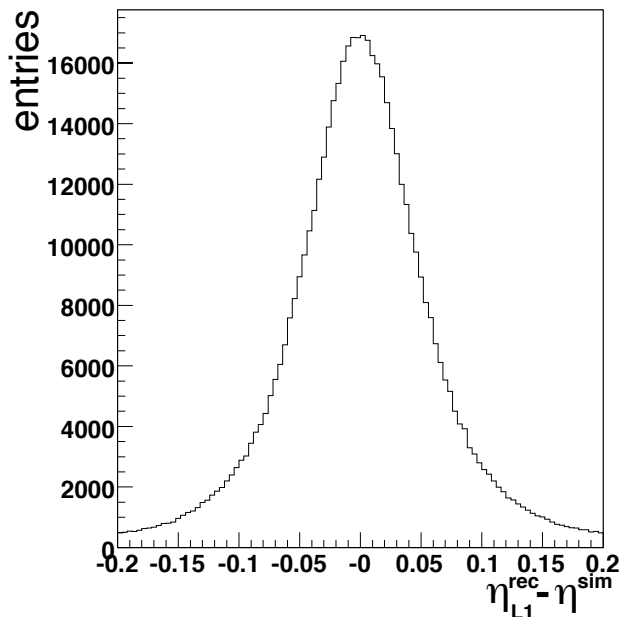


Figure 4.1: Distribution of  $\eta^{rec} - \eta^{sim}$  for Level-1 muon trigger candidates.

obviously far from Gaussian, the angle  $\varphi$  of most of the muons now lie in a window of  $\pm 0.5$  rad around the generated value. This distribution also features significant tails, containing those muons with incorrect charge assignment for which the  $\varphi$  correction pulls the measured value further away from the generated value.

## 4.2.2 Level-2 selection using displaced $J/\psi$ candidates

### 4.2.2.1 Primary vertex reconstruction

The first step in the  $J/\psi$  selection is the reconstruction of the interaction vertex. Primary vertex reconstruction and identification is performed with an algorithm which uses tracks reconstructed only from hits in the pixel detector (*Divisive Primary Vertex Finder* algorithm [52]). Using only hits from the pixel detector saves time in the reconstruction, which is important on trigger level. Due to pileup events, several primary vertices can be found in each event. The efficiency that one of the reconstructed vertices in the event corresponds to the simulated  $B_S$  vertex is given by:

$$\epsilon = \frac{N_{PV}}{N_{L1}}, \quad (4.8)$$

where  $N_{L1}$  is the number of events which have passed the Level-1 trigger, and  $N_{PV}$  is the number of events where the correct primary vertex is reconstructed. It is assumed that the correct primary vertex is reconstructed if at least one primary vertex

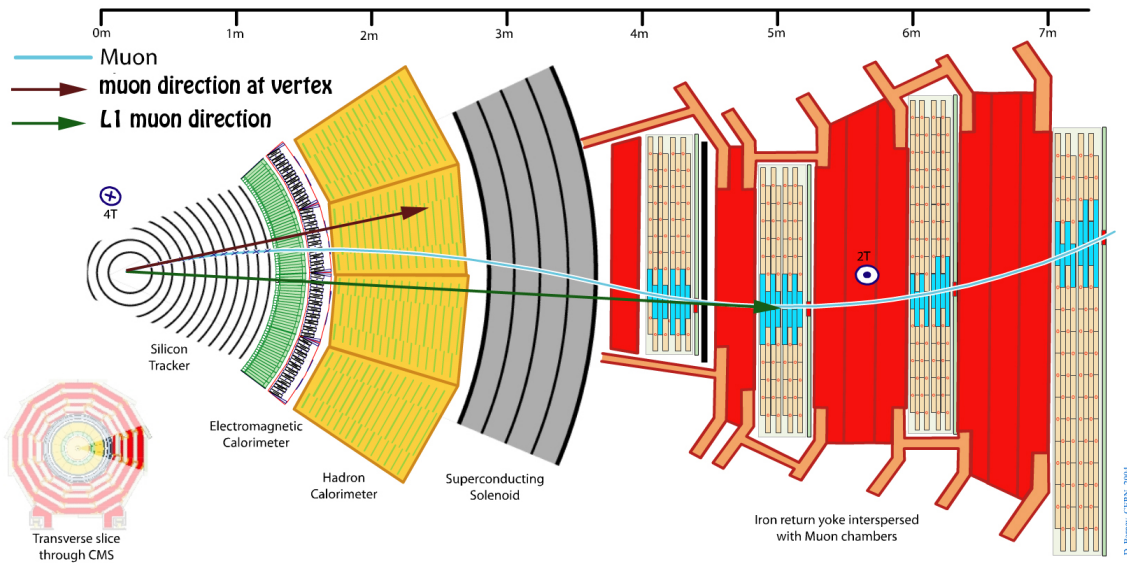


**Figure 4.2:** A transverse slice of the CMS detector with a negatively charged muon passing through it (blue curve). The muon direction at production vertex is illustrated by the red arrow whereas the direction measured by the second muon station (Level-1 direction) is illustrated by the green arrow.

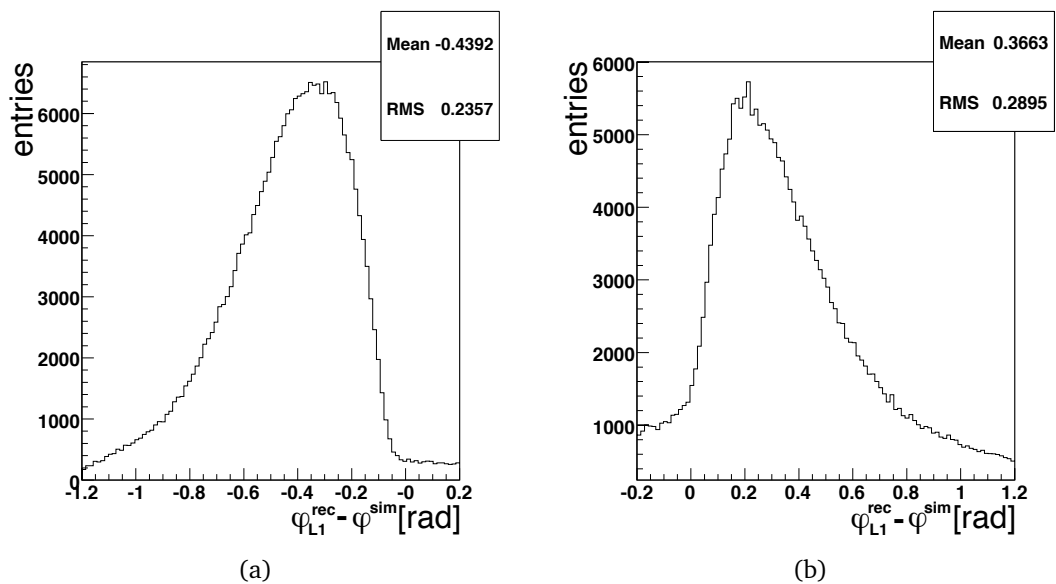


**Figure 4.3:** Distribution of  $\varphi_{L1}^{rec} - \varphi_{L1}^{sim}$  for Level-1 muon trigger candidates, for positively charged muons (a) and negatively charged muons (b).

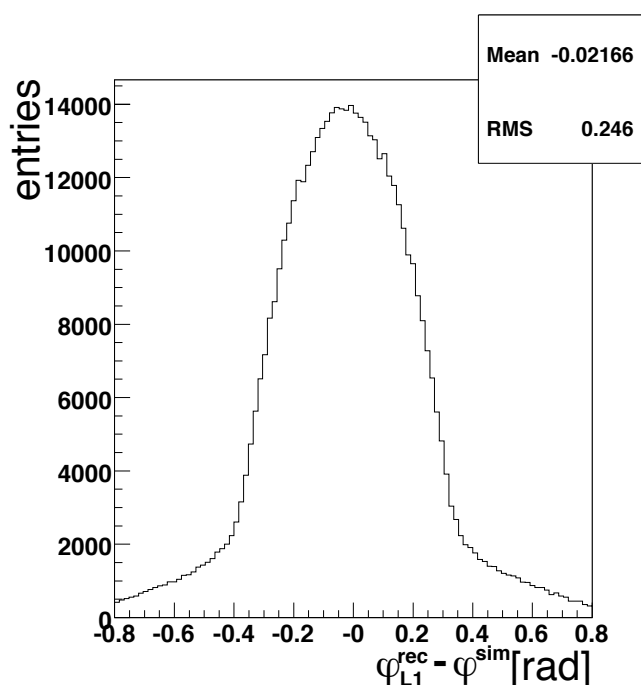


**Figure 4.4:**  $\varphi_{L1}^{rec} - \varphi_{L1}^{sim}$  distribution for Level-1 muon trigger candidates, after applying a correction of  $+0.4$  rad for positive muons and of  $-0.4$  rad for negative muons to take into account the deflection in the magnetic field.

is reconstructed within  $500 \mu\text{m}$  in  $z$  from the simulated one. An efficiency of 0.988 is obtained. The distribution of residuals of the estimated  $z$  position of the closest primary vertex is shown in Fig. 4.5 and the width of the core of the distribution is  $\sigma_{z_{pV}} = 67 \mu\text{m}$ . This is already a very good resolution taking into account that only hits in the pixel detector were used.

For the  $(x, y)$  coordinates of the primary vertex, the nominal position from the beam spot is taken, since the uncertainty on the position of the LHC beam spot ( $\sigma = 16.7 \mu\text{m}$ ) is smaller than what may be obtained from reconstructed tracks (due to the fact that the beam spot is calculated from many events, not just one).

As mentioned before, the pixel vertexing algorithm reconstructs the signal interaction vertex as well as pile-up interaction vertices. In most other physics analysis in CMS, the identification of the signal primary vertex is performed by ordering primary vertices by the sum of  $p_T^2$  of the tracks associated to the vertex and then using the one with the highest sum of  $p_T^2$ . However, for  $B_s$  events this criterion is not well suited since many of the tracks have relatively low  $p_T$  and are produced in secondary vertices and might thus not be taken into account for the primary vertex. In fact, the efficiency for finding the correct primary vertex in  $B_s \rightarrow J/\psi \phi$  events is lowered from 0.988 to 0.796 if only the vertex with the highest sum of  $p_T^2$  is selected. In order to avoid this efficiency loss, the three vertex candidates with the highest sum of  $p_T^2$  in the event are retained for the following analysis, with an efficiency of 0.969. The correct primary



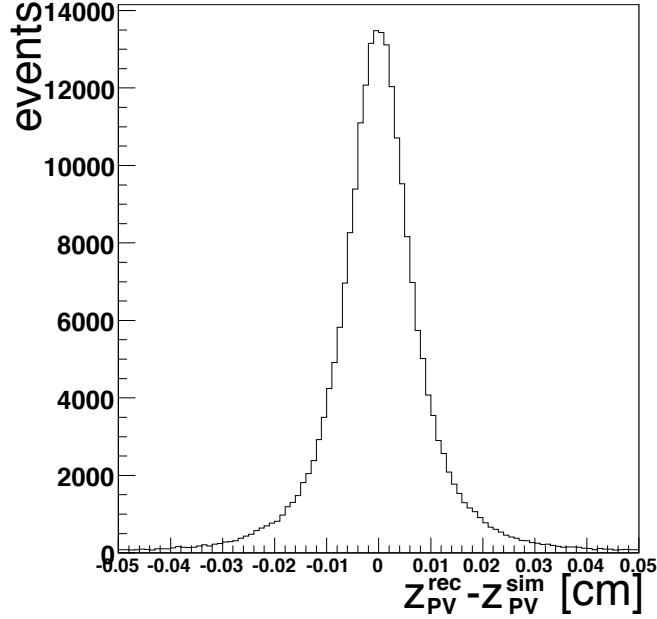


**Figure 4.5:** Distribution of  $z^{rec} - z^{sim}$  for the primary vertex, reconstructed with the Divisive Primary Vertex Finder method. For each simulated interaction vertex, the closest reconstructed Primary Vertex is used.

vertex is then selected after the  $J/\psi$  reconstruction.

#### 4.2.2.2 Muon track reconstruction

At this stage, muons are reconstructed in the tracker only. The only input from the muon system is the direction of the muons triggered by the Level-1 trigger. To ensure a fast reconstruction which is necessary in the trigger, tracks are reconstructed only in regions around the Level-1 muon directions. The track reconstruction starts from regions around each of the three primary vertices (as shown in Fig. 4.6). This region expands  $\pm 1$  cm in  $z$  and  $r$  around each primary vertex. These fairly loose constraints are necessary to reconstruct efficiently tracks from secondary vertices arising from  $B$  decays.

The direction of the Level-1 muon candidate is used to define a rectangular region in the  $(\eta, \varphi)$  space (Fig. 4.6), with the  $\varphi$  coordinate corrected by 0.4 rad as discussed in Sec. 4.2.1. The width of the region of interest around the Level-1 direction is  $|\Delta\eta| < 0.15$ ,  $|\Delta\varphi| < 0.5$ . Regional track reconstruction is carried out in these regions as detailed in [23, Section 6.4.2.1], but in order to reduce reconstruction time, the maximum number of trajectory candidates to propagate at each step is limited to 3, and propagation is stopped after 5 hits have been added to the track.

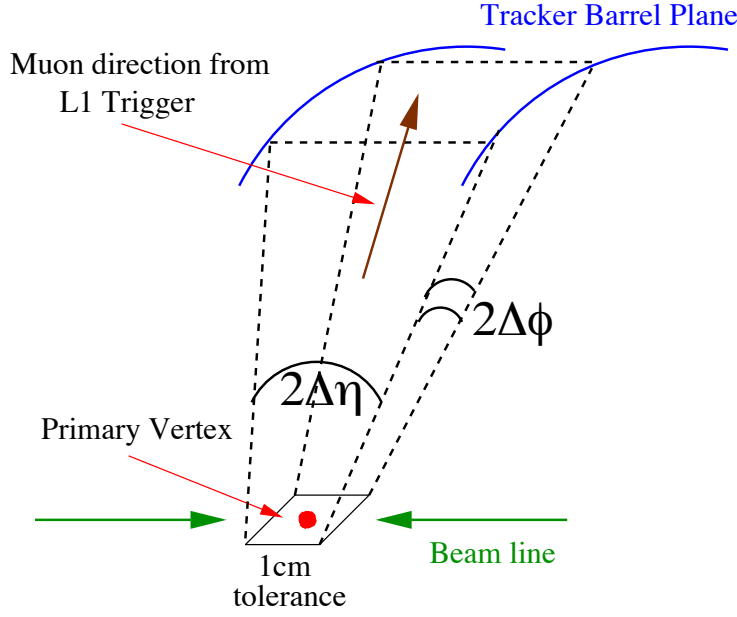


Figure 4.6: Rectangular  $\eta - \phi$  region for local track reconstruction [53].

#### 4.2.2.3 $J/\psi$ reconstruction and selection

After assigning the muon mass to the reconstructed tracks, the invariant mass of the pair is calculated. The mass resolution for the  $J/\psi$  candidates depends on the number of hits used in track reconstruction; a resolution of  $\sigma = 51 \text{ MeV}/c^2$  is obtained with 5 hits per track. The mass distribution is shown in Fig. 4.7, the combinatorial background arises from signal events in which one (or more) reconstructed track is not matched to the corresponding generated particle of the  $B_s$  decay. The width of the distribution is only due to the reconstruction, since the natural width of the  $J/\psi$  is  $93.2 \pm 2.1 \text{ keV}$  at a mass of  $3.096 \text{ GeV}/c^2$ .

To obtain optimal signal efficiency whilst minimising the background, a  $J/\psi$  candidate is accepted if it passes the following cuts:

$$\begin{aligned} p_T(\mu) &> \begin{cases} 2.5 \text{ GeV}/c & \text{for } |\eta| < 1.2, \\ 2.0 \text{ GeV}/c & \text{for } 1.2 \leq |\eta| < 2.5, \end{cases} \\ p_T(J/\psi) &> 4.0 \text{ GeV}/c, \\ |\Delta m_{J/\psi}| &< 150 \text{ MeV}/c^2, \end{aligned}$$

where  $\Delta m_{J/\psi}$  denotes the difference between the invariant mass of the reconstructed  $J/\psi$  candidate and the known mass of the  $J/\psi$  ( $3097 \text{ MeV}/c^2$ ). A  $p_T$  cut lower than the Level-1 cut is imposed on the muons, especially in the endcap region, in order to try to recover muons passing the Level-1 trigger thanks to an overestimated Level-1  $p_T$ .

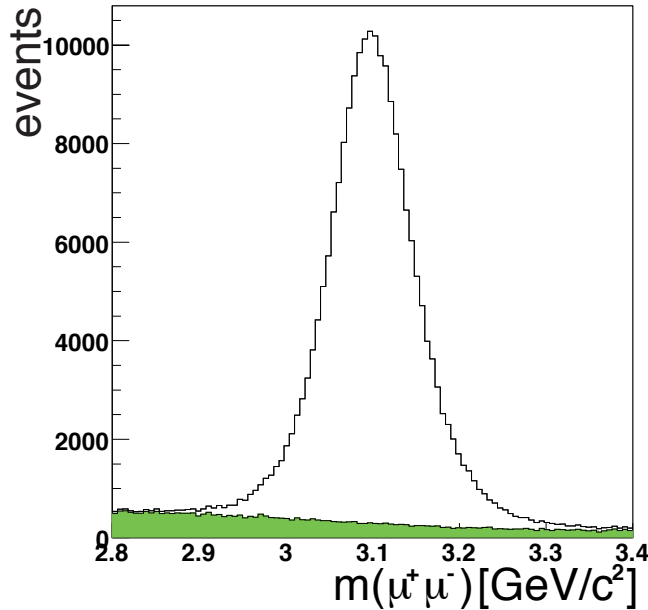


**Figure 4.7:** Mass distribution for the  $J/\psi$  with the Level-2 reconstruction. The background is combinatorial in signal events (green).

The efficiency for Level-2  $J/\psi$  reconstruction in signal events (calculated with respect to the number of events triggered at Level-1 with the request of opposite muon charge) is 0.88.

After performing  $J/\psi$  reconstruction, it is then possible to correctly identify the signal primary vertex as the one from which the two muon tracks originate.

#### 4.2.2.4 Prompt $J/\psi$ background rejection

The prompt  $J/\psi$  production represents a dominant contribution to the Level-1 di-muon trigger rate, as shown in Tab. 4.4: out of 900 Hz of total rate, 172 Hz are estimated to come from  $J/\psi$  decays. Thanks to their relatively long lifetime of  $\approx 1.5$  ps,  $B$  mesons are typically able to travel a few millimetres before decaying. This gives a powerful tool to discriminate between prompt  $J/\psi$  and  $J/\psi$  from  $B$  meson decays. In order to reject prompt  $J/\psi$  events the decay vertex of the  $J/\psi$  resonance is reconstructed and its compatibility with the beam axis is evaluated. A Kalman vertex fit [54] is performed on the two muon tracks, and events are retained where the reduced  $\chi^2$  per degree of freedom of the fit satisfies  $\chi^2/\text{ndof} < 10$ . This already rejects events in which the two muons used for the  $J/\psi$  candidate do not originate from the same vertex.

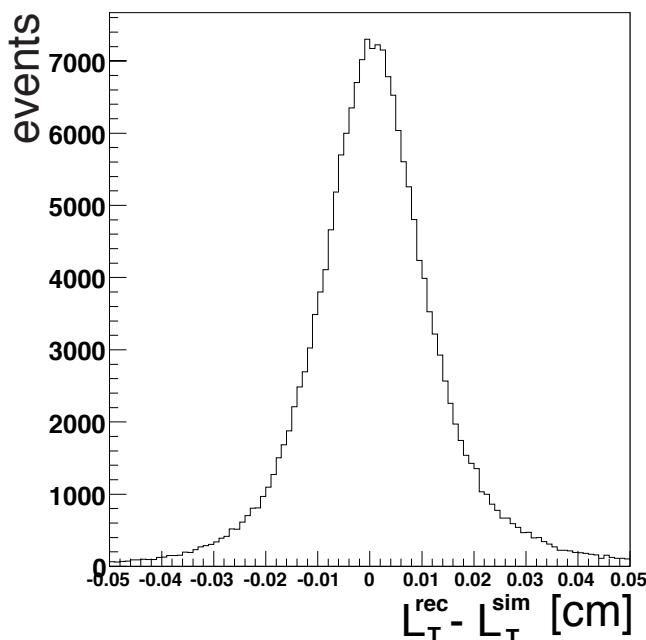


**Figure 4.8:** Residual distribution of the transverse decay length for the  $J/\psi$  candidates with the Level-2 reconstruction.

The main variable used to discriminate between signal and background is the transverse decay length  $L_{xy}$ , which is the distance between the reconstructed secondary vertex and the beam axis in the plane transverse to the beam axis. The distribution of residuals of the transverse decay length are shown in Fig. 4.8. The resolution, obtained from a Gaussian fitted to the core of the residual is  $\sigma = 100 \mu\text{m}$ , which is good enough to resolve  $B$ -meson decays and thus to reject background from prompt decays.

Distributions of the transverse decay length for signal events and for background events are illustrated in Fig. 4.9(a). One can clearly see the difference between the distribution of the prompt  $J/\psi$  events and the  $B$ -meson decays. In order to estimate the compatibility of the decay vertex with the primary vertex, it is convenient to define the significance of the transverse decay length, which is the transverse decay length itself divided by its error ( $L_{xy}/\sigma_{L_{xy}}$ ). Distributions for signal and background are reported in Fig. 4.9(b). A low background rate from direct  $J/\psi$  below 3 Hz is obtained with a threshold of  $L_{xy}/\sigma_{L_{xy}} > 3$ , which is therefore chosen as the working point for the High-Level Trigger selection.

Additional background rejection may be obtained requiring that the direction of the momentum of the  $J/\psi$  candidate in the transverse plane is approximately parallel to the direction of the transverse decay length, since  $J/\psi$  mesons produced in the decays of relatively high momentum  $B_s$  are collimated around the  $B_s$  direction by the relativistic boost. The opening angle  $\Delta\alpha$  is thus defined as the angle between

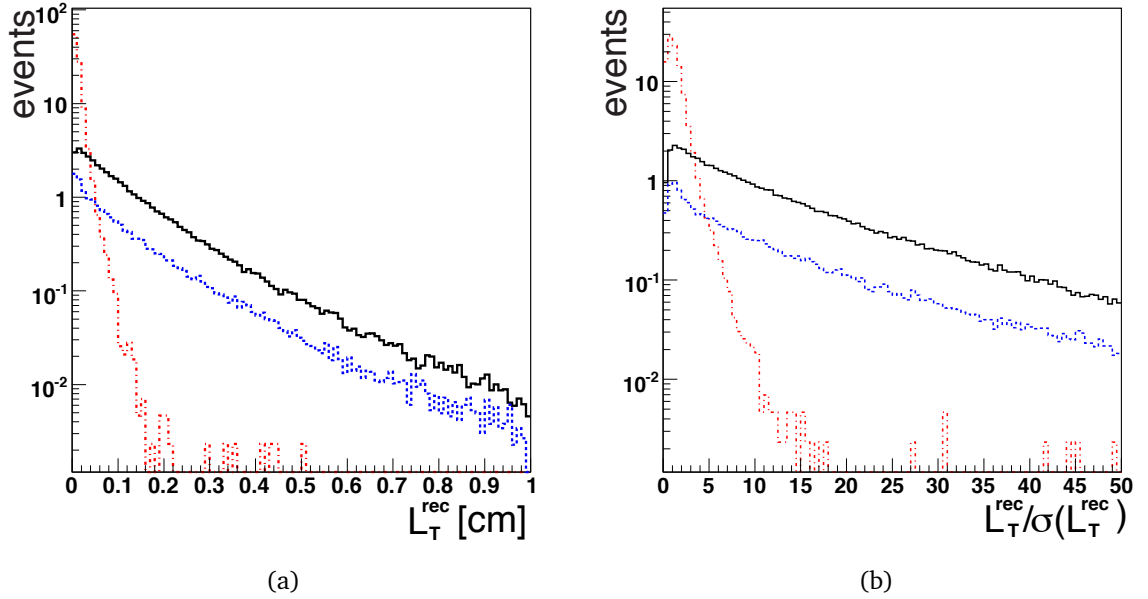


**Figure 4.9:** Distribution of the transverse decay length  $L_{xy}$  (a) and of its significance  $L_{xy}/\sigma_{L_{xy}}$  (b) for signal events (in black continuous line), direct  $J/\psi$  background (red dashed-dotted line) and for  $b \rightarrow J/\psi$  background (blue dashed line) at the Level-2 trigger. Signal events are rescaled by a factor  $10^3$ .

the transverse momentum vector and the transverse decay length vector of the  $J/\psi$  candidate. The distribution of this variable after applying the decay length selection is shown in Fig. 4.10 for signal and direct  $J/\psi$  background events. For signal events, the direction of the  $J/\psi$  is almost parallel to the vector between the primary vertex and the decay vertex. So the value for  $\cos(\Delta\alpha)$  is close to 1. For background events, where no true secondary vertex is present, it is equally probable that the false secondary vertex is reconstructed in opposite or in the same direction of the momentum vector. This results in the peaks at 1 and  $-1$ . With a cut at  $\cos(\Delta\alpha) > 0.9$ , corresponding to an angle of less than 0.45 mrad, it is possible to keep almost all signal events while discarding these background events.

#### 4.2.2.5 Trigger rates at Level-2

Tab. 4.5 summarizes the performance of the Level-2 trigger selection:  $b \rightarrow J/\psi X$  events are now the dominant contribution to the trigger rate. This selection is therefore well suited for an inclusive selection of decays of  $B$  hadrons to  $J/\psi$ , which may be used for many different  $B$  Physics studies, including reconstruction of other exclusive decays in addition to  $B_s \rightarrow J/\psi \phi$ , or measurement of inclusive quantities such as the total  $b\bar{b}$  production cross section. The signal rate is still orders of magnitudes

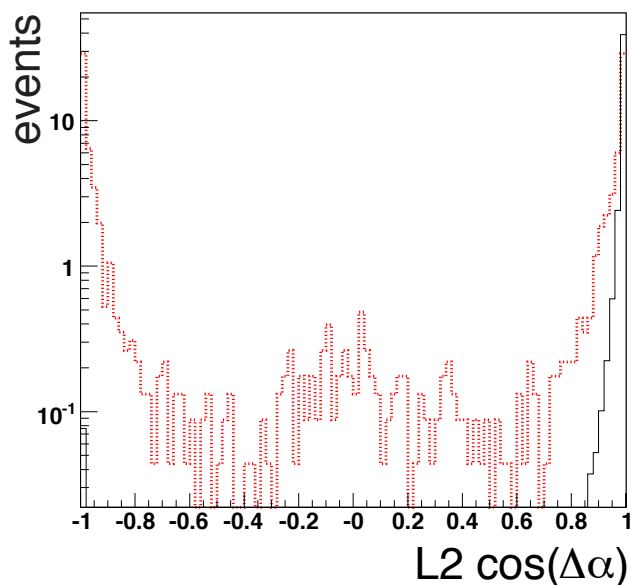


**Figure 4.10:** Distribution of  $\cos(\Delta\alpha)$  for signal (in black continuous line) and direct  $J/\psi$  (in red dashed-dotted line) events, after the application of the decay length cut  $L_{xy}/\sigma_{L_{xy}} > 3$ .

smaller than the background, making a further reduction in rate possible, as shown in the next section.

### 4.2.3 Level-3 selection with full $B_s \rightarrow J/\psi \phi$ reconstruction

The total background rate at Level-2 is within 15 Hz, but is still too high to be recorded on tape for offline analysis. An additional reduction of the trigger rate may then be achieved by performing a Level-3 reconstruction of the full decay chain.

First, the two kaons originating from the  $\phi$  need to be reconstructed. For this, the constraints on the region in  $\eta - \varphi$  space have to be much weaker than the constraints imposed at Level-2 since the direction of the kaons is not measured by the muon

**Table 4.5:** Efficiency  $\epsilon$  (defined with respect to the number of generated events) and rate  $R$  for signal and backgrounds of the Level-2  $J/\psi$  trigger selection. The errors are statistical. Systematic uncertainties will be discussed in Section 4.4.6.

sample	$B_s \rightarrow J/\psi \phi$	direct $J/\psi$	A: $b \rightarrow J/\psi X$	B: $b \rightarrow J/\psi X$	$B_d \rightarrow J/\psi K^*$
$\sigma$ (nb)	0.074	176	27.9	3.20	0.366
L2 $\epsilon$	0.2869(7)	$0.65(2) \cdot 10^{-2}$	0.2127(11)	0.2191(11)	0.3028(12)
L2 R (Hz)	0.042463(9)	2.287(7)	12.21(6)	1.4064(7)	0.2434(1)

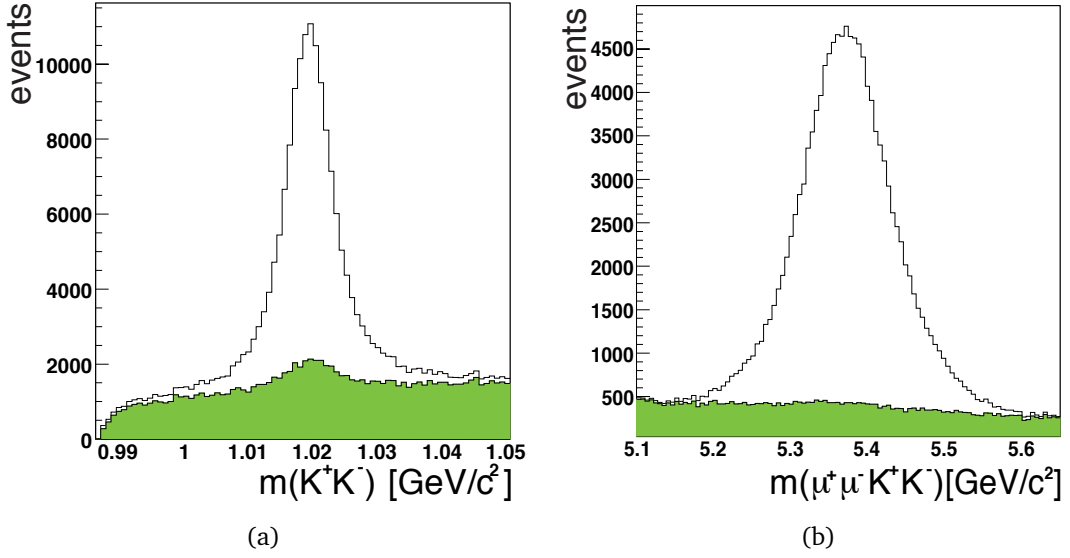


**Figure 4.11:** Invariant mass distribution of  $\phi$  (a) and  $B_s$  (b) candidates with the Level-3 reconstruction. The background is combinatorial in signal events (green).

system. Tracks are reconstructed in a region of ( $|\Delta\eta| < 0.9$ ,  $|\Delta\varphi| < 0.9$ ) around the momentum direction of each  $J/\psi$  candidate. The track propagation is performed in the same way as in the Level-2 reconstruction, using only 5 hits in the tracker.

All tracks with transverse momentum greater than 0.7 GeV/c in this tracking region are kept. In addition, the tracks should not pass the primary vertex identified as the one from which the  $J/\psi$  mother originates further than 1 cm in  $z$  and  $r$ .

Tracks selected in this way are assigned the  $K$  mass (494 MeV/c<sup>2</sup>).  $\phi$  candidates are created from all possible combination of positive and negative tracks. Now  $B_s$  candidates can be created combining the  $\phi$  candidates with the  $J/\psi$  candidates reconstructed in Level-2. To retain a high signal fraction while rejecting most of the background, the following cuts are applied to  $\phi$  and  $B_s$  candidates:

$$\begin{aligned} p_T(\phi) &> 1.0 \text{ GeV}/c \\ p_T(B_s) &> 5.0 \text{ GeV}/c . \end{aligned}$$

Reconstruction and selection efficiency for the full decay chain at Level-3 (calculated with respect to the number of events triggered at Level-2) is 0.86 for signal events. The invariant mass distributions of the  $\phi$  and  $B_s$  candidates are shown in Fig. 4.11. The width of the mass distributions of the  $\phi$  is  $\sigma_\phi = 4.4 \text{ MeV}/c^2$  and the one of the  $B_s$  is  $\sigma_{B_s} = 65 \text{ MeV}/c^2$ . While the  $B_s$  mass width arises purely from the reconstruction uncertainties, the  $\phi$  width is already of the same order of magnitude as its natural width  $\Gamma_\phi = 4.26 \pm 0.04 \text{ MeV}/c^2$ .

sample	$B_s \rightarrow J/\psi \phi$	direct $J/\psi$	<b>A:</b> $b \rightarrow J/\psi X$	<b>B:</b> $b \rightarrow J/\psi X$	$B_d \rightarrow J/\psi K^*$
$\sigma$ (nb)	0.074	176	27.9	3.20	0.366
L3 $\epsilon$	0.2050(6)	$0.7(7) \cdot 10^{-5}$	$1.5(1) \cdot 10^{-3}$	$1.23(3) \cdot 10^{-2}$	$9.37(14) \cdot 10^{-3}$
L3 R (Hz)	0.03034(8)	0.002(2)	0.083(6)	0.0792(18)	0.0077(2)

**Table 4.6:** Efficiency  $\epsilon$  (defined with respect to the number of generated events) and trigger rate  $R$  for signal and backgrounds of the Level-3 selection. The errors are statistical. Systematic uncertainties will be discussed in Section 4.4.6.

Imposing that the reconstructed masses lie within a loose window around the known values it is then possible to reduce substantially the background rate but keeping almost full efficiency on the signal:

$$\begin{aligned} |\Delta m_\phi| &< 0.02 \text{ GeV}/c^2, \\ |\Delta m_{B_s}| &< 0.2 \text{ GeV}/c^2, \end{aligned}$$

where  $\Delta m_\phi$  ( $\Delta m_{B_s}$ ) denotes the difference between the invariant mass of the reconstructed  $\phi$  ( $B_s$ ) candidate and the known mass of the  $\phi$  ( $B_s$ ) ( $m_\phi = 1019 \text{ MeV}/c^2$ ,  $m_{B_s} = 5366 \text{ MeV}/c^2$ ). A Kalman vertex fit with the four tracks from all  $B_s$  candidates is performed. Only events containing at least one combination where the four tracks are compatible with a common vertex are retained, imposing that the  $\chi^2/\text{ndof}$  of the vertex fit is less than 10. Additionally, the previous vertex constraint on the transverse decay length  $L_{xy}/\sigma_{L_{xy}} > 3$  is imposed again on the refitted vertex. In this case, the  $B_s$  momentum vector and the vector between production and decay vertex are expected to be perfectly aligned, since the  $B_s$  travels in a straight line before decaying; therefore, a tighter selection on the pointing angle  $\cos(\Delta\alpha) > 0.95$  is also applied.

Tab. 4.6 shows the efficiencies and expected rates for the  $B_s \rightarrow J/\psi (\rightarrow \mu^+ \mu^-) \phi (\rightarrow K^+ K^-)$  signal and the simulated backgrounds after the High Level Trigger selection.

### 4.3 Offline selection and reconstruction

The offline selection can be divided in three parts. First, a pre-selection of  $B_s \rightarrow J/\psi (\rightarrow \mu^+ \mu^-) \phi (\rightarrow K^+ K^-)$  decays is applied, similar to the HLT selection. The main difference is that the full detector is now used for the reconstruction and muons and track reconstruction is not restricted to certain regions anymore. Also, track reconstruction uses all hits available and is not stopped after 5 hits as in the HLT reconstruction. Muon criteria are tighter than in the trigger, requiring more hits in the muon chambers. After the pre-selection, a kinematic vertex fit is performed followed by tighter constraints on the reconstructed  $B_s$  candidate. This will be discussed in the following.



### 4.3.1 Pre-selection of $B_s \rightarrow J/\psi(\rightarrow \mu^+\mu^-)\phi(\rightarrow K^+K^-)$ decays

The primary vertex is reconstructed using the standard primary vertex finder in CMS [23, Section 6.6.4], which uses all fully reconstructed tracks in the complete tracker. The probability to find at least one primary vertex candidate in  $B_s$  signal events with the standard version of this algorithm is 0.92. However, only in 83% of the  $B_s$  events the reconstructed primary vertex is consistent with the simulated  $B_s$  vertex (i.e. the reconstructed primary vertex is within  $500 \mu\text{m}$  from the simulated vertex). In order to prevent this unnecessary loss of efficiency, the Primary Vertex is not used in this analysis, and all quantities of interest have been evaluated in the transverse plane and the beam-spot is used as  $x - y$  position.

Muons are reconstructed in CMS using the *global muon* reconstruction algorithm [23, Section 9.1.3], which tries to perform an outside-in extrapolation of the muon tracks obtained with a standalone reconstruction in the muon detector, combining them with the tracks reconstructed in the silicon tracker. Since the global muon reconstructor is more suited to the reconstruction of high- $p_T$  muons, it is not fully efficient for low- $p_T$  muons from  $J/\psi$  decays (the efficiency is around 88% per muon). Even when an event was triggered based on the reconstructed  $J/\psi$  on trigger level, these two muons are not necessarily reconstructed with the *global muon* reconstructor. The trigger requirements are much looser than the ones applied for *global muons* and low  $p_T$  muons might not reach the outermost muon stations as required in the offline reconstruction.

Thus a different approach was chosen to reconstruct the two muons from the  $J/\psi$ . All tracks are reconstructed with the standard track reconstruction algorithm [23, Section 6.5] in the inner tracker. A muon identification algorithm which uses information from the muon detector [23, Section 9.2.1.2] is applied to these tracks; the algorithm returns a compatibility score between 0 and 1 which depends on the number of hits or track segments in the outer muon detector compatible with an inside-out extrapolation of the tracker track. Tracks with a compatibility score greater than 0.1 are kept as muon candidates. In addition, all tracks reconstructed in the tracker are compared to the *global muons*; if the tracker tracks share more than half of their hits in the tracker with these *global muons*, the tracker tracks are also kept as muon candidates.

$J/\psi$  candidates are now formed from oppositely charged muons applying the following constraints:

$$\begin{aligned} p_T(\mu) &> \begin{cases} 3 \text{ GeV}/c & \text{for } |\eta| < 1.2, \\ 2.0 \text{ GeV}/c & \text{for } 1.2 \leq |\eta| < 2.5, \end{cases} \\ p_T(J/\psi) &> 4.0 \text{ GeV}/c, \\ |\Delta m_{J/\psi}| &< 120 \text{ MeV}/c^2. \end{aligned}$$

Again,  $\Delta m_{J/\psi}$  denotes the difference between the invariant mass of the reconstructed  $J/\psi$  candidate and the known mass of the  $J/\psi$  ( $3097 \pm 0.011 \text{ MeV}/c^2$ ).

To reconstruct the  $\phi$  meson, all tracks are reconstructed with standard track reconstruction. As CMS does not possess a particle identification system suitable for this measurement, all measured tracks have to be considered as possible kaon candidates, which adds a substantial combinatorial background. All oppositely charged tracks are considered as  $\phi$  candidates.  $B_s$  candidates are formed by combining the two muons from a  $J/\psi$  candidate with the two kaons from a  $\phi$  candidate. All possible combinations in an event are considered. In addition, the following constraints are applied:

$$\begin{aligned} p_T(K) &> 0.8 \text{ GeV}/c, \\ p_T(\phi) &> 1 \text{ GeV}/c, \\ |\Delta m_\phi| &< 20 \text{ MeV}/c^2, \\ p_T(B_s) &> 5 \text{ GeV}/c, \end{aligned}$$

where  $\Delta m_\phi$  denotes the difference between the invariant mass of the reconstructed  $\phi$  candidate and the known mass of the  $\phi$  ( $1019 \text{ MeV}/c^2$ ).

### 4.3.2 Kinematic vertex fit

For a precise reconstruction of the decay vertex, which is needed for the likelihood fit in Section 4.4, a kinematic vertex fit is used [55, 53]. Kinematic fitting is the application of constraints (e.g. mass, energy and momentum conservation) to improve the estimated parameters. Track parameters are improved by taking into account these constraints. The underlying mathematical approach in the kinematic fit is a  $\chi^2$  minimisation with Lagrange multipliers. The  $\chi^2$  used is given by the distance between the tracks and the reconstructed vertex. In this analysis the following constraints are applied in the fit:

- The four final state tracks are required to come from a common secondary decay vertex, since the decay time of the two intermediate states ( $J/\psi$  and  $\phi$ ) in the decay is negligible.
- The invariant mass of the muon pair is required to be equal to the mass of the  $J/\psi$  resonance ( $3097 \text{ MeV}/c^2$ ). This constraint can be applied since the experimental resolution on the  $J/\psi$  mass is much higher than its natural width  $\Gamma_{J/\psi} = 93.2 \pm 2.1 \text{ keV}/c^2$ . It is impossible to impose such a constraint on the kaon pair, since the width of the  $\phi$  ( $\Gamma_\phi = 4.26 \pm 0.04 \text{ MeV}/c^2$ ) is larger than the experimental resolution.

A detailed description of the kinematic fit applied to  $B_s \rightarrow J/\psi (\rightarrow \mu^+ \mu^-) \phi (\rightarrow K^+ K^-)$  events is outlined in [53, Chapter 3].

The invariant mass distribution of the  $B_s$  candidates after the kinematic fit is shown in Fig. 4.12(b). With this fit, the resolution of the reconstructed invariant mass of the  $B_s$  is improved from  $\sigma = 34 \text{ MeV}/c^2$  to  $\sigma = 14 \text{ MeV}/c^2$ .

### 4.3.3 Final $B_s \rightarrow J/\psi(\rightarrow \mu^+\mu^-)\phi(\rightarrow K^+K^-)$ selection

After the kinematic fit, tighter selection criteria are applied on the selected  $B_s$  candidates to suppress the background while keeping most of the signal. Apart from the improved resolution the kinematic fit returns a  $\chi^2$ -probability which allows to distinguish between the background and the signal. In case of background this probability is close to 0 while for the signal it is almost flat (apart from the  $B_d \rightarrow J/\psi(\rightarrow \mu^+\mu^-)K^*(\rightarrow K^+\pi^-)$  background, since the four tracks also come from the same vertex). Thus the following cut was applied:

$$P(\chi^2) < 10^{-3}.$$

In addition a cut on the reconstructed  $\phi$  mass is applied (Fig. 4.12(a)):

$$|\Delta m_\phi| < 8 \text{ MeV}/c^2.$$

Furthermore, for signal events, the momentum vector of the reconstructed  $B_s$  should be aligned with the vector between primary and secondary vertex. The opening angle between these two vectors is called  $\Delta\alpha$  and the following cut is applied:

$$\cos(\Delta\alpha) > 0.98.$$

At this stage no cut on the invariant  $B_s$  mass is applied since the sidebands could be used in the likelihood analysis (Section 4.4). Only a small fraction of the remaining background events are directly under the  $B_s$  peak, and even a simple cut on the reconstructed  $B_s$  mass would reduce the number of background events by a significant factor (see Section 4.4.5). No cut on the decay length  $L_{xy}$  is imposed since a further disturbance of the proper decay time distributions should be avoided.

With this selection, a yield of 1090000 signal events can be expected within  $10 \text{ fb}^{-1}$  of data, with a background of 43'600 events. The efficiencies for the different criteria are given in Tab. 4.7 for the signal and the different background samples. Tab. 4.8 summarises the expected event yields for  $10 \text{ fb}^{-1}$  as well as the number of processed Monte Carlo events for the signal and backgrounds.

### 4.3.4 Proper decay time resolution

As we will see in Section 4.4, the proper decay time of the  $B_s$  is one of the most important ingredients to the likelihood fit. A precise measurement is of great importance to

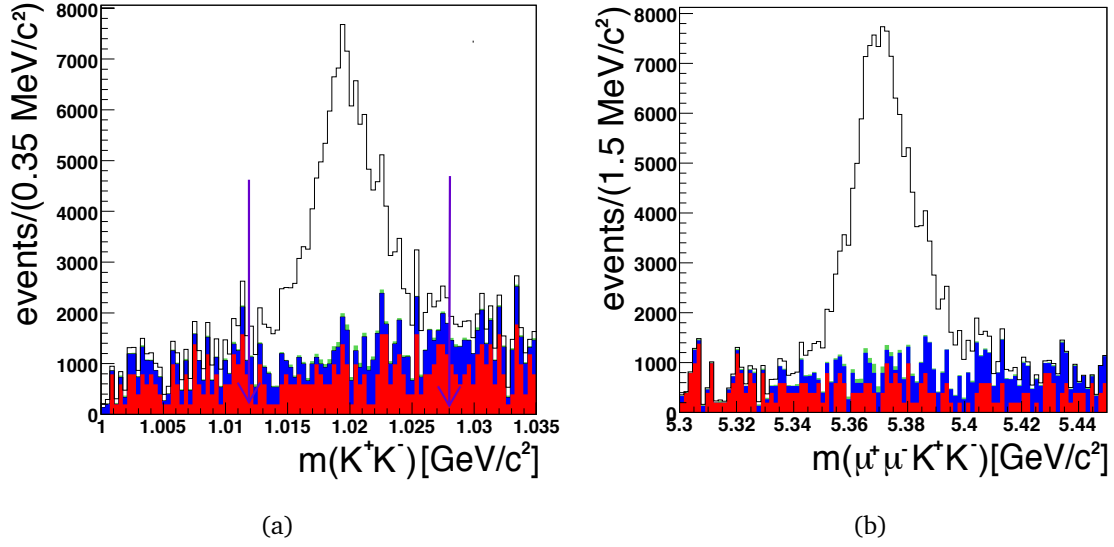


**Figure 4.12:** Invariant mass distribution of  $\phi$  (a) and  $B_s$  (b) candidates after cuts (except for the final  $\phi$  mass requirement) have been applied; the selection on the  $\phi$  mass is indicated. The background is from inclusive  $b \rightarrow J/\psi X$  (red), from  $B_d \rightarrow J/\psi K^*$  (blue), and from combinatorial in signal events (green). The histograms are stacked.

requirement	signal	background		
	$B_s \rightarrow J/\psi \phi$	$\mathbf{B}: b \rightarrow J/\psi X$	direct $J/\psi$	$B_d \rightarrow J/\psi K^*$
HLT selection	0.2050(6)	$1.23(3) \cdot 10^{-2}$	$0.7(7) \cdot 10^{-5}$	$9.37(14) \cdot 10^{-3}$
pre-selection	0.1789(5)	$5.85(19) \cdot 10^{-3}$	$0.7(7) \cdot 10^{-5}$	$6.36(11) \cdot 10^{-3}$
$P(\chi^2) < 10^{-3}$ req.	0.1658(5)	$2.82(14) \cdot 10^{-3}$	$0.7(7) \cdot 10^{-5}$	$5.03(10) \cdot 10^{-3}$
$\cos(\Delta\alpha) > 0.98$	0.1648(5)	$2.58(13) \cdot 10^{-3}$	–	$4.97(10) \cdot 10^{-3}$
$ \Delta m_\phi  < 8 \text{ MeV}/c^2$	0.1465(5)	$1.13(13) \cdot 10^{-3}$	–	$2.02(10) \cdot 10^{-3}$

**Table 4.7:** Offline selection efficiencies for the signal and background (defined with respect to the number of generated events) The quoted errors are statistical. Systematic uncertainties will be discussed in Section 4.4.6.

	$B_s \rightarrow J/\psi \phi$	$\mathbf{B}: b \rightarrow J/\psi X$	$B_d \rightarrow J/\psi K^*$
$\sigma \cdot Br$ (nb)	0.074	3.2	0.366
$\epsilon$ (%)	14.7	0.113	0.202
Events per $10 \text{ fb}^{-1}$	109'000	36'200	7'400
Events processed	507'888	154'000	486'000
Corresp. Lumi.	$6.8 \text{ fb}^{-1}$	$48 \text{ pb}^{-1}$	$1.3 \text{ fb}^{-1}$
Events selected	74'662	175	981

**Table 4.8:** Expected number of events and composition of the processed sample. The  $B_s$  sample includes combinatorial background.

resolve the different decay times of the light and heavy  $B_s$  meson. The proper decay time  $t$  of the  $B_s$  meson in its reference frame is related to the experimentally measured decay length by a Lorentz transformation:

$$t = \frac{t_{lab}}{\gamma} = \frac{L}{\beta c \cdot \gamma} = L \frac{m}{p}, \quad (4.9)$$

where the decay length  $L$  is the distance between the interaction and decay vertices in the laboratory frame,  $m$  is the mass of the  $B_s$  meson and  $p$  is the magnitude of its momentum. The Lorentzfactor  $\gamma$  is given by

$$\gamma = \frac{1}{\sqrt{1 - \beta^2}}, \quad (4.10)$$

$$\text{with } \beta = \frac{v}{c}, \quad (4.11)$$

where  $v$  is the velocity of the  $B_s$  meson.

It is also possible to determine the proper decay time from the projections of the decay length and momentum in the transverse plane, respectively  $L_T$  and  $p_T$ :

$$t = \frac{t_{lab}}{\gamma} = \frac{L_T}{\beta_T c \cdot \gamma} = L_T \frac{m}{p_T}, \quad (4.12)$$

$$\text{with } \beta_T = \frac{v_T}{c}, \quad (4.13)$$

where  $v_T$  is the transverse velocity.

The resolution for the transverse decay length is  $\sigma_{L_T} = 77 \mu\text{m}$  (Fig. 4.13(a)). The resolution of the proper decay time is then  $\sigma_t = 23 \mu\text{m}/c = 7.7 \cdot 10^{-14} \text{s}$  (Fig. 4.13(b)). The expected difference between the decay times of the heavy and light  $B_s$  of about  $30 \cdot 10^{-14} \text{s}$  is thus bigger than the resolution. Nevertheless, this resolution is not good enough to resolve the difference by a simple fit to the proper decay time distribution as shown in [53]. To extract the difference a likelihood fit on the time-dependent angular distribution as described in Chapter 1 needs to be performed. This likelihood fit is described in the following section.

## 4.4 The maximum likelihood fit

As already outlined in Chapter 1, the decay  $B_s \rightarrow J/\psi(\rightarrow \mu^+\mu^-)\phi(\rightarrow K^+K^-)$  provides a powerful tool to measure mixing parameters of the  $B_s$  system. In Section 1.2.3 the differential decay rate of the  $B_s \rightarrow J/\psi(\rightarrow \mu^+\mu^-)\phi(\rightarrow K^+K^-)$  was introduced as

$$\frac{d^4\Gamma(B_s(t))}{d\Theta dt} = f(\Theta, \alpha, t) = \sum_{i=1}^6 O_i(\alpha, t) \cdot g_i(\Theta), \quad (4.14)$$

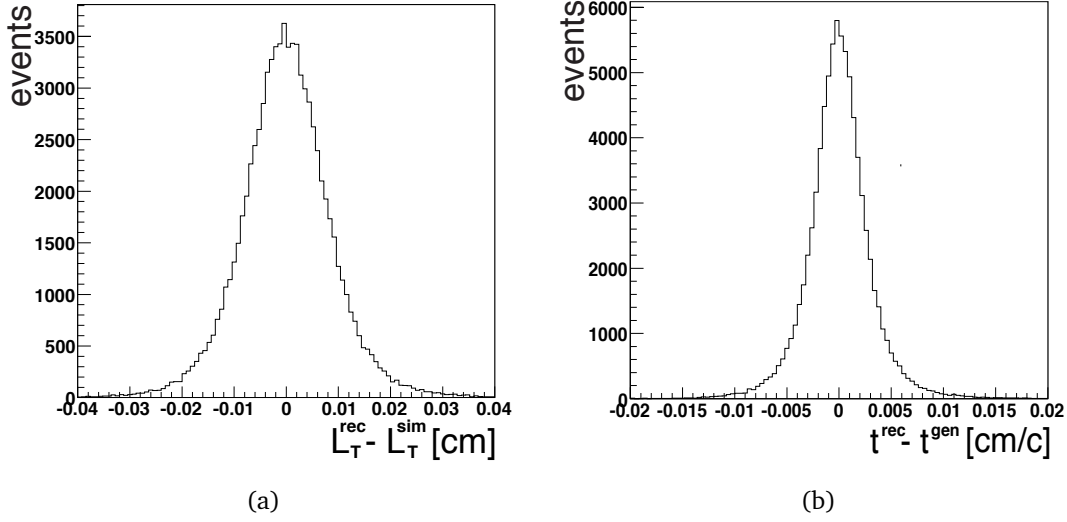


**Figure 4.13:** Residual distribution of the transverse decay length  $L_T$  (a) and associated proper decay time (b) for the  $B_s$  candidates with secondary vertices reconstructed with the kinematic fit.

where  $O_i$  are kinematics-independent observables and  $g_i$  the angular distributions (see Eq. 1.29 and 1.30). The set of physical parameters ( $\Gamma_L, \Gamma_H, |A_0|, |A_{\parallel}|, |A_{\perp}|, \delta_1, \delta_2, \phi_s$ ) is represented by  $\alpha$  and the angles which define the kinematics are generically denoted by  $\Theta = (\cos \theta, \varphi, \cos \psi)$ . The proper decay time is represented by  $t$ .

By observing the distribution of events in  $t$  and  $\Theta$  the physical parameters  $\alpha$  can be extracted. In our analysis we decided to use the method of *maximum likelihood* to estimate the parameters. For this the *likelihood function*

$$L(\alpha) = \prod_{i=1}^{N_{\text{events}}} \mathcal{P}(\Theta_i, \alpha, t_i) \quad (4.15)$$

needs to be maximized with respect to the set of parameters  $\alpha$ .  $\mathcal{P}(\Theta_i, \alpha, t_i)$  is the probability for a certain event  $i$  in which the angles  $\Theta_i$  and the proper time  $t_i$  were measured.  $N_{\text{events}}$  is the total number of reconstructed signal events. With perfect detector resolution, no distortion through the signal selection and no background, this probability would be  $\mathcal{P}(\Theta_i, \alpha, t_i) = f(\Theta, \alpha, t)$ . But although the selection criteria are kept as simple as possible, a distortion of the time dependent angular distributions is not avoidable. This distortion by the detector acceptance, trigger efficiency and the different selection criteria is taken into account by an efficiency term  $\epsilon(t, \Theta)$  determined from Monte Carlo simulation. In addition, a term describing the background (also determined from Monte Carlo simulation) has to be added. These steps, performed on events with full detector simulation, are detailed in Section 4.4.2 and 4.4.3. But first, in Section 4.4.1 the validation of the likelihood fit on a simplified event simulation will be presented.

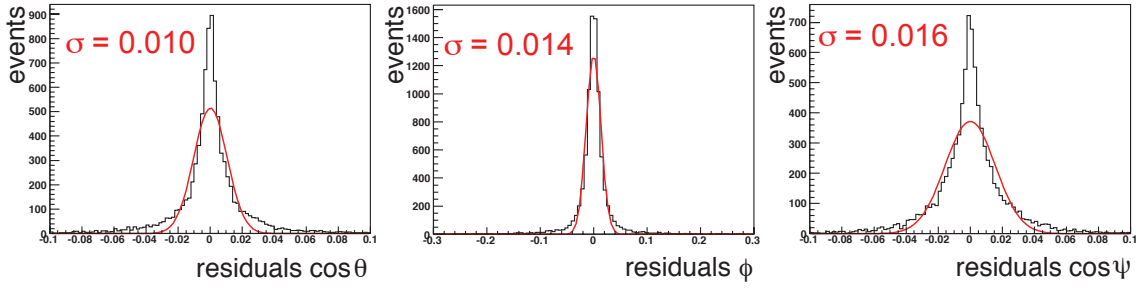


**Figure 4.14:** Residual distribution of the reconstructed angles ( $\cos\theta$ ,  $\phi$ ,  $\cos\psi$ ). The resolution is defined as the standard deviation of a Gaussian fitted to the distribution (red line).

#### 4.4.1 Validation of likelihood fit

Since the simulation of events using the full CMS detector simulation is very time consuming, the likelihood fit was first validated with a simplified Monte Carlo simulation, which also had the advantage of full control over the distributions generated. In this *toy Monte Carlo* the angles  $\Theta$  and the proper decay time  $t$  were generated according to Eq. 4.14. In addition the proper time  $t$  and the angles  $\Theta$  were smeared with Gaussian resolution functions. The standard deviations of these Gauss functions are taken to be equal to those measured with full detector simulation. As shown in Sec. 4.3.4 the resolution on the proper decay time is  $\sigma_t \approx 0.1$  ps. The residual distribution of the angles is shown in Fig. 4.14, where the resolution is obtained from a Gaussian fit. The Gaussian fit is obviously not optimal but sufficient for the purpose of the toy Monte Carlo simulation. Backgrounds were not simulated in the toy Monte Carlo.

The events generated with the toy Monte Carlo were used as input into a maximum likelihood fit based on the following probability density function

$$\mathcal{P} = f(\Theta, \alpha, t) \otimes G(t; 0, \sigma_t), \quad (4.16)$$

where  $f$  is folded ( $\otimes$ ) with  $G(t; 0, \sigma_t)$ , the Gaussian resolution function of the proper time with  $\sigma_t$  as a free parameter in the fit. The smearing of the angles was not taken into account in the fit since the uncertainties on the angles are very small and have a small impact on the likelihood fit results, as we will see in Section 4.4.1.2.

The maximum likelihood fit was performed fitting all 8 independent parameters simultaneously. The result for 100'000 events is given in Tab. 4.9. As can be seen, the relative width difference  $\Delta\Gamma_s/\bar{\Gamma}_s$  is determined with an uncertainty of 0.015. As expected, the relative uncertainty on the weak phase  $\phi_s$  is large, due to the smallness of  $\phi_s$ . The large uncertainties on  $\delta_1$  and  $\delta_2$  are due to the fact that they enter only in terms multiplied by  $\phi_s$ .

Parameter	Input value	Result	Stat.error	Rel.error
$ A_0(0) ^2$	0.57	0.5711	0.0023	0.4%
$ A_{  }(0) ^2$	0.217	0.2141	0.0036	1.7%
$ A_{\perp}(0) ^2$	0.213	0.2148	0.0030	1.4%
$\bar{\Gamma}_s$	0.712 ps <sup>-1</sup>	0.7132 ps <sup>-1</sup>	0.0032 ps <sup>-1</sup>	0.5%
$\Delta\Gamma_s$	0.142 ps <sup>-1</sup>	0.1338 ps <sup>-1</sup>	0.0100 ps <sup>-1</sup>	7.4%
$\Delta\Gamma_s/\bar{\Gamma}_s$	0.2	0.188	0.015	8.0%
$\delta_1$	$\pi$	2.93	0.61	
$\delta_2$	0	-0.09	0.63	
$\phi_s$	-0.04	-0.042	0.072	
$\sigma_t$	0.1 ps	0.1006 ps	0.0039 ps	3.9%

**Table 4.9:** Results of a likelihood fit on 100'000 events produced with the toy Monte Carlo, using the input values as in [9].  $|A_{\perp}(0)|^2$  and  $\Delta\Gamma_s/\bar{\Gamma}_s$  are not fitted but calculated from the other fitted parameters.

The consistency of the estimated quantities and their errors was cross checked. 50 samples with 100'000 events were produced and a fit was performed on each of these samples. The distribution of the estimated widths and relative width differences are shown in Fig. 4.15. The mean of the estimated  $\Delta\Gamma_s/\bar{\Gamma}_s$  is in very good agreement with the input value and the RMS of the distribution corresponds to the mean error of the fitted values.

The fit was also performed on samples with different numbers of events. As can be seen in Tab. 4.10, the error scales approximately with statistics, as expected.

#### 4.4.1.1 Test with different values for the input parameters

Fits were performed using different values for  $\Delta\Gamma_s/\bar{\Gamma}_s$  (Tab. 4.11) and  $\phi_s$  (Tab. 4.12) in the toy Monte Carlo to investigate the sensitivity of this method. For  $\Delta\Gamma_s/\bar{\Gamma}_s$ , the estimated values are always very close to the input value, and the estimated uncer-

**Table 4.10:** Results of the likelihood fit for different numbers of events. The input value for  $\Delta\Gamma_s/\bar{\Gamma}_s$  in the toy Monte Carlo was 0.2.

Events	Result for $\Delta\Gamma_s/\bar{\Gamma}_s$	Stat.error	Rel.error
10'000	0.163	0.046	28%
50'000	0.205	0.025	12%
100'000	0.188	0.015	8.0%
200'000	0.198	0.016	8.0%
500'000	0.208	0.009	4.3 %
1'000'000	0.203	0.0067	3.3%



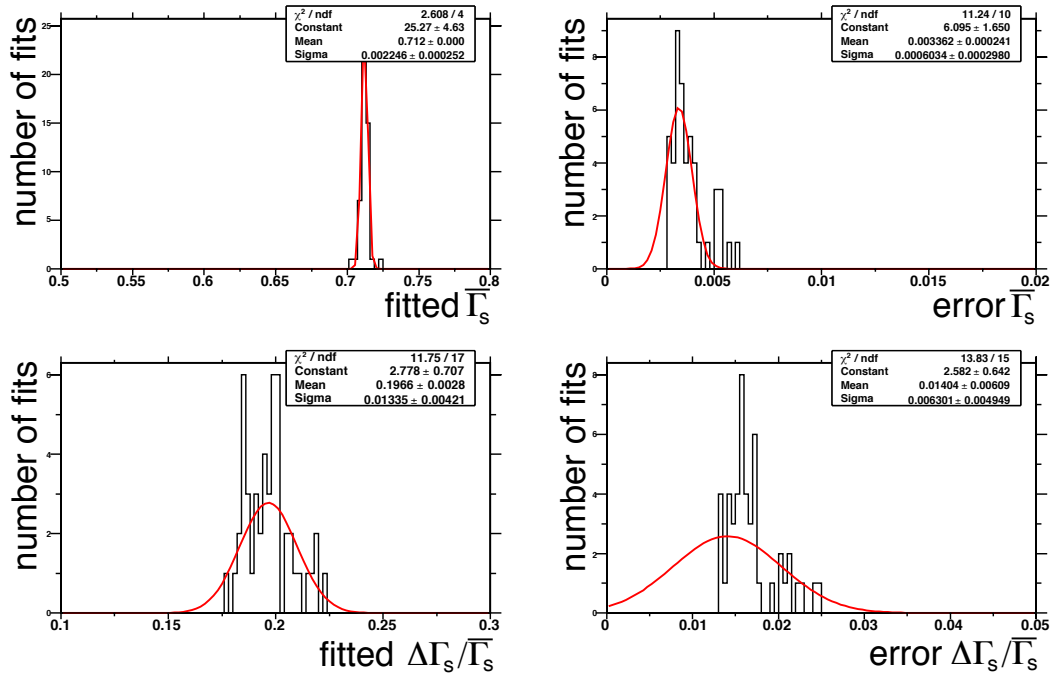


**Figure 4.15:** Distributions of the estimated quantities for likelihood fits on 50 independent samples of 100'000 events produced with the toy Monte Carlo. The upper plots show  $\bar{\Gamma}_s$  and the lower  $\Delta\Gamma_s/\bar{\Gamma}_s$ . Left plots show the estimated quantities, and right plots the estimated uncertainties. The red lined indicate Gaussian fits.

tainties are very stable. The phase can nevertheless not be estimated unless its value is very high.

#### 4.4.1.2 Influence of the resolution of the angular variables and the proper decay length

In order to estimate the influence of the measurement uncertainties of the angles, the toy Monte Carlo simulation was repeated without smearing and with a harsher smearing, where the resolution is taken to be two and five times larger than obtained

**Table 4.11:** The average results for likelihood fits on 50 samples of 100'000 events produced with the toy Monte Carlo with different values for  $\Delta\Gamma_s/\bar{\Gamma}_s$ .

Input value for $\Delta\Gamma_s/\bar{\Gamma}_s$	Result	Stat.error	Rel.error
0.0	0.003	0.016	
0.1	0.1	0.018	18%
0.2	0.197	0.016	8%
0.3	0.298	0.018	6%
0.4	0.396	0.017	4%
0.5	0.497	0.017	3.4%

Input value for $\phi_s$	Result	Stat.error	Rel.error
0.	-0.03	0.077	256%
0.04	-0.060	0.088	147%
0.1	-0.135	0.089	66%
0.15	-0.189	0.094	50%
0.2	0.25	0.11	44%

**Table 4.12:** *The average results for likelihood fits on 50 samples of 100'000 events produced with the toy Monte Carlo with different CP phases  $\phi_s$ .*

from the full simulation (denoted  $\sigma_{\text{Theta}}$ . The mean of the estimated  $\Delta\Gamma_s/\bar{\Gamma}_s$  from fits of 50 samples of 100'000 events is very close to the value found with the default smearing (Tab. 4.13). The error on  $\Delta\Gamma_s/\bar{\Gamma}_s$  does not increase by a larger smearing. This shows that the angular resolution is good and has almost no influence on the result. Thus it is correct not to include the angular smearing in the probability density function Eq. 4.16. The observed variation of 0.004 between the fit without smearing and the  $2\sigma_{\Theta}$  smearing will be added to the systematic uncertainty in Section 4.4.6 to account for the fact that the uncertainties on the angles are not taken into account in the fit. No influence is seen on the other parameters, such as  $\bar{\Gamma}_s$ ,  $|A_0^2|$ , ... .

A similar test is made with the proper decay length repeating the simulation without smearing and with a smearing, where the resolution is taken to be two times larger than in the default simulation (Tab. 4.14). As already said in Section 4.3.4, the uncertainty on the proper decay time  $t$  is almost as large as the expected width difference  $\Delta\Gamma_s$ . But its influence is still small since the proper decay time uncertainty  $\sigma_t$  is included in the likelihood fit through the convolution by the Gaussian resolution function in Eq. 4.16. The observed variation of 0.002 between the fit without smearing and the  $2\sigma_t$  smearing will be added to the systematic uncertainty. No influence is seen on the other parameters.

**Table 4.13:** *Mean of the estimated  $\Delta\Gamma_s/\bar{\Gamma}_s$  for different smearing of the angles  $\Theta$  on 50 samples of 100'000 events produced with the toy Monte Carlo. The input value for  $\Delta\Gamma_s/\bar{\Gamma}_s$  in the toy Monte Carlo was 0.2.*

Error on angles	Result for $\Delta\Gamma_s/\bar{\Gamma}_s$	Stat.error
no smearing	0.200	0.017
$1\sigma_{\Theta}$	0.197	0.016
$2\sigma_{\Theta}$	0.196	0.017
$5\sigma_{\Theta}$	0.192	0.017

Error on time	Result for $\Delta\Gamma_s/\bar{\Gamma}_s$	Stat.error
no smearing	0.197	0.018
$1\sigma_t$	0.197	0.016
$2\sigma_t$	0.195	0.017

**Table 4.14:** Mean of the estimated  $\Delta\Gamma_s/\bar{\Gamma}_s$  for different smearing of the proper decay time  $t$  on 50 samples of 100'000 events produced with the toy Monte Carlo. The input value for  $\Delta\Gamma_s/\bar{\Gamma}_s$  in the toy Monte Carlo was 0.2.

## 4.4.2 Signal efficiency from full detector simulation

From now on, all studies are performed on a sample with full detector simulation. As mentioned before, the time-dependent angular distributions used as input in the likelihood fit will be disturbed by the event reconstruction and selection. This distortion has to be taken into account by an efficiency function in the probability density function  $\mathcal{P}$ . It is assumed that the efficiency can be factorized in two functions, the first modelling the effects of the decay length requirements (see Section 4.2.2.4) and the second the distortion of the angular distribution,

$$\epsilon(t, \Theta) = \epsilon(t) \cdot \epsilon(\Theta). \quad (4.17)$$

The resulting probability function used in the fit is now:

$$\mathcal{P} = [\epsilon(t) \cdot \epsilon(\Theta) \cdot f(\Theta, \alpha, t)] \otimes G(t; 0, \sigma_t). \quad (4.18)$$

### 4.4.2.1 Angular efficiency

The angular efficiency  $\epsilon(\Theta)$  is a 3-dimensional efficiency which cannot be factorised due to the strong correlation of  $\cos\theta, \phi, \cos\psi$ . It is neither possible to obtain  $\epsilon(\Theta)$  from a 3-dimensional histogram in which the number of observed Monte Carlo events in each bin is divided by the number of events expected from the undisturbed function  $f(\Theta, \alpha, t)$ . This would require a very high number of simulated events with full detector simulation, something not possible in finite time. Thus it is necessary to parametrise the efficiency by a 3-dimensional angular function.

For this parametrisation an expansion of products of spherical harmonics [56] was used:

$$\epsilon(\Theta) = \sum_{LRM} T_{LRM}^\epsilon \cdot \mathcal{Y}_{LRM}(\Theta), \quad (4.19)$$

$$\text{with } \mathcal{Y}_{LRM}(\Theta) = \sqrt{2\pi} \cdot Y_{LM}(\theta, \varphi) \cdot Y_{RM}(\psi, 0), \quad (4.20)$$

where  $\mathcal{Y}_{LRM}$  are orthonormal basis functions and  $Y_{LM}$  are spherical harmonic functions. In principle,  $L$  and  $R$  run from 0 to infinity and the sum over  $M$  from  $-\min(L; R)$

to  $+\min(L;R)$ , but it has been found that the expansion can be limited to  $L, R \leq 8$ . These  $\mathcal{Y}_{LRM}$  functions describe the partial waves involved in a scalar  $\rightarrow$  vector decay [57].

The moments  $T_{LRM}^\epsilon$  of the efficiency can be determined by using the fact that  $\mathcal{Y}_{LRM}$  are orthonormal basis functions and thus satisfying

$$\int \mathcal{Y}_{LRM}(\Theta) \mathcal{Y}_{L'R'M'}^*(\Theta) d\Theta = \delta(L-L') \delta(R-R') \delta(M-M'). \quad (4.21)$$

Multiplying Eq. 4.19 with  $\mathcal{Y}_{L'R'M'}^*(\Theta)$  and integrating over  $\Theta$  yields

$$T_{LRM}^\epsilon = \int \epsilon(\Theta) \cdot \mathcal{Y}_{LRM}^*(\Theta) d\Theta. \quad (4.22)$$

The integral can be discretised into bins of size  $\Delta\Theta$ . The efficiency  $\epsilon(\Theta_j)$  in each bin  $j$  is then

$$\epsilon(\Theta_j) \cdot \Delta\Theta = \frac{N_j}{N_{\text{th}}}, \quad (4.23)$$

where  $N_j$  is the observed number of events in the bin  $j$  and  $N_{\text{th}}$  is the predicted number in the bin. Now Eq. 4.22 can be written as

$$T_{LRM}^\epsilon \approx \sum_{j=1}^{N_{\text{bins}}} \epsilon(\Theta_j) \cdot \mathcal{Y}_{LRM}^*(\Theta_j) \cdot \Delta\Theta \quad (4.24)$$

$$= \sum_{j=1}^{N_{\text{bins}}} \frac{N_j}{N_{\text{th}}} \cdot \mathcal{Y}_{LRM}^*(\Theta_j) \quad (4.25)$$

$$= \sum_{j=1}^{N_{\text{bins}}} \frac{N_j}{N_{\text{gen}} \cdot f(\Theta_j)} \cdot \mathcal{Y}_{LRM}^*(\Theta_j), \quad (4.26)$$

where  $f(\Theta_j)$  is the expected time-integrated angular distribution (Eq. 1.28) and  $N_{\text{gen}}$  is the total number of events generated. Finally, the number of bins can be chosen so large that maximally one event is contained in each bin. Thus only bins with one event contribute to the sum with weight 1. The moments  $T_{LRM}^\epsilon$  can then be determined directly from the reconstructed Monte Carlo events through the relation

$$T_{LRM}^\epsilon \approx \frac{1}{N_{\text{gen}}} \sum_{i=1}^{N_{\text{obs}}} \frac{1}{f(\Theta_i)} \mathcal{Y}_{LRM}^*(\Theta_i). \quad (4.27)$$

Fig. 4.16 shows the projections of measured angular distributions on each of the three angles  $\cos\theta$ ,  $\phi$ ,  $\cos\psi$  in black, where the projections for a certain angle are obtained by integrating over the other two angles. The red line represents the angular efficiency function  $\epsilon(\Theta)$  which was obtained with the method outlined above. The green line indicates the resulting probability density function  $\mathcal{P} = f(\Theta) \cdot \epsilon(\Theta)$ , which indeed agrees well with the observed Monte Carlo Data.

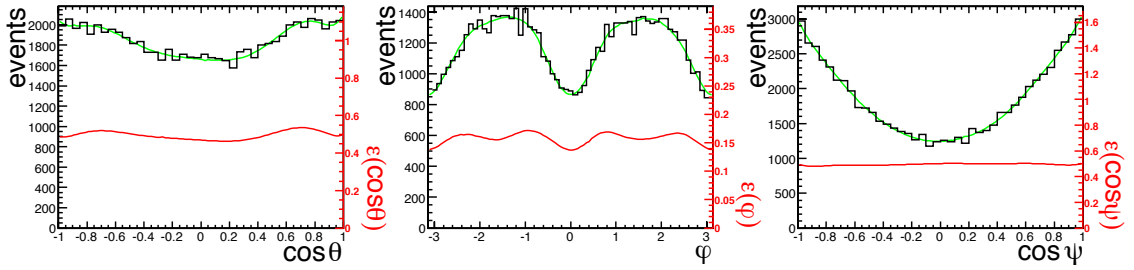


**Figure 4.16:** Observed angular distributions obtained from the full Monte Carlo simulation in black. Angular efficiency function  $\epsilon(\Theta)$  in red (normalised to one, with red axis on the right). The resulting angular probability density functions for the signal ( $f(\Theta) \cdot \epsilon(\Theta)$ ) is shown in green (scaled to the number of observed events). For each distribution, the functions are integrated over the two other angles.

#### 4.4.2.2 Efficiency of the proper decay time

The proper decay time distribution is disturbed by the decay length requirement on trigger level. Fig. 4.17 shows the distribution of  $\epsilon(t) = N_{\text{obs}}/N_{\text{gen}}$ . After the initial turn-on due to the decay length requirement and a stable plateau, a deficit of events can be observed. This decrease in efficiency is attributed to the restrictions imposed on the seeds by the tracking regions in the HLT, which cause an additional track reconstruction inefficiency for displaced tracks such as those originating from  $B$  decays. The tolerance of 1 cm in both the transverse and the longitudinal direction imposed on the tracking regions in the HLT (see Section 4.2.2.2) results in an implicit cut on the impact parameters. Further studies are needed to find solutions to alleviate this inefficiency. Without corrections, the main effect of this inefficiency would be to lower the estimated lifetime of the longer-lived eigenstate  $B_s^H$ .

The different features in this distribution cannot easily be described by a simple function. We have thus chosen two sigmoidal functions combined with a quadratic function

$$\epsilon(t) = \begin{cases} c \cdot \left(1 + \tanh\left(\frac{t-t_0}{\Delta t_1}\right)\right) & t < t_0 \\ (a \cdot t^2 + b \cdot t + c) \cdot \left(1 + \tanh\left(\frac{t-t_0}{\Delta t_2}\right)\right) & t > t_0 \end{cases} . \quad (4.28)$$

The parameters  $(a, b, c, t_0, \Delta t_1, \Delta t_2)$  are found by fitting this function to the distribution Fig. 4.17 obtained by the Monte Carlo simulation. The absolute normalisation of  $\epsilon(t)$  is not important here, since the overall probability density function is normalised in the likelihood fit.

The best way to determine the efficiency from real data is by using a different  $B$  meson decay, e.g. the decay  $B_d \rightarrow J/\psi K^*$ , which is very similar to the studied  $B_s$  decay, and for which the lifetime has been measured with a high precision.

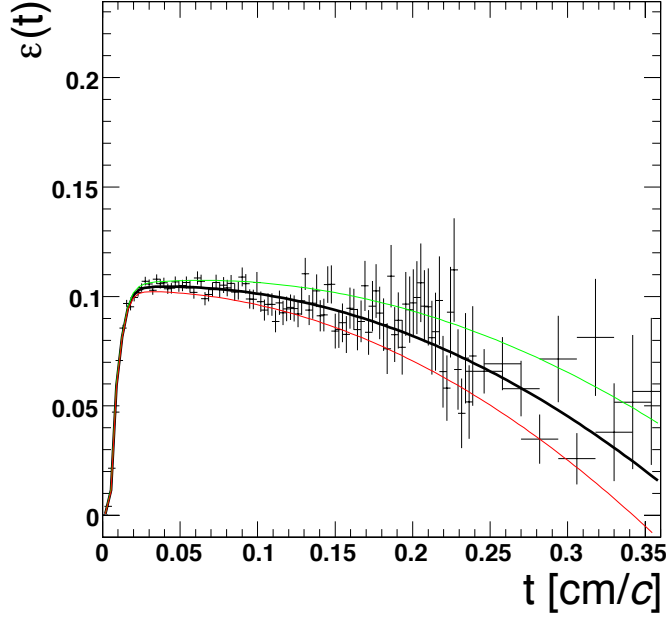


**Figure 4.17:** Distribution of the observed time-dependent efficiency  $\epsilon(t)$  (apart from a multiplicative normalisation factor) as a function of the proper decay length with fitted function (Eq. 4.28) and  $1\sigma$  uncertainties on the parameters of the fit function.

### 4.4.3 Background

Again, this part deals with events generated with full detector simulation. The probability density function  $\mathcal{P}$  in Eq. 4.18 is further disturbed by the background which was not fully rejected in the reconstruction and selection of the events. In principle this background would have to be taken care of by an additional term

$$\mathcal{P} = [(1 - b) \cdot \epsilon(\Theta, t) \cdot f(\Theta, \alpha, t) + b \cdot f_{BG}(\Theta, t)] \otimes G(t; 0, \sigma_t), \quad (4.29)$$

where  $b$  is the fraction of background and  $f_{BG}(\Theta, t)$  is the time-dependent angular distribution of the background.

Unfortunately, only 981  $B_d \rightarrow J/\psi(\rightarrow \mu^+\mu^-)K^*(\rightarrow K^+\pi^-)$  events and 175  $b \rightarrow J/\psi X$  events were left after reconstruction and selection. None of the prompt  $J/\psi$  events passed all selection criteria. Therefore, these background samples available were not large enough to estimate the distribution  $f_{BG}(\Theta, t)$ . Thus the likelihood fit was applied using a probability density function which assumes signal only (Eq. 4.18). The ensuing systematic error in the likelihood function was evaluated by comparing the result of the fit on a sample containing signal and background events with the result on a sample containing signal events only. This is discussed in Sections 4.4.5 and 4.4.6.

#### 4.4.3.1 Possible improvements in the background description

Although not applied in this analysis, a description of a possible way to estimate these distributions will be given here.

The background can be divided in two different types of distributions. The first type arises from misidentified  $B_d \rightarrow J/\psi(\rightarrow \mu^+\mu^-)K^*(\rightarrow K^+\pi^-)$  events, in which the pion has been taken to be a kaon. Since this decay is also a decay of a pseudo-scalar  $B$  meson into two vector mesons, its differential decay rate is of the same functional form (Eq. 1.28) [7, 8] as the decay of interest but with different parameters (see Tab. 4.2). The width difference of the two eigenstates of the  $B_d$  is assumed to be negligible, and no CP violation is present since the final state is flavour specific. The true time dependent angular distribution of the decay  $B_d \rightarrow J/\psi(\rightarrow \mu^+\mu^-)K^*(\rightarrow K^+\pi^-)$  is well known but cannot be used since the pion in the decay is reconstructed as a kaon. This misidentification leads to a distortion of the angular distributions and the decay time distribution of the  $B_d$  decay since the wrong mass is assigned to the pion leading to wrong boosts applied in the calculation of the angles (see Eq. 1.30) and in the calculation of the proper decay time (see Eq. 4.12).

Since the width difference in the  $B_d$  system is negligible, the distribution of the proper decay time can be separated from the angular distributions:

$$f_{B_d}(\Theta, t) = \epsilon(t) \cdot f_{B_d}(\Theta) \cdot e^{-\tau_{B_d} t}, \quad (4.30)$$

where  $\tau_{B_d}$  would be a free parameter in the likelihood fit. The well measured lifetime of the  $B_d$  cannot be used for  $\tau_{B_d}$  since the misidentified pion biases the proper decay time of the decay.

For the same argument as in Section 4.4.2.1, it is not possible to obtain the angular distribution  $f_{B_d}(\Theta)$  of the  $B_d$  background from a 3-dimensional histogram, since to many events would have to be generated to populate all bins in the histogram with sufficient statistics. Instead, the angular distribution of the  $B_d$  background should be described by a function. To model the angular distributions of the  $B_d \rightarrow J/\psi(\rightarrow \mu^+\mu^-)K^*(\rightarrow K^+\pi^-)$  background, the functions  $\mathcal{Y}_{LRM}(\Theta)$  (Eq. 4.20) are used again:

$$f_{B_d}(\Theta) = \sum_{LRM} T_{LRM}^{B_d} \cdot \mathcal{Y}_{LRM}(\Theta), \quad (4.31)$$

A similar derivation as in Section 4.4.2.1 leads to

$$T_{LRM}^{B_d} = \int f_{B_d}(\Theta) \cdot \mathcal{Y}_{LRM}^*(\Theta) d\Theta \quad (4.32)$$

$$\approx \frac{1}{N_{B_d}} \sum_{i=1}^{N_{B_d}} \mathcal{Y}_{LRM}^*(\Theta_i), \quad (4.33)$$

with the difference, that  $f_{B_d}(\Theta)$  is not an efficiency term but the full angular distribution of the  $B_d$  background. Here as well, the expansion would be done up to  $L, R \leq 8$ .

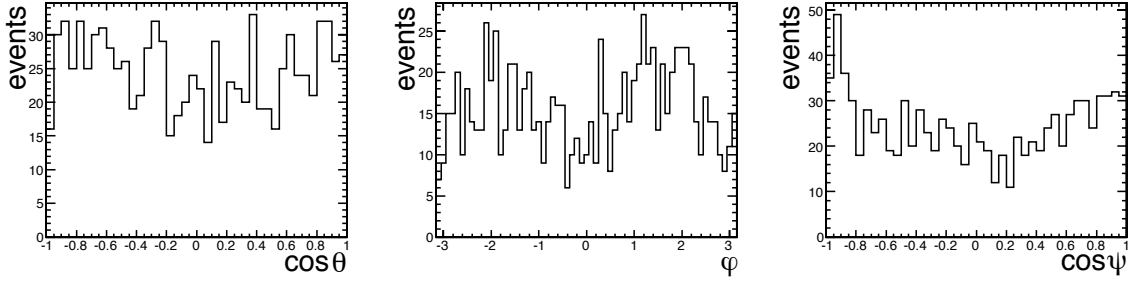


**Figure 4.18:** Angular distributions of the misidentified  $B_d \rightarrow J/\psi K^*$ .

These would be obtained by a Monte Carlo simulation, and could be cross-checked on real data by a fully reconstructed sample of well-identified  $B_d \rightarrow J/\psi K^*$  decays, misreconstructed as  $B_s$  candidates. However, the low number of events selected in our sample does not allow to compute this distribution reliably (Fig. 4.18). The corresponding distributions for the signal in Fig. 4.16 are much smoother due to better statistics. A different approach was thus taken as outlined in Section 4.4.5.

The other sources of background are assumed to have no angular dependence and will thus be modelled by a flat angular distribution normalised to one. The distribution of their proper decay time will be modelled by two exponential decays, the first,  $\tau_s$ , describing the short-lived prompt background and the second,  $\tau_l$ , misidentified long-lived heavy-flavour hadrons:

$$f_r(\Theta, t) = \epsilon(t) \cdot \left( \frac{b_s}{\tau_s} \cdot e^{-\tau_s t} + \frac{b_l}{\tau_l} \cdot e^{-\tau_l t} \right), \quad (4.34)$$

where  $b_s$  and  $b_l$  are the fractions of short-lived and long-lived backgrounds.

A better estimate of the signal and background fractions would be obtained by using the events in a wider 4-track invariant mass  $m(\mu^+ \mu^- K^+ K^-)$  region between 5.219 and 5.559  $\text{GeV}/c^2$ . Since the  $B_s$  signal events are mainly populated under the  $B_s$  mass peak, the fraction of background events could be estimated from outside this region. This would mean, that the 4-track invariant mass distributions for signal and backgrounds need to be included in the fit. The mass distribution of the  $B_s$  signal events could be modelled by a Gaussian  $G_s(m; m_{B_s}, \sigma_{B_s})$ , where  $m_{B_s}$  is the mass of the  $B_s$  meson and  $\sigma_{B_s}$  the standard deviation due to the reconstruction. The mass distribution of the misidentified  $B_d \rightarrow J/\psi K^*$  decays can also be modelled by a Gaussian  $G(m; m_{B_s}, \sigma_{B_s})$  (Fig. 4.19(a)). Because of the misidentification of the pion,  $m_{B_d}$  will not correspond to the true mass of the  $B_d$  meson, and will be left as a free parameter in the fit, as well as the width of the Gaussian  $\sigma_{B_d}$ .

Assuming that the other sources of background have a linear mass distribution (see Fig. 4.19(b)) they could be modelled by a linear function

$$L(m) = a \cdot m + b, \quad (4.35)$$



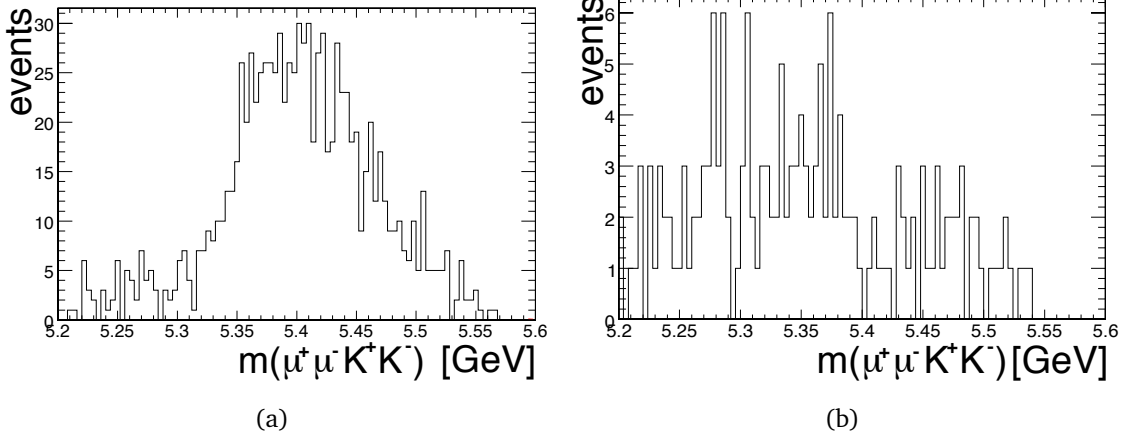


**Figure 4.19:** Four-track invariant mass distribution of the selected misidentified  $B_d \rightarrow J/\psi K^*$  decays (a) and inclusive  $b \rightarrow J/\psi X$  decays (b).

which has to be normalised to one.

The low number of background events which remain after the selection does not allow to draw a definitive conclusion about the shape of their 4-track invariant mass distribution, as mentioned before.

#### 4.4.4 The full probability density function

Taking into account signal and all backgrounds, the total probability density function would be given by

$$\begin{aligned} \mathcal{P} = & \left[ (1 - b_{B_d} - b_s - b_l) \cdot \epsilon(t, \Theta) \cdot f(\Theta, \alpha, t) \cdot G(m; m_{B_s}, \sigma_{B_s}) \right. \\ & + b_{B_d} \cdot f_{B_d}(\Theta) \cdot \epsilon(t) \cdot \frac{1}{\tau_{B_d}} e^{-t/\tau_{B_d}} \cdot G(m; m_{B_d}, \sigma_{B_d}) \\ & \left. + \epsilon(t) \cdot \left( \frac{b_s}{\tau_s} \cdot e^{-t/\tau_{cs}} + \frac{b_l}{\tau_l} \cdot e^{-t/\tau_l} \right) \cdot L(m) \right] \otimes G(t; 0, \sigma_t), \end{aligned} \quad (4.36)$$

where  $b_{B_d}$  is the fraction of misidentified  $B_d$  in the sample. The background fractions  $b_{B_d}$ ,  $b_s$  and  $b_l$  are among the free parameters of the fit.

Due to the lack of simulated background events, it was impossible to fit the full probability density function in Eq. 4.36 (see Section 4.4.3 for details). Thus, we only fitted a probability density function taking into account signal only:

$$\mathcal{P} = [\epsilon(t, \Theta) \cdot f(\Theta, \alpha, t)] \otimes G(t; 0, \sigma_t), \quad (4.37)$$

Since the background is omitted in the probability density function, the mass distributions are no longer needed to estimate the background fractions.

For a maximum likelihood fit, the probability density function has to be normalized to a constant. As a result of the time-dependent efficiency, the integral over the proper decay time of Eq. 4.36 is no longer 1, but depends on the estimated parameters. The fitted probability density function is thus re-normalized for each fit iteration. This is done by calculating numerically the probability density function integral over the proper decay time and the angles. The minimisation is performed using Minuit [58].

#### 4.4.5 Results from full detector simulation

To perform a realistic analysis, the signal and the different backgrounds have to be normalised to the same integrated luminosity. Due to the limited CPU resources only samples of limited size could be generated, which do not permit to have a final dataset with the foreseen number of events. Indeed, the simulated signal corresponds to an integrated luminosity of  $6.8 \text{ fb}^{-1}$ , while the simulated inclusive background  $b \rightarrow J/\psi X$  corresponds to an integrated luminosity of barely  $48 \text{ pb}^{-1}$ . No events from the prompt  $J/\psi$  production were left after the offline selection. The situation is somewhat better for the decay  $B_d \rightarrow J/\psi K^*$  for which the simulated dataset corresponds to an integrated luminosity of  $1.3 \text{ fb}^{-1}$ . The composition of the samples is detailed in Tab. 4.8.

We proceed in two steps. A fit is first performed on the complete set of selected  $B_s$  candidates from simulated signal events with full detector simulation (corresponding to  $6.8 \text{ fb}^{-1}$ ), using the probability density function in Eq. 4.37. The results, given in Tab. 4.15, are comparable to those obtained in the validation tests with the simplified toy Monte Carlo simulation (Section 4.4.1), with a relative width difference  $\Delta\Gamma_s/\bar{\Gamma}_s$  determined with an uncertainty of 0.016. No sensitivity on the weak phase and the strong phases is obtained.

Now, the likelihood fit is performed on a simulated sample containing signal,  $B_d \rightarrow J/\psi K^*$  and combinatorial background events. For this a sample corresponding to an integrated luminosity of  $1.3 \text{ fb}^{-1}$  is used. This allows to use the correct ratio between signal and  $B_d \rightarrow J/\psi K^*$  events. Due to the low number of generated background events passing the reconstruction and selection, it was neither possible to parametrise the angular distributions nor the proper time distributions of any of the backgrounds (see Section 4.4.3). Thus the likelihood fit was applied assuming a signal only probability density function (Eq. 4.37).

A tighter cut on the reconstructed  $B_s$  mass is then applied. Only  $B_s$  candidates with an invariant mass in a window  $\pm 36 \text{ MeV}/c^2$  around the world-average  $B_s$  mass are selected. This reduces the number of background  $B_d$  events by a further 59%, while reducing the number of signal candidates by 2.9%. The results of the likelihood fit on a sample containing signal and  $B_d$  background events corresponding to an integrated luminosity of  $1.3 \text{ fb}^{-1}$  are summarised in Tab. 4.16. The distribution of the proper

Parameter	Input value	Result	Stat.error	Rel.error
$ A_0(0) ^2$	0.57	0.5740	0.0027	0.4%
$ A_{  }(0) ^2$	0.217	0.2181	0.0047	2.1%
$ A_{\perp}(0) ^2$	0.213	0.2079	0.0040	1.9%
$\bar{\Gamma}_s$	0.712 ps <sup>-1</sup>	0.7124 ps <sup>-1</sup>	0.0035 ps <sup>-1</sup>	0.5%
$\Delta\Gamma_s$	0.142 ps <sup>-1</sup>	0.135 ps <sup>-1</sup>	0.011 ps <sup>-1</sup>	8.0%
$\Delta\Gamma_s/\bar{\Gamma}_s$	0.2	0.189	0.016	8.4%
$\delta_1$	$\pi$	2.94	0.63	
$\delta_2$	0	-0.11	0.64	
$\phi_s$	-0.04	-0.030	0.076	

**Table 4.15:** Results of the maximum likelihood fit for an integrated luminosity of 6.8 fb<sup>-1</sup> (signal only).  $|A_{\perp}(0)|^2$  and  $\Delta\Gamma_s/\bar{\Gamma}_s$  are not fitted but calculated from the other fitted parameters.

Parameter	Input value	Result	Stat.error	Rel.error
$ A_0(0) ^2$	0.57	0.5823	0.0061	1.1%
$ A_{  }(0) ^2$	0.217	0.2130	0.0077	3.6%
$ A_{\perp}(0) ^2$	0.213	0.2047	0.0065	3.2%
$\bar{\Gamma}_s$	0.712 ps <sup>-1</sup>	0.7060 ps <sup>-1</sup>	0.0080 ps <sup>-1</sup>	1.1%
$\Delta\Gamma_s$	0.142 ps <sup>-1</sup>	0.144 ps <sup>-1</sup>	0.026 ps <sup>-1</sup>	17.7%
$\Delta\Gamma_s/\bar{\Gamma}_s$	0.2	0.204	0.037	18.4%

**Table 4.16:** Results of the maximum likelihood fit for an integrated luminosity of 1.3 fb<sup>-1</sup> (signal, combinatorial and  $B_d \rightarrow J/\psi K^*$  background).  $|A_{\perp}(0)|^2$  and  $\Delta\Gamma_s/\bar{\Gamma}_s$  are not fitted but calculated from the other fitted parameters.

decay time with the fit is shown in Fig. 4.20. As a comparison, the likelihood fit was performed again on a sample containing only signal events corresponding to the same luminosity of 1.3 fb<sup>-1</sup>. As can be seen, the influence of the background is very small, with only a slight degradation of the width difference for the case that signal and background events were used in the likelihood fit.

#### 4.4.6 Systematics and detector effects

The list of systematic uncertainties which were considered are given below and are summarized in two tables. The first, Tab. 4.18, summarizes the uncertainties which affect the rates at HLT and offline reconstruction and selection. The second, Tab. 4.19, summarizes the uncertainties which affect the measurement of the various parameters.

- Track reconstruction efficiency:

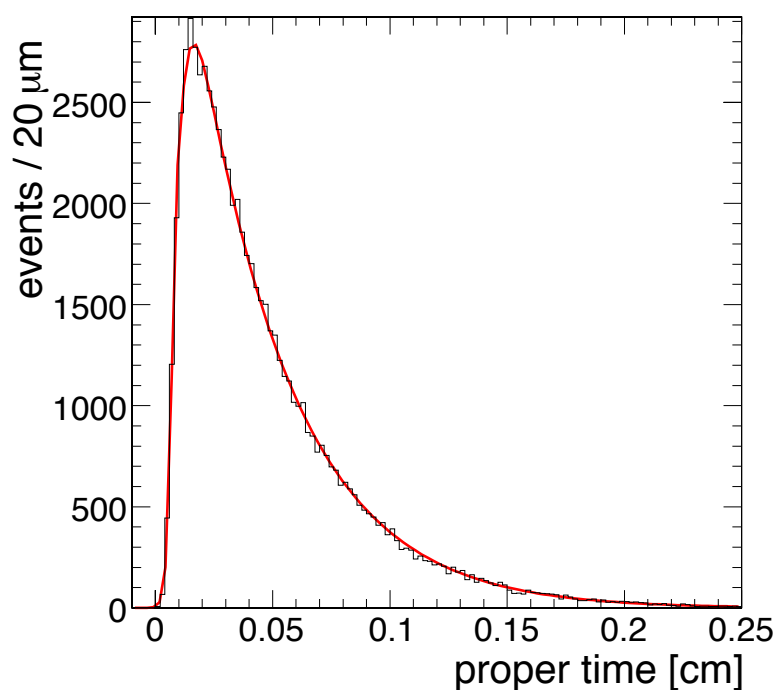


**Figure 4.20:** Distributions of the proper decay length of the selected signal and background events with fit projection.

A 1% uncertainty per track on the track reconstruction efficiency is assumed for all tracks [59].

- Muon reconstruction:

The event selection relies heavily on the correct identification of muons. A 1% uncertainty per track on the combined muon identification procedure is assumed [59].

- Tracker and muon detector misalignment:

The study has been conducted with a perfectly aligned detector. To gauge the

**Table 4.17:** Results of the maximum likelihood fit for an integrated luminosity of  $1.3 \text{ fb}^{-1}$  (signal only).  $|A_{\perp}(0)|^2$  and  $\Delta\Gamma_s/\bar{\Gamma}_s$  are not fitted but calculated from the other fitted parameters.

Parameter	Input value	Result	Stat.error	Rel.error
$ A_0(0) ^2$	0.57	0.5859	0.0062	1.1%
$ A_{\parallel}(0) ^2$	0.217	0.2141	0.0078	3.6%
$ A_{\perp}(0) ^2$	0.213	0.2002	0.0064	3.2%
$\bar{\Gamma}_s$	$0.712 \text{ ps}^{-1}$	$0.7018 \text{ ps}^{-1}$	$0.0081 \text{ ps}^{-1}$	1.2%
$\Delta\Gamma_s$	$0.142 \text{ ps}^{-1}$	$0.147 \text{ ps}^{-1}$	$0.026 \text{ ps}^{-1}$	17.4%
$\Delta\Gamma_s/\bar{\Gamma}_s$	0.2	0.210	0.037	18.1%

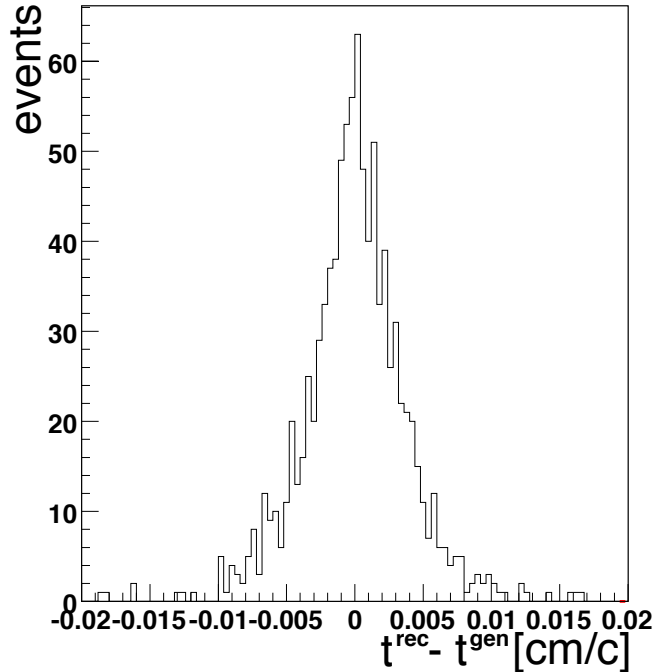


**Figure 4.21:** Distribution of  $t^{\text{rec}} - t^{\text{gen}}$  for  $B_s^0$  proper decay time, estimated from the transverse decay length, for the short-term alignment.

sensitivity of the analysis with respect to the alignment, the analysis has been repeated on a detector with long or short-term alignment scenario. The short-term alignment scenario is expected to be representative of the relative misalignment of the detector components during the initial data taking period, while the long-term alignment scenario is intended to be representative of a mature understanding of the detector, for which optimal alignment corrections have been applied [60]. The pixel detector has the same level of misalignment assumed in both scenarios. In the silicon-strip tracker (SST) the short-term alignment is ten times worse than the long-term alignment. The effects of misalignment of the tracker on various aspects of track and vertex reconstruction have been extensively studied and reported in [61, 62]. The degradation affect both the selection, mostly through the requirement on the significance of the transverse decay length of the  $J/\psi$  in the HLT, and the analysis, through the degradation of the measurement of the proper decay length. The resolution of the latter is degraded from  $\sigma = 24 \mu\text{m}$  for a perfectly aligned detector to  $\sigma = 32 \mu\text{m}$  with the short-term alignment (Fig. 4.21). The HLT efficiency is degraded by some 17% with respect to a perfectly aligned detector.

- Background

To gauge the influence of the background on the fit, the variation observed

source	HLT uncert.	offline uncert.
tracking inefficiency	2 %	2%
muon reconstruction	-	1.4%
misalignment	17%	-

**Table 4.18:** List of systematic uncertainties with effect on the predictions of the rates.

between the fits performed on the reduced  $1.3 \text{ fb}^{-1}$  dataset with and without the background events is added to the systematic uncertainty (Tab. 4.19), as described in Section 4.4.5.

- Signal to background ratio

The largest single source of uncertainty in the estimate of the number of events is obviously the poor knowledge of the  $B_s \rightarrow J/\psi \phi$  branching ratio. This measurement was performed relative to several other fully reconstructed  $B$  decays by CDF [63]. The uncertainty on the relative branching ratio between the decays  $B_s \rightarrow J/\psi \phi$  and  $B_d \rightarrow J/\psi K^*$  is 33%. This uncertainty is slightly more precise than the measurement on the absolute branching ratio since the dominant uncertainties are the low number of  $B_s$  candidates and the fragmentation. Furthermore, in the determination of the absolute branching ratio, two other reference decays are used in addition to the  $B_d \rightarrow J/\psi K^*$  decay. It can be expected that this branching ratio will be measured with a much better accuracy at the Tevatron in the current run, and that it will be measured at the LHC experiments. The various uncertainties are listed in Section 4.1. The errors quoted do not include the uncertainty on the total  $b\bar{b}$  cross section at LHC energies; however, since both the signal and background are proportional to this cross section, the signal-to-background ratio is unaffected by the uncertainty. The signal-to-background ratio has thus a significant uncertainty due to the uncertainties of the branching ratios.

To evaluate the influence of this uncertainty on the likelihood fit, the fit performed on the reduced  $1.3 \text{ fb}^{-1}$  sample was repeated varying the number of  $B_s$  signal events to match the uncertainty in the signal-to-background ratio. For this estimate, we have chosen a smaller uncertainty for the  $B_s$  branching fraction as given in Section 4.1, since we believe that it will be measured again in the current run of the Tevatron and in the very first data taking period of the LHC. Instead we assume an uncertainty of the  $B_s$  branching ratio of 20%. For the other branching ratio uncertainties, we use the numbers listed in Section 4.1. The variation observed on the fit is listed under the heading “S/B ratio” in Tab. 4.19.

- Proper time efficiency

source	$ A_0(0) ^2$	$ A_{  }(0) ^2$	$ A_{\perp}(0) ^2$	$\bar{\Gamma}_s$ [ps <sup>-1</sup> ]	$\Delta\Gamma_s/\bar{\Gamma}_s$
alignment	0.00012	0.00042	0.00055	0.00040	0.0014
background	0.0034	0.0011	0.0045	0.0043	0.0059
$S/B$ ratio	0.0037	0.0001	0.0024	0.0025	0.0055
$\epsilon(t)$	0.0016	0.00073	0.0023	0.022	0.015
$\epsilon(\Theta)$	0.014	0.0061	0.0082	0.00083	0.0010
resolution	-	-	-	0.00060	0.0045
total	0.015	0.0063	0.0099	0.023	0.017

**Table 4.19:** List of systematic uncertainties with effect on the measurements. Since we assumed that the different contributions are independent, the total systematic uncertainty is the square sum of all uncertainties.

Fits were performed where the parameters of the time dependent efficiency function are varied by one standard deviation. The mean variation of the fitted parameters was added to the systematic uncertainty (labelled  $\epsilon(t)$  in Tab. 4.19). As already mentioned, the decay  $B_d \rightarrow J/\psi K^*$  can be used to compare the accuracy of the proper time efficiency comparing the Monte Carlo prediction with the efficiency function observed in the data.

- Angular efficiency

The expansion used to model the distortion of the angular distributions (Eq. 4.19) is limited to  $L, R \leq 8$ . When limiting the expansion to  $L, R \leq 6$  or  $L, R \leq 10$ , the result of the fit shows negligible differences. In addition, to account for the possibility that the efficiencies do not factorize and that the angular efficiency is grossly miscalculated, the fit is also repeated without the angular efficiency, i.e. without correction of the distortion. While this has little influence on the estimated widths, a large variation is found for the amplitudes. This variation is used as systematic uncertainty labelled  $\epsilon(\Theta)$  in Tab. 4.19.

- Resolution on the angles  $\Theta$  and the proper decay time  $t$

To account for the influence of the uncertainties of the angles  $\Theta$  and the proper decay time  $t$ , the variation found when varying the smearing in the toy Monte Carlo (Section 4.4.1.2) is added to the systematic uncertainty.

Tab. 4.19 summarises all systematic uncertainties with effect on the measurement. In Tab. 4.20 the final results including all systematic uncertainties for 1.3 fb<sup>-1</sup> are given.

## 4.5 Conclusions

In this part of the thesis, prospects for an analysis of  $B_s \rightarrow J/\psi (\rightarrow \mu^+ \mu^-) \phi (\rightarrow K^+ K^-)$  events with the CMS detector at LHC were studied. This decay is of particular interest since it allows to study many properties of the  $B_s$  system such as the width difference  $\Delta\Gamma_s$  between the light and heavy mass eigenstates of the  $B_s$  and the CP violating phase  $\phi_s$ .

The selection with a dedicated trigger for this decay is presented. It is based on the identification of  $J/\psi$  and  $B_s$  candidates with a displaced decay vertex. This trigger is characterised by its high background suppression, keeping more than 20% of the signal events. For a lower instantaneous luminosity than assumed in this study, the strong Level-3 constraints (cut on reconstructed  $\phi$  and  $B_s$  masses and transverse momenta) could be dropped, leading to a trigger useful for CMS for a wide range of analyses focused on  $b \rightarrow J/\psi X$  events.

The offline reconstruction is similar to the trigger reconstruction, with the difference that the complete detector information is available. A constrained vertex fit is applied on reconstructed  $B_s$  events to obtain a precise prediction of the proper decay time. The resolution obtained after applying the fit is  $\sigma(t) = 23 \mu\text{m}/c = 7.7 \cdot 10^{-14} \text{ s}$ . In addition, the  $\chi^2$ -probability of the vertex fit is a good parameter to distinguish between signal and backgrounds. An efficiency of 15% for signal events is obtained (including the trigger efficiency) while most of the backgrounds are rejected by another order of magnitude with respect to the trigger rejection. The background to signal ratio is now 20%.

The differential decay rate of  $B_s \rightarrow J/\psi (\rightarrow \mu^+ \mu^-) \phi (\rightarrow K^+ K^-)$  events can be written as

$$\frac{d^4\Gamma(B_s(t))}{d\Theta dt} = f(\Theta, \alpha, t), \quad (4.38)$$

where  $t$  is the proper decay time and  $\Theta$  is a set of three angles defined by the decay kinematics. The set of physical parameters such as the average decay time  $\bar{\Gamma}_s$ , the de-

**Table 4.20:** Results of the maximum likelihood fit for an integrated luminosity of  $1.3 \text{ fb}^{-1}$  (signal and background).  $|A_{\perp}(0)|^2$  and  $\Delta\Gamma_s/\bar{\Gamma}_s$  are not fitted but calculated from the other fitted parameters.

Parameter	Input value	Result	Stat. error	Sys. error	Total error	Rel. error
$ A_0(0) ^2$	0.57	0.582	0.006	0.015	0.016	2.8%
$ A_{\parallel}(0) ^2$	0.217	0.213	0.008	0.006	0.010	4.6%
$ A_{\perp}(0) ^2$	0.213	0.205	0.007	0.010	0.012	5.8%
$\bar{\Gamma}_s$	$0.712 \text{ ps}^{-1}$	$0.7060 \text{ ps}^{-1}$	$0.0080 \text{ ps}^{-1}$	$0.0227 \text{ ps}^{-1}$	$0.0240 \text{ ps}^{-1}$	3.4%
$\Delta\Gamma_s$	$0.142 \text{ ps}^{-1}$	$0.144 \text{ ps}^{-1}$	$0.026 \text{ ps}^{-1}$	$0.011 \text{ ps}^{-1}$	$0.028 \text{ ps}^{-1}$	19%
$\Delta\Gamma_s/\bar{\Gamma}_s$	0.2	0.204	0.037	0.017	0.041	20%



cay time difference  $\Delta\Gamma_s$  and the weak phase  $\phi_s$  is represented by  $\alpha$ . A time-dependent angular fit on this differential decay rate was developed to extract several parameters of the  $B_s$  system simultaneously. First, the fit was widely tested on a simplified event generation developed for this purpose (toy Monte Carlo simulation).

Then the angular analysis was performed using a full detector simulation. In this case, the likelihood fit needs to take into account the distortion of the angular and proper decay time distributions due to the finite resolutions and the event selection criteria. A measurement with an integrated luminosity of  $1.3 \text{ fb}^{-1}$  of data could already yield a measurement of  $\Delta\Gamma_s/\bar{\Gamma}_s$  with an absolute error of  $\sigma = 0.04$  (Tab. 4.20) including the systematic error. This error corresponds to a relative uncertainty of 20% assuming  $\Delta\Gamma_s/\bar{\Gamma}_s = 0.2$ .

The analysis could be further improved by using larger samples of generated background events, which were not available at the time of this study. In that case, the background distributions could be modelled in the fit, resulting in a better precision. In case of real collision data the decay  $B_d \rightarrow J/\psi(\rightarrow \mu^+\mu^-)K^*(\rightarrow K^+\pi^-)$  could be used to test the fit method since the parameters in the  $B_d$  system have been measured with high precision in other experiments.



# Bibliography

- [1] **CDF Collaboration**, “An Updated Measurement of the  $CP$  Violating Phase  $\beta_s^{J/\psi\phi}$ ,” *CDF Note* **08-07-24** (2008).
- [2] **D0 Collaboration**, V. M. Abazov et al., “Measurement of the angular and lifetime parameters of the decays  $B_d^0 \rightarrow J/\psi K^{*0}$  and  $B_s^0 \rightarrow J/\psi\phi$ ,” *Phys. Rev. Lett.* **102** (2009) 032001, [arXiv:0810.0037](https://arxiv.org/abs/0810.0037).  
[doi:10.1103/PhysRevLett.102.032001](https://doi.org/10.1103/PhysRevLett.102.032001).
- [3] **Particle Data Group Collaboration**, C. Amsler et al., “Review of Particle Physics,” *Phys. Lett.* **B667** (2008) 1.  
[doi:10.1016/j.physletb.2008.07.018](https://doi.org/10.1016/j.physletb.2008.07.018).
- [4] J. Charles et al., “CP violation and the CKM matrix: Assessing the impact of the asymmetric  $B$  factories,” *Eur. Phys. J.* **C41** (2005) 1–131,  
[arXiv:hep-ph/0406184](https://arxiv.org/abs/hep-ph/0406184). updates at <http://ckmfitter.in2p3.fr/>.  
[doi:10.1140/epjc/s2005-02169-1](https://doi.org/10.1140/epjc/s2005-02169-1).
- [5] **UTfit Collaboration**, M. Bona et al., “The 2004 UTfit Collaboration report on the status of the unitarity triangle in the standard model,” *J. of High Energy Phys.* **07** (2005) 028, [arXiv:hep-ph/0501199](https://arxiv.org/abs/hep-ph/0501199). updates at <http://www.utfit.org>.
- [6] I. Dunietz, R. Fleischer, and U. Nierste, “In pursuit of new physics with  $B_s$  decays,” *Phys. Rev.* **D63** (2001) 114015.  
[doi:10.1103/PhysRevD.63.114015](https://doi.org/10.1103/PhysRevD.63.114015).
- [7] A. S. Dighe, I. Dunietz, and R. Fleischer, “Extracting CKM phases and  $B_s - \bar{B}_s$  mixing parameters from angular distributions of non-leptonic  $B$  decays,” *Eur. Phys. J.* **C6** (1999) 647–662. [doi:10.1007/s100529800954](https://doi.org/10.1007/s100529800954).
- [8] A. S. Dighe, I. Dunietz, H. J. Lipkin, and J. L. Rosner, “Angular distributions and lifetime differences in  $B_s \rightarrow J/\psi\phi$  decays,” *Phys. Lett.* **B369** (1996) 144–150.  
[doi:10.1016/0370-2693\(95\)01523-X](https://doi.org/10.1016/0370-2693(95)01523-X).

- [9] **Heavy Flavor Averaging Group (HFAG)** Collaboration, K. Anikeev et al., “Averages of  $b$ -hadron properties as of winter 2005,” [arXiv:hep-ex/0505100](#).
- [10] A. J. Lenz, “Mixing and lifetimes of  $b$ -hadrons,” *AIP Conf. Proc.* **1026** (2008) 36–47, [arXiv:0802.0977](#). [doi:10.1063/1.2965074](#).
- [11] E. Norrbin and T. Sjostrand, “Production and hadronization of heavy quarks,” *Eur. Phys. J.* **C17** (2000) 137–161, [arXiv:hep-ph/0005110](#). [doi:10.1007/s100520000460](#).
- [12] **Particle Data Group** Collaboration, S. Eidelman et al., “Review of Particle Physics,” *Phys. Lett.* **B592** (2004) 1. [doi:10.1016/j.physletb.2004.06.001](#).
- [13] **CDF** Collaboration, A. Abulencia et al., “Observation of  $B/s_0$  anti- $B/s_0$  oscillations,” *Phys. Rev. Lett.* **97** (2006) 242003, [arXiv:hep-ex/0609040](#). [doi:10.1103/PhysRevLett.97.242003](#).
- [14] H. G. Moser and A. Roussarie, “Mathematical methods for  $B_0$  anti- $B_0$  oscillation analyses,” *Nucl. Instrum. Meth. in Phys. Research* **A384** (1997) 491–505. [doi:10.1016/S0168-9002\(96\)00887-X](#).
- [15] **D0** Collaboration, “ $B_s^0$  Oscillation Combination for Summer 2007,” *DO Note* **5618-CONF** (2007).
- [16] **D0** Collaboration, “D0 results on  $\Delta\Gamma_s$  versus  $CP$ -Violating Phase  $\phi_s^{J/\psi\phi}$ ,” *DO Note* **5933-CONF** (2009).
- [17] O. Bruning et al., “LHC Design Report. Vol. I: The LHC Main Ring,” CERN-2004-003-V-1.
- [18] O. Buning et al., “LHC Design Report. 2. The LHC Infrastructure and General Services,” CERN-2004-003-V-2.
- [19] M. Benedikt, P. Collier, V. Mertens, J. Poole, and K. Schindl, “LHC Design Report. 3. The LHC injector chain,” CERN-2004-003-V-3.
- [20] **CMS** Collaboration, R. Adolphi et al., “The CMS experiment at the CERN LHC,” *J. of Instrumentation* **3** (2008) S08004. [doi:10.1088/1748-0221/3/08/S08004](#).
- [21] **ATLAS** Collaboration, G. Aad et al., “The ATLAS Experiment at the CERN Large Hadron Collider,” *J. of Instrumentation* **3** (2008) S08003. [doi:10.1088/1748-0221/3/08/S08003](#).
- [22] **CMS** Collaboration, “The CMS Magnet Project: Technical Design Report”. Technical Design Report CMS. CERN, Geneva, 1997.

- 
- [23] CMS Collaboration, , “The CMS Physics Technical Design Report, Volume 1,” *CERN/LHCC 2006-001* (2006). CMS TDR 8.1.
- [24] C. Amsler et al., “Mechanical Design and Material Budget of the CMS Barrel Pixel Detector,” *J. of Instrumentation* **4** (2009) P05003.  
[doi:10.1088/1748-0221/4/05/P05003](https://doi.org/10.1088/1748-0221/4/05/P05003).
- [25] I. Bird et al., “LHC Computing Grid. Technical Design report,”  
CERN-LHCC-2005-024.
- [26] CMS Collaboration, “CMS: The Computing Project. Technical Design Report,”  
CERN-LHCC-2005-023.
- [27] Y. Allkofer et al., “Design and performance of the silicon sensors for the CMS barrel pixel detector,” *Nucl. Instrum. Meth. in Phys. Research* **A584** (2008) 25–41, [arXiv:physics/0702092](https://arxiv.org/abs/physics/0702092).
- [28] E. Alagöz, “Simulation and beam test measurements of the CMS pixel detector”. PhD thesis, Universität Zürich, 2009.
- [29] A. Dorokhov et al., “Tests of silicon sensors for the CMS pixel detector,” *Nucl. Instrum. Meth. in Phys. Research* **A530** (2004) 71–76,  
[arXiv:physics/0311050](https://arxiv.org/abs/physics/0311050).
- [30] A. Dorokhov et al., “Electric field measurement in heavily irradiated pixel sensors,” *Nucl. Instrum. Meth. in Phys. Research* **A560** (2006) 112–117,  
[arXiv:physics/0412036](https://arxiv.org/abs/physics/0412036).
- [31] A. Castoldi, E. Gatti, V. Manzari, and P. Rehak, “Performance of silicon drift detectors in a magnetic field,” *Nucl. Instrum. Meth. in Phys. Research* **A399** (1997), no. 2-3, 227 – 243. [doi:DOI: 10.1016/S0168-9002\(97\)00909-1](https://doi.org/10.1016/S0168-9002(97)00909-1).
- [32] R. Kaufmann, “Development of Radiation Hard Pixel Sensors for the CMS Experiment”. PhD thesis, Universität Zürich, 2001.
- [33] CMS Collaboration, “L1 Trigger Performance,” *to be published in J. of Instrumentation* (2009).
- [34] CMS Collaboration, “The CMS Silicon Strip Tracker Operation and Performance With Cosmic Rays in 3.8 T Magnetic Field,” *to be published in J. of Instrumentation* (2009).
- [35] CMS Collaboration, “Alignment of the CMS Silicon Tracker During Commissioning with Cosmic Ray Particles,” *to be published in J. of Instrumentation* (2009).
- [36] CMS Collaboration, “Performance of the CMS pixel detector with cosmic ray data,” *to be published in J. of Instrumentation* (2009).
-

- [37] V. Chiochia et al., “Simulation of heavily irradiated silicon pixel sensors and comparison with test beam measurements,” *IEEE Trans. Nucl. Sci.* **52** (2005) 1067–1075, [arXiv:physics/0411143](#). [doi:10.1109/TNS.2005.852748](#).
- [38] M. Swartz et al., “Observation, modeling, and temperature dependence of doubly peaked electric fields in irradiated silicon pixel sensors,” *Nucl. Instrum. Meth. in Phys. Research A* **565** (2006) 212–220, [arXiv:physics/0510040](#). [doi:10.1016/j.nima.2006.05.002](#).
- [39] E. James, Y. Maravin, M. Mulders, and N. Neumeister, “Muon identification in CMS,” *CMS Note* **2006/010** (2006).
- [40] V. Ciulli, N. Magini, L. Wilke, T. Speer, K. Prokofiev, S. Shulga, and T. Ilicheva, “Study of the decay  $B_s \rightarrow J/\psi \phi \rightarrow \mu^+ \mu^- K^+ K^-$ ,” *CMS Note* **2006/121** (2006).
- [41] **CMS** Collaboration, G. L. Bayatian et al., “CMS Technical Design Report, Volume II: Physics performance,” *J. Phys.* **G34** (2007) 995–1579. [doi:10.1088/0954-3899/34/6/S01](#).
- [42] T. Sjostrand, L. Lonnblad, and S. Mrenna, “PYTHIA 6.2: Physics and manual,” [arXiv:hep-ph/0108264](#).
- [43] A. Belkov and S. Shulga, “Studies of angular correlations in the decays  $B_s \rightarrow J/\psi \phi$  by using the SIMUB generator,” *Comput. Phys. Commun.* **156** (2004) 221–240, [arXiv:hep-ph/0310096](#). [doi:10.1016/S0010-4655\(03\)00465-X](#).
- [44] **GEANT4** Collaboration, S. Agostinelli et al., “GEANT4: A simulation toolkit,” *Nucl. Instrum. Meth. in Phys. Research A* **506** (2003) 250–303.
- [45] P. Nason et al., “Bottom production, in Proceedings of the workshop on Standard Model physics (and more) at the LHC”. CERN, 2000.
- [46] J. M. Campbell, J. W. Huston, and W. J. Stirling, “Hard Interactions of Quarks and Gluons: A Primer for LHC Physics,” *Rept. Prog. Phys.* **70** (2007) 89, [arXiv:hep-ph/0611148](#). [doi:10.1088/0034-4885/70/1/R02](#).
- [47] J. Baines et al., “Heavy Quarks (Working Group 3): Summary Report for the HERA-LHC Workshop Proceedings,” [arXiv:hep-ph/0601164](#).
- [48] **CDF** Collaboration, F. Abe et al., “Production of  $J/\psi$  mesons from  $\chi_c$  meson decays in  $p\bar{p}$  collisions at  $\sqrt{s} = 1.8$  TeV,” *Phys. Rev. Lett.* **79** (1997) 578–583. [doi:10.1103/PhysRevLett.79.578](#).
- [49] B. Cano-Coloma and M. A. Sanchis-Lozano, “Charmonia production in hadron colliders and the extraction of colour-octet matrix elements,” *Nucl. Phys.* **B508** (1997) 753–767, [arXiv:hep-ph/9706270](#). [doi:10.1016/S0550-3213\(97\)00660-3](#).

- 
- [50] **CMS** Collaboration, , “The TriDAS Project Technical Design Report, Volume 2: Data Acquisition and High-Level Trigger,” *CERN/LHCC 2002-26* (2002). CMS TDR 6.2.
- [51] **CMS** Collaboration, , “The TriDAS Project Technical Design Report, Volume 1: The Level-1 Trigger,” *CERN/LHCC 2000-38* (2000). CMS TDR 6.1.
- [52] S. Cucciarelli, M. Konecki, D. Kotlinski, and T. Todorov, “Track reconstruction, primary vertex finding and seed generation with the Pixel Detector,” *CMS Note 2006/026* (2006).
- [53] K. Prokofiev, “Study of the  $B_s^0 \rightarrow (J/\psi)\phi \rightarrow \mu^+\mu^-K^+K^-$  Decay with the CMS Detector at LHC”. PhD thesis, Universität Zürich, 2005.
- [54] R. Frühwirth, P. Kubinec, W. Mitaroff, and M. Regler, “Vertex reconstruction and track bundling at the LEP collider using robust algorithms,” *Comput. Phys. Commun.* **96** (1996) 189–208. doi:10.1016/0010-4655(96)00040-9.
- [55] K. Prokofiev and T. Speer, “A kinematic fit and a decay chain reconstruction library,” *CERN 2005-002* (2005). Proc. of the 2004 Conference for Computing in High-Energy and Nuclear Physics (CHEP 04), Interlaken, Switzerland, 2004.
- [56] **BABAR** Collaboration, B. Aubert et al., “Ambiguity-free measurement of  $\cos(2\beta)$ : Time-integrated and time-dependent angular analyses of  $B \rightarrow J/\psi K\pi$ ,” *Phys. Rev.* **D71** (2005) 032005, arXiv:hep-ex/0411016.
- [57] I. Dunietz, H. Quinn, A. Snyder, W. Toki, and H. J. Lipkin, “How to extract CP-violating asymmetries from angular correlations,” *Phys. Rev.* **D43** (1991) 2193–2208.
- [58] F. James and M. Roos, “MINUIT: A System for Function Minimization and Analysis of the Parameter Errors and Correlations,” *Comput. Phys. Commun.* **10** (1975) 343–367. doi:10.1016/0010-4655(75)90039-9.
- [59] **CMS** Collaboration, , “The CMS Technical Design Report, Vol. 1: Detector Performance and Software ,”. CERN/LHCC 2006-001.
- [60] I. Belotelov et al., “Simulation of Misalignment Scenarios for CMS Tracking Devices,” *CMS Note* (2006).
- [61] P. Vanlaer et al., “Impact of CMS Silicon Tracker Misalignment on Track and Vertex Reconstruction,” *CMS Note* (2006).
- [62] T. Speer et al., “Vertex Fitting in the CMS Tracker,” *CMS Note* (2006).
- [63] **CDF** Collaboration, F. Abe et al., “Ratios of bottom meson branching fractions involving  $J/\psi$  mesons and determination of  $b$  quark fragmentation fractions,” *Phys. Rev.* **D54** (1996) 6596–6609. doi:10.1103/PhysRevD.54.6596.
-





## Acknowledgements

First of all I would like to express my gratitude to Claude Amsler for giving me the opportunity to do this PhD study and for sharing his great knowledge in particle physics. I am much obliged to Alexander Schmidt who supported me while writing this thesis and gave valuable suggestions for improvements on the text as well as on the analysis parts. Great thanks go to Thomas Speer who eased the start of my PhD a lot and with whom it was always a great pleasure to discuss. Vincenzo Chiochia helped me to understand the way the pixel detector works, answering all questions I came up with. It was a great pleasure to cooperate on the  $B_s$  analysis with Thomas Speer and Nicolo Magini. Their long-time experience with CMS made working much easier. Thanks also to Kirill Prokofiev, on whose work I could base my studies. Many thanks go to Morris Swartz, with whom I had many fruitful discussions concerning the Lorentz angle in the pixel detector, and to Urs Langenegger who helped me on various  $b$ -physics issues.

I wish to thank the whole Uni Zürich CERN group for a lot of instructive discussion and the friendly atmosphere, which made it a pleasure to work here.

I would also like to thank the Paul Scherrer Institut for financial support without which this thesis would not have been possible.

Finally I thank my friends and family for their love and encouragement as always. Special thanks go to Bernd. Without his valuable support, especially in the last month of my PhD, this work would never have been finished.



# Curriculum Vitae

---

## Personal Details

---

**Name:** Lotte WILKE  
**Date of Birth:** 03.01.1979  
**Place of Birth:** Wuppertal (Germany)

---

## Education

---

**since 09/2005** Graduate education in experimental high energy physics  
Universität Zürich  
Thesis Title: *Study of the  $B_s$ -Meson with the First LHC Data*

**10/1998 - 01/2005** Diploma in Physik, RWTH Aachen  
Final grade *sehr gut*  
Diploma Thesis: *Measurement of Jet Production in Proton Antiproton Collisions with the DO Detector*

**08/1989 - 06/1998** Abitur, Couven-Gymnasium Aachen  
Final grade *1.7*  
Leistungsfächer *Mathematik und Physik*

---

## Publications (only excerpt)

---

**CMS** Collaboration, “Performance of the CMS pixel detector with cosmic ray data” ,  
*submitted to J. of Instrumentation.*

L. Wilke, “Heavy Flavour Physics at CMS and ATLAS”, Proceedings of the 44th rencontre de Moriond on QCD and High Energy Interactions (2009).

V. Chiochia, T. Speer, L. Wilke, “Lorentz angle calibration for the barrel pixel detector”,  
*CMS Note 2008/012* (2006).

**CMS** Collaboration, “CMS technical design report, volume II: Physics performance” ,  
*J. Phys. G34* (2007) 995-1579.

V. Ciulli, T. Ilicheva, N. Magini, K. Prokofiev, S. Shulga, T. Speer, L. Wilke, “Study of the decay  $B_s \rightarrow J/\psi \phi \rightarrow \mu^+ \mu^- K^+ K^-$ ”, *CMS Note 2006/121* (2006).

---

